KUOPION YLIOPISTON JULKAISUJA C. LUONNONTIETEET JA YMPÄRISTÖTIETEET 166
KUOPIO UNIVERSITY PUBLICATIONS C. NATURAL AND ENVIRONMENTAL SCIENCES 166

PÄIVI J. VAUHKONEN

Image Reconstruction in Three-Dimensional Electrical Impedance Tomography

Doctoral dissertation

To be presented by permission of the Faculty of Natural and Environmental Sciences of the University of Kuopio for public examination in Auditorium L23, Snellmania building, University of Kuopio, on Saturday 3rd January 2004, at 12 noon

Department of Applied Physics
University of Kuopio

KUOPION YLIOPISTO
KUOPIO 2004

Distributor:
Kuopio University Library
P.O. Box 1627
FIN-70211 KUOPIO
FINLAND
Tel. +358 17 163430
Fax +358 17 163410
http://www.uku.fi/kirjasto/julkaisutoiminta/julkmyyn.html

Series Editor:
Professor Lauri Kärenlampi Ph.D.
Department of Ecology and Environmental Science
University of Kuopio

Professor Jari Kaipio, Ph.D.
Department of Applied Physics
University of Kuopio

Author's address:
Department of Applied Physics
University of Kuopio
P.O. Box 1627
FIN-70211 KUOPIO
FINLAND
Tel. +358 17 162 210
Fax +358 17 162 585
E-mail: Paivi.Vauhkonen@uku.fi

Supervisors:
Docent Marko Vauhkonen, Ph.D.
Department of Applied Physics
University of Kuopio

Professor Jari Kaipio, Ph.D.
Department of Applied Physics
University of Kuopio

Professor Erkki Somersalo, Ph.D.
Department of Mathematics
Helsinki University of Technology
Finland

Reviewers:
Assistant Professor Jennifer Mueller, Ph.D.
Department of Mathematics
Colorado State University
Fort Collins, CO, USA

Professor Simon Arridge, Ph.D.
Department of Computer Science
University College London, UK

Opponent:
Docent Samuli Siltanen, Ph.D.
Department of Mathematics
Gunma University
Kiryu, Japan

ISBN 951-781-304-X
ISSN 1235-0486

Kopijyvä
Kuopio 2004
Finland

Vauhkonen, Päivi J. Image Reconstruction in Three-Dimensional Electrical Impedance Tomography. Kuopio University Publications C. Natural and Environmental Sciences 166. 2004. 121 p.
ISBN 951-781-304-X
ISSN 1235-0486

ABSTRACT

In electrical impedance tomography (EIT), weak alternating currents are injected into the object through the electrodes which are attached on the boundary of the object. The resulting voltages can be measured with the same electrodes. An estimate for the internal resistivity distribution of the object is based on known currents and measured voltages. The estimation of static three-dimensional resistivity distributions is a nonlinear and ill-posed inverse problem.

In EIT the injected currents spread out in three dimensions and if this is not considered in the reconstruction, off-plane structures may cause many errors, especially in static EIT. Therefore the three-dimensional (3D) reconstruction is needed, which means that in the realistic EIT problems, for example head imaging, thousands of unknown resistivity parameters have to be determined. These computations take a lot of computer time and storage and therefore the solution method plays a significant role. Because of the nonlinearity and ill-posedness of EIT standard optimization approaches can not be utilized.

In this thesis a finite element-based method for the reconstruction of 3D resistivity distributions is used. The proposed method is based on the so-called complete electrode model that takes into account the presence of the electrodes and the contact impedances. In this thesis different types of iterative optimization methods for the solution of the inverse problem have been studied. Methods in which the expence of inverting large dimensional matrices can be avoided are presented. The proposed approaches are tested with computer simulations.

In some cases, EIT may involve an unbounded domain. In these cases, it is not reasonable to model the whole domain but the model is truncated somewhere. The truncation may cause problems and errors in the image reconstruction. In this thesis the model truncation problem is solved by using infnite element method, which involves the choosing of the shape functions so that they extend to infinity. The approach is compared with method of choosing long elements on the truncation surface.

Universal Decimal Classification: 537.311.6
National Library of Medicine Classification: QT 36, WN 206
INSPEC Thesaurus: electric impedance imaging; image reconstruction; finite element analysis; electrical resistivity; optimization; conjugate gradient methods; inverse problems

Acknowledgements

This study was carried out in the Department of Applied Physics at the University of Kuopio during 1999-2003. The study was supported by Graduate School in Functional Research in Medicine.

I wish to express my greatest gratitude to my main supervisor Docent Marko Vauhkonen, Ph.D. Without his support this thesis would have never been completed. I thank my second supervisor Professor Jari P. Kaipio, Ph.D. for his encouragement and for the opportunity to work in the Department of Applied Physics. I also thank my third supervisor Professor Erkki Somersalo, Ph.D.

I wish to thank the official reviewers Assistant Professor Jennifer Mueller, Ph.D., and Professor Simon Arridge, Ph.D. for their suggestions for this thesis.

I want to thank the staff in the Department of Applied Physics at the University of Kuopio for their support. Especially I thank the members of the Inverse problems research group. Many thanks to Ville Kolehmainen, Ph.D. for fruitful collaboration during several years. Thanks to my former roommate Tanja Tarvainen, M.Sc. for many scientific and non-scientific discussions. I thank Tuomo Savolainen, M.Sc. and Lasse Heikkinen, M.Sc. for their guidance in experimental field in EIT, and Jorma Ollikainen, Ph.D. for collaboration in head imaging. Special thank goes to Aku Seppänen, M.Sc. for his friendship, encouragement and for many valuable suggestions and help with this thesis.

I express my gratitude to all my teachers, especially Docent Jouko Tervo, Ph.D, and Docent Pasi Karjalainen, Ph.D. I also want to thank my students from whom I have learnt at least as much as they have learnt from me.

I thank my friends and associates in Judo club Sakura. Thank you Kari, Tita, Timo, Ritva, Tarja, Pekka A., Pekka K., Seppo, Rami, Pera, Antti, Juha, Petri, Aino, Jukka and Sensei Timo Harju. For me judo acts as an excellent counterbalance to work. I have learnt so much about life (and physics) through judo. Especially my Special needs judo group has taught me a lot. I warmly thank my friend Marita Kokkonen for many common experiences in Special needs judo.

My thanks and appreciation go to my parents Elvi and Jouko Ronkanen, my grandfather Reino Ronkanen, my brothers Hannu and Antti, and my godparents Riitta, Anneli and Veikko. I also thank Tuula, Noora, Henri and Essi for their friendship. I thank my precious friends Saara and Jouko for their support and for reminding me of the life outside the university and dojo.

Finally I want to express my special thanks to my loyal friend Vilma.

Kuopio, 23 December 2003

Päivi Johanna Vauhkonen

1 Introduction **9**

2 On the theory of optimization methods **15**
2.1 Line search methods 16
2.1.1 Inexact line search 16
2.1.2 Steepest descent method 18
2.1.3 Newton's method 19
2.1.4 Newton-Raphson method 21
2.2 Linear and nonlinear least squares problems 23
2.2.1 Gauss-Newton method 24
2.3 Methods for ill-posed least squares problems 25
2.3.1 The singular value decomposition 28
2.3.2 Levenberg-Marquardt method 30
2.3.3 Tikhonov regularization 33
2.3.4 Generalized Tikhonov regularization 35
2.4 Conjugate-gradient methods 39
2.4.1 Conjugate direction method 39
2.4.2 Conjugate gradient method 41
2.4.3 Nonlinear conjugate gradient method 44

3 Forward problem in EIT **48**
3.1 The complete electrode model 48
3.1.1 Boundary conditions 49
3.2 Finite element method in EIT 52
3.2.1 Variational form for the complete electrode model 53
3.2.2 FEM approximation of the complete electrode model 55
3.2.3 Integration with linear basis functions 58
3.2.4 Integration with second order basis functions 62
3.3 Infinite elements 63
3.3.1 Infinite elements based on choosing of the basis functions . 63
3.3.2 Mapped infinite elements 64
3.3.3 Positioning of poles (t_0) 66
3.3.4 Infinite element methods in EIT 67

4 Inverse problem in EIT **74**
4.1 The Jacobian matrix in EIT 74
4.2 The Hessian in EIT 77
4.3 Block form for computing ∇F 78
4.4 Alternative formulation for the Levenberg-Marquardt method . . . 79
4.5 Kaczmarz -method 80
4.6 Extended Kalman filter 81
4.7 Regularization matrix 82
4.8 Difference imaging 82
4.9 Starting point for iteration 83

5 Numerical studies **84**
5.1 Comparison of iterative reconstruction methods 84
5.1.1 Simulated measurements 84
5.1.2 Iterative reconstructions 86
5.1.3 Discussion of the results 90
5.2 Infinite elements 93
5.2.1 Effect of the model truncation 93
5.2.2 Errors in the reconstructions 101

6 Conclusions **110**

References **112**

A Basis functions for 3D wedge element **119**

CHAPTER I

Introduction

ELECTRICAL IMPEDANCE TOMOGRAPHY

Electrical impedance tomography, EIT, is an imaging modality that can be used in cases of conductive targets. In EIT the internal resistivity distribution is reconstructed based on electrical measurements from the boundary of the target. In many cases the resistivity distribution carries valuable information on the structural, and especially, functional properties of the target. For example, in medical applications, different organs of human body posses contrast in resistivities . Further, physiological changes, such as increased blood circulation, cause changes in electrical resistivities of individual organs.

In EIT the electrodes are placed on the surface of an object and current is injected into the object through these electrodes. Current is weak alternating current whose amplitude is usually between 1-5 mA and frequency between 1-100 kHz. The resulting voltages on the surface of the object are measured using the same or additional voltage measurement electrodes. The internal resistivity distribution is computed based on this boundary data. This reconstruction problem is an ill-posed *inverse problem* in the sense of Hadamard [28], and special methods are required for the solution. In the sequel reconstruction of conductivity distribution, instead of resistivity distribution, is also discussed. These reconstruction problems, however, are equivivalent; the conductivity is the inverse of resistivity.

Many applications of EIT have been developed e.g. for medical purposes [112]. A traditional medical application is the imaging of thorax but many promising results have also been obtained from head imaging, for example, locating and monitoring of cerebral haemorrhage [86, 71, 13, 62]. Also realistic head models for numerical computations and validation of three-dimensional algorithms for EIT of human brain function have been used [5, 98]. The resistivity information obtained from EIT could also be used together with EEG (ElectroEnchephaloGraphy), when the internal current sources are estimated [77, 76]. EIT has also been widely used in geophysical [113] and industrial applications [20, 115].

The spatial resolution in EIT is relatively poor in comparison to other modal-

ities, such as, magnetic resonance imaging and X-ray tomography. However, for example in industrial process tomography, where the targets often change very rapidly, EIT is a workable modality due to its good temporal resolution. The fastest EIT system can provide as many as 1000 images per second [115].

The mathematical development in EIT was started in 1980 [14] when the uniqueness of the EIT inverse problem was first addressed. After this paper there have been many studies on the uniqueness of the recovery of the conductivity inside an object based on the measurements made on the boundary. The proofs of the uniqueness in isotropic case in two and three dimensions with different kinds of assumptions can be found in [96, 84, 55, 54, 95, 23, 53, 41, 18, 93, 72]. If the conductivity is anisotropic the recovery is non-unique [94].

The EIT reconstruction methods can be divided in two categories, *stationary* and *non-stationary imaging*. Stationary imaging can further be divided in two categories, *difference imaging* and *static imaging*. In difference imaging two data sets are measured corresponding to two different target conductivity distributions. Based on the difference between these measurements the difference of the conductivity distributions can be estimated. In static imaging the reconstruction is based on a single data set of voltage measurements only, and the aim is to reconstruct the absolute conductivity distribution. This involves very accurate computation of simulated voltages in an arbitrary (simulated reference) conductivity distribution. The computation of the voltage measurements when the currents and the conductivity distribution are known, is called *the forward problem*. In this thesis, reconstruction methods for stationary cases are considered. In non-stationary or *dynamic imaging*, the time-dependence of the resistivity distribution is taken into account, and a reconstruction is obtained after each current injection.

Methods for reconstruction of impedance images are based on mathematical models that connect the internal resistivity distribution to the measurements made on the surface of the object. In [17, 91] various models were studied. In connection with EIT problem these models are referred to as electrode models. It was found that the most coarse model, the so-called continuum model, highly overestimates resistivities and also the more accurate models, the gap and the shunt models, were found respectively, to overestimate and underestimate resistivities [91]. The most accurate model that has been proposed is the so-called *complete electrode model*. This model can take into account the shunting effect of the electrodes and also the contact impedances between the electrodes and the object. The contact impedance is due to the electrochemical reaction in which the electron flow is converted to the ion flow in the object. The contact impedance is especially important when the voltages on the current carrying electrodes (*two electrode method*) are measured. However, the effect of the contact impedance can be minimized by using the separate electrodes for the measurements (*four electrode method*). The complete electrode model has also been used in this study.

In this thesis, the forward problem has been solved by using the finite element method (FEM). FEM is a feasible method for solving partial differential equations with complex geometries and non-trivial boundary conditions [35, 66, 44, 12]. In EIT the finite element method has been used at least since 1985 [70]. For two-

dimensional cases, see [99, 43, 117, 37, 79, 38, 116] and for three-dimensional cases with complete electrode model [85, 109, 108, 103, 81, 80]. For three-dimensional FEM calculations to solve the forward problem of EIT with simplified electrode models see e.g. [58, 116, 88, 87, 59, 63, 97].

In two-dimensional (2D) EIT, an array of electrodes is attached around an object and the images are reconstructed based on the assumption that the injected currents are confined to the two-dimensional electrode plane. However, when electric current passes through the object the current spreads out in three dimensions. If this fact is not considered in the image reconstruction, many errors, especially in static electrical impedance tomography, are produced. For this reason the three-dimensional (3D) approach is justified.

In the early stages of EIT at the beginning of 1980's, only cross-sectional 2D images were considered. Fully three-dimensional (3D) EIT has been discussed later e.g. in [113, 27, 63, 67, 64, 65]. All these proposed approaches have been based on difference imaging and some of them on *ad hoc* approaches to reconstruct 3D images. Also many simplifications have been done in the electrode modeling, which may have produced difficulties of obtaining static reconstructions. In the following, a short summary of the earlier work considering 3D EIT is given.

In [113, 114], an algorithm for electrical impedance tomography was described that makes no prior assumptions about current flow paths. It involves the solution of the associated Poisson equation for inhomogeneous media with an explicit conductivity-updating scheme that is not subject to matrix ill-conditioning problems. A finite element method with a simple physical model (continuum model) was used in the computations. The algorithm uses the measured voltages to cause a change to the conductivity distribution to tend toward minimization of the differences between the measured and calculated surface voltages. First the algorithm calculates the potential and current densities with Neumann boundary conditions. From these calculations, the voltages at the surface nodes are obtained. These voltages are compared with actual voltage measurements. Unless the exact conductivity distribution is known in advance, there will be a discrepancy and the potential distribution is calculated again with Dirichlet boundary condition. This means that a large number of conductivity-updating iterations are needed. The algorithm was tested with a three dimensional laboratory experiment with top surface measurements only. A submerged metallic object was imaged with error that was believed to be due to poor modelling of fields in the vicinity of the electrodes.

In [27], methods for resolving the forward and inverse problems in 3D were proposed. The forward and inverse computations were based on the continuum electrode model [17] and its analytical solution. For this reason the proposed approach can be used for the cylindrical objects only.

A direct sensitivity matrix (DSM) approach for fast 3D image reconstruction was proposed in [67]. There is no need for inversion of DSM, and the reconstructed image of conductivity change is obtained directly by the product of the DSM and the difference between two measurement vectors. This is obtained by assuming that the matrix $(S^TS)^{-1}S^T$ where S is a sensitivity matrix (the Jacobian), could be approximated with the DSM where the matrix elements are the inverses of

the corresponding elements of S. This is a very crude approximation and it is not guaranteed that it works properly. Further, the boundary element method was used in construction of this matrix. This restricts the generality of resistivity distribution since the boundary element method requires that the areas surrounded by the given boundaries have the same value of resistivity.

A modification of the "classical" sensitivity method for the 3D image reconstruction was used in [63, 64]. An image reconstruction algorithm based on the sensitivity matrix S has been utilized such that the relationship between the measured boundary data ΔU to the change in conductivity image $\Delta\sigma$ is $\Delta U = S\Delta\sigma$ where ΔU is a difference between a perturbed data set U and the uniform case U_u, and similarly for $\Delta\sigma$. Each sensitivity coefficient is given with voltage gradients which are found by calculating the node potentials of each element using the approximation $u = r_1^{-1} - r_2^{-1}$ where r_1 and r_2 are the distances of the image point to the current injecting and voltage measurement electrode pairs. The sensitivity matrix is normalized by pre-multiplying S with a diagonal matrix where the non-zero elements correspond to a theoretical U_u data set which can be calculated from the node potentials at the electrode sites. The drawbacks of this approach are that the forward model is very inaccurate, for example, it does not depend on the estimated parameters σ and the method can only be used for the difference imaging. In [65] the proposed method was applied to 3D EIT of the human thorax.

There have also been attempts to exploit three-dimensional aspects in two-dimensional reconstruction algorithms, instead of producing fully 3D reconstruction [24, 40, 83, 82]. In [24] three-dimensional measurements were used for two-dimensional reconstruction. They used three rings of 16 electrodes, one centrally and the other two 10 cm on both sides of the central electrode plane. The measurements were obtained for uniform resistivity throughout the model and also for two perturbations in resistivity introduced, one on the central plane and the other in the midway between the central and lower electrode plane. The measurements on the three rings of electrodes were used individually to reconstruct the resistivity distributions on the respective plane. The objects on the upper and lower planes were clearly visible also in the reconstruction corresponding to the central plane. It was suggested to subtract in the "appropriate" proportion normalized images of the upper and lower planes from the central image. In this way the perturbation caused by the off-plane target disappeared in the central plane image.

In [83, 82], the effect of the third dimension on 2D EIT was studied. The work was based on the applied potential tomography system, [4], and a cylindrical phantom containing saline. Experimentally obtained magnitudes of pixel values corresponding to different conditions in the third dimension were presented. The analysis of these data yielded two observations. First, planes of changed resistivity out of the electrode plane can appear as both increased and decreased resistivity in the image. Secondly, it was found that the image of an object is shifted in position toward the centre almost linearly with distance from the electrode plane in z-direction and that the slope of this linear variation depends on the radial distance of object. This observation has been utilized in [82]. They fitted an empirical curve to this dependence and based on this, developed a method to

locate 3D objects using only two electrode planes.

Often when fully 3D EIT has been considered, simplified geometrical and mathematical models have been used [113, 27, 63, 67, 64, 65, 39, 68, 69, 11]. This makes it possible to solve the image reconstruction problem with the aid of (semi)analytical methods. This approach is applicable in difference imaging in the situations where the object is assumed to be geometrically simple. However, in the cases of absolute imaging and complex geometries accurate modelling is needed, and furher, numerical methods, such as FEM are needed for solving the forward problem in the static image reconstruction. The FEM solution of the most accurate model, the complete electrode model, was first published by the author of this thesis, [85, 109, 108, 103]. In order to solve the forward problem accurately enough for the static reconstructions the complete electrode model and FEM with second order basis functions (also called shape functions, see [12, 35]) were used. The FEM approximation of the complete electrode model has also been implemented in refs [81, 80].

Infinite elements

There are many situations in engineering which involve unbounded domain. Specific examples can be found in fields such as fluid mechanics, acoustics, electromagnetics, heat and mass transfer. Also decay of the voltages along one axis in EIT, for example, in a human leg or a long pipe in industrial applications is approximately a problem like this. The most common way to solve these problems is to limit the studied volume at finite distance on which adequate conditions on the field variables are imposed. This method requires a large number of finite elements leading to a large system of equations. This increases computing time and computer storage required for reconstuction. Another way is to use "longer" elements on the boundary. This leads often to ill-conditioned elements and inaccurate solutions.

The development of infinite elements has helped in the proper physical modelling of the far field behavior and in the reduction of the number of elements. The infinite element method, which involves the choosing of the shape functions so that they extend to infinity, has been described in [8]. In the so-called mapped infinite element method the known local element is mapped to the infinite element whose node(s) of some boundary are at infinity. This method has been used in [6, 61, 90, 118]. A similar idea has also been used with infinite boundary elements in [7].

The formulation of the infinite element depends on the type of decay that is to be incorporated. In general, the types of the decay which are adopted are $\frac{1}{r^n}$, with $\frac{1}{r}$, $\frac{1}{r^2}$ and $\frac{1}{\sqrt{r}}$ as the special cases of decay, where r is the distance from the chosen pole to a general point within the element. In [110] three-dimensional hexahedral infinite elements with $\frac{1}{r}$ and $\frac{1}{\sqrt{r}}$ decay have been presented. In [78] some techniques for testing infinite elements have been presented for the exponential, $\frac{1}{r}$ and $\frac{1}{\sqrt{r}}$ decays. The formulation of infinite elements has been tested by synthesizing special differential equations. Often these new differential equations are not those which will be eventually solved by the infinite elements, but other equations which are

simpler, and preserve the properties of the final differential equation.

The infinite elements method was applied to EIT by the author of this thesis in [104, 105]

Aims and contents of this thesis

In this thesis the three-dimensional recontruction in EIT is considered. The main aims of the thesis are:

1. To present the implemetation of the FEM approximation for the 3D complete electrode model,
2. to compare different iterative reconstruction methods in EIT, including a novel block-nonlinear conjugate gradient method, and
3. to apply the infinite elements method to EIT.

In most of the realistic EIT problems, for example head imaging, thousands of unknown conductivity (resistivity) have to be determined. These computations take a lot of computer time and storage. Hence the solution methods plays a significant role. Because of the nonlinearity and ill-posedness of EIT standard optimization approaches can not be utilized. In this thesis different types of iterative optimization methods for the solution the inverse problem have been studied A special nonlinear conjugate-gradient method for 3D EIT is proposed. The advantage of the conjugate-gradient methods is that the expence of inverting large dimensional matrices can be avoided. In addition, in the proposed block-nonlinear conjugate-gradient method the gradients needed for the search direction can be computed in separate blocks. This reduces further the need of storage in the computation and allows parallelization. The proposed approaches are tested and results are compared with computer simulations.

The model truncation problem has been solved with infinite elements. The idea that the three-dimensional basis functions can be separable has been used. In the case of the separable basis functions, the integrals over the three-dimensional infinite elements can be replaced by the integrals over the two-dimensional and one-dimensional elements. In this work, a cylindrical volume is assumed to be an unbounded domain only in one direction, so that simple one dimensional infinite elements can also be used in 3D. The accuracy of the solutions with separable infinite elements, long finite elements and separable finite elements has also been compared.

This thesis is divided into six chapters. After Introduction in Chapter 1, different types of optimization methods is presented. In Chapter 3, the forward problem in EIT is discussed. The variational form for the complete electrode model is presented and finite element method and infinite element method in EIT is considered. The theory of inverse problem in case of EIT is discussed in Chapter 4. In Chapter 5, reconstructions with simulated data in static cases are given. Chapter 6 is a discussion chapter in which the results of the whole thesis are summed up and suggestions for further development are given.

CHAPTER II

On the theory of optimization methods

There are many different types of optimization problems and each type needs different solution method. Special algorithms have been developed for solving *linear* or *nonlinear problems*. Different types of solution methods are also needed when the model includes or does not include explicit constraints on the variables (called *constrained problems* or *unconstrained problems*). When the method is chosen the property of solution has to be considered as well. The fastest algorithms only seek a local solution instead of real minimum/maximum (global) solution. Global solutions are necessary in some applications, but they are usually difficult to identify and locate. Sometimes the already existing standard methods can be utilized but unfortunately many problems require a solution method tailored just for the given problem.

Most of the optimization methods are iterative. They begin with an initial guess and generate a sequence of improved estimates until the optimal solution is obtained. Some methods need a good initial guess in order to be able to converge to the global minimum (or maximum). These type of methods can not be used if there is not enough prior information on the sought solution. The strategies used to move from one iterate to the next differ from one method to the other. The algorithms which are based on *Newton method* use derivatives (first or second) for choosing the direction in the iteration. Very often these methods converge fast but computation of the derivatives takes a lot of computer time and storage especially in large dimensional problems with thousands of variables. The biggest problem of these methods is that also the inversion of the large dimensional matrices that includes the derivatives has to be computed. For large dimensional problems methods that avoid inversion of these large dimensional matrices are much more favorable.

In this chapter the optimization methods for both linear and non-linear unconstrained problems are discussed in general. The gradient based iterative methods which can be utilized in three-dimensional electrical impedance tomography will be considered.

2.1 Line search methods

Let us denote a multivariable function which has to be minimized by $F(x)$ where x is a real n-vector $x = (x_1, x_2, ..., x_n)^T$ and $F : \mathbb{R}^n \to \mathbb{R}$.

Each iteration of line search method computes a search direction p_k and then decides how far to move along that direction. The iteration is given by

$$x_{k+1} = x_k + \alpha_k p_k \ , \tag{2.1}$$

where the positive scalar α_k is called the step length. The step length tells how far from the point x_k one moves to the direction p_k. The success of a line search method depends on effective choices for both p_k and α_k. In computing the step length α_k, compromises have to be made. On one hand α_k should be chosen such that it gives a substantial reduction of minimized function F and on the other hand the time that is taken to choose α_k should not be too long. In practice *inexact* line search is used to compute a step length that achieves adequate reductions in F at minimal cost. In next sections different strategies to choose step length α_k and search direction p_k is discussed.

2.1.1 Inexact line search

As explained earlier, inexact line search is problematic but has significant role in convergence rate of the method. Step parameter should be chosen as accurately as possible, but at the same time too much time is not wanted to be used for numerous iterations. A standard choice for the step parameter is $\alpha_k = 1$. This in not effective way because convergence rate is going to be slow if optimal or even close to optimal α_k is not used. This can also lead to the situation in which the minimum can not be found at all even if the search direction is good.

Let us denote $\phi(\alpha_k) = F(x_k + \alpha_k p_k) = (F \circ g)(\alpha_k)$ where $g(\alpha_k) = x_k + \alpha_k p_k$. By using the chain rule of the partial differentiation of the composite function the derivative of $\phi(\alpha_k)$

$$\frac{\mathrm{d}\phi(\alpha_k)}{\mathrm{d}\alpha_k} = \sum_{i=1}^{n} \frac{\partial F(g(\alpha_k))}{\partial x_{k,i}} \frac{\partial g_i(\alpha_k)}{\partial \alpha_k} \tag{2.2}$$

$$= \sum_{i=1}^{n} \frac{\partial F(g(\alpha_k))}{\partial x_{k,i}} p_{k,i} \tag{2.3}$$

$$= \nabla F(x_k + \alpha_k p_k)^T p_k \ , \tag{2.4}$$

where $\nabla F = (\frac{\partial F}{\partial x_1}, \cdots, \frac{\partial F}{\partial x_n})$, is obtained. The simplest condition which α_k has to fulfill is that $F(x_k + \alpha_k p_k) < F(x_k)$. One choice to choose α_k such that the previous condition is fulfilled is

$$F(x_k + \alpha_k p_k) \leq F(x_k) + c_1 \alpha_k \nabla F(x_k)^T p_k \tag{2.5}$$

where $0 < c_1 < 1$ and $\nabla F(x_k)^T p_k$ is the derivative of ϕ_{α_k} at $\alpha_k = 0$ [75]. Because p_k is descent direction $\nabla F(x_k)^T p_k < 0$ (see the next section on steepest descent

method). The condition (2.5) is called *the Armijo condition*. The step parameter α_k is acceptable only if $\phi(\alpha_k)$ is below or equal with the line $l(\alpha_k) = F(x_k) + c_1\alpha_k\nabla F(x_k)^T p_k$. Because of parameter c_1 the line $l(\alpha_k)$ lies above the graph $\phi(\alpha_k)$ also for very small values of α_k. Step lengths satisfying Armijos condition are shown in Fig. 2.1. The Armijo condition by itself is not an efficient way

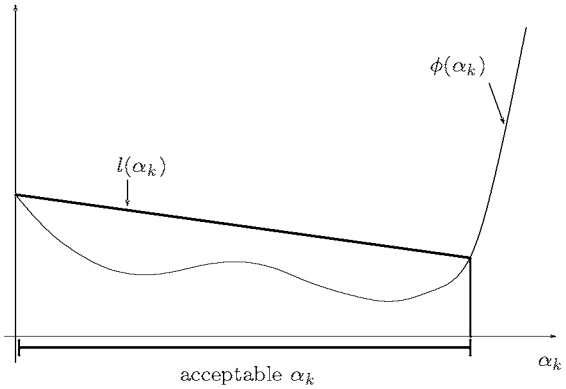

Figure 2.1: Step lengths satisfying the Armijo condition.

to choose step parameters, because it is satisfied for all small values of α_k and therefore convergence can be very slow. By setting that the derivative at α_k has to be greater than gradient at 0, that is,

$$\nabla F(x_k + \alpha_k p_k)^T p_k \geq c_2 \nabla F(x_k)^T p_k \ , \tag{2.6}$$

where $c_2 \in]c_1, 1[$, it can be ensured that α_k is not "too small" and more efficient convergence can be obtained. The condition (2.6) is called *the curvature condition* and together with the Armijo condition they are known as *the Wolfe conditions* Step lengths satisfying the Wolfe conditions are shown in Fig. 2.2. It is not guaranteed that the slope of tangent at α_k, which fulfills both of the Wolfe conditions, is negative. In order to ensure that the slope is not too positive and on the other hand that α_k is not too far from the stationary point of $\phi(\alpha_k)$ the Wolfe condition (2.6) can be written as

$$|\nabla F(x_k + \alpha_k p_k)^T p_k| \leq c_2 |\nabla F(x_k)^T p_k| \tag{2.7}$$

The Armijo condition and condition (2.7) are known as *the strong Wolfe conditions* see Fig. 2.3.

There are also other conditions for choosing step parameters (see for example [22, 26, 75]). Like Armijo, Wolfe and strong Wolfe conditions they are based on computation of gradients at several points during the calculations of α_k. In practice, gradients are expensive to compute and therefore it is advisable to use less expensive methods. For example, the gradient at α_k can be approximated by

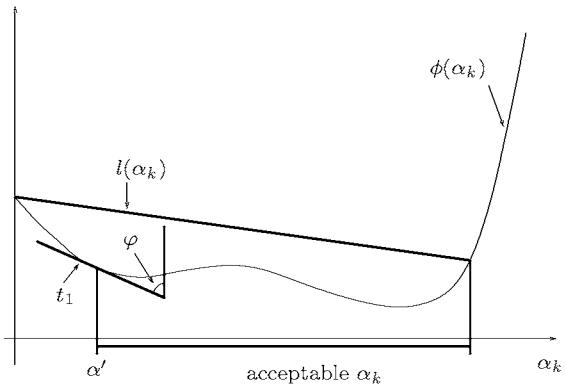

Figure 2.2: Step lengths satisfying the Wolfe conditions. Line t_1 is the tangent line at $\alpha_k = \alpha'_k$ such that slope of tangent at α'_k is greater than slope of tangent when $\alpha_k = 0$.

the difference quotient and the equation (2.7) takes the form

$$\frac{|F(x_k + \alpha_k p_k) - F(x_k + \nu p_k)|}{\alpha_k - \nu} \leq c_2 |\nabla F(x_k)^T p_k| \ , \tag{2.8}$$

where $\nu \in [0, \alpha_k[$ [26].

If $\phi(\alpha_k)$ is known to be almost quadratic, an effective way to choose the step parameter is to compute $\phi(\alpha_k)$ with few different values of α_k and then fit a quadratic function to the data. For the known quadratic function the minimum point α_k^* is easy to compute.

2.1.2 Steepest descent method

Consider the linear approximation to F based on the Taylor-series expansion as

$$F(x_k + p_k) \approx F(x_k) + \nabla F(x_k)^T p_k \ , \tag{2.9}$$

where ∇F is the gradient of F and $x_k \in \mathbb{R}^n$. Since the function F is to be minimized a step along p_k is taken such that $F(x_k + p_k) < F(x_k)$ which means that every p_k that satisfies the condition $\nabla F(x_k)^T p_k < 0$ is a descent direction. If the direction is chosen to be $p_k = -\nabla F(x_k)$ the method is called *steepest descent method*. This can also be obtained from the expression of the vectors

$$\nabla F(x_k)^T p_k = \|\nabla F(x_k)\|_2 \|p_k\|_2 \cos\theta \ , \tag{2.10}$$

where θ is the angle between the vectors $\nabla F(x_k)$ and p_k. Since $\cos\theta$ lies between -1 and 1, $p_k^T \nabla F(x_k)$ will be minimized when θ is π, in other words $p_k = -\nabla F(x_k)$. This direction is orthogonal to the equipotential curves of the minimized function. Therefore the steepest descent method can be formulated as

$$x_{k+1} = x_k - \alpha_k \nabla F(x_k) \ . \tag{2.11}$$

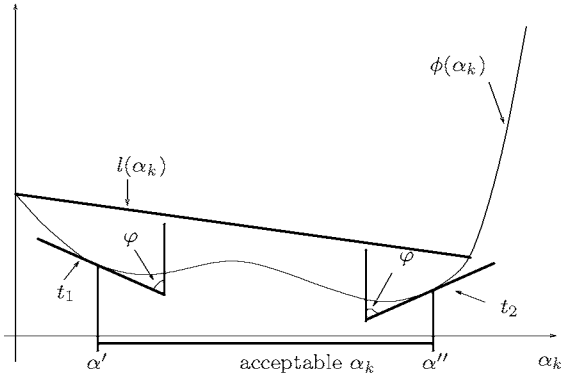

Figure 2.3: Step lengths satisfying the strong Wolfe conditions. Line t_1 is the tangent line at $\alpha_k = \alpha'_k$ and line t_2 is the tangent line at $\alpha_k = \alpha''_k$ such that absolute values of slope of tangents at all $\alpha_k \in [\alpha'_k, \alpha''_k]$ are smaller than absolute value of slope of tangent when $\alpha_k = 0$.

Advantages of the steepest descent method are that it has guaranteed convergence and it requires only calculation of the gradient $\nabla F(x_k)$ but not of second derivatives. Disadvantage of the method is that its convergence can be quite slow. Even in ideal case in which the objective function F is quadratic (smooth function) and choosing α_k are exact the convergence rate is linear.

2.1.3 Newton's method

Traditional Newton method has been used to find the zero point of nonlinear functions $f(x)$, $f : \mathbb{R} \to \mathbb{R}$. The basic idea in this method is that if x_0 is an approximation (first guess) to the zero point of $f(x)$ then a closer approximation will be given by a point $x = x_1$ where the tangent to the graph at $x = x_0$ cross the x axis. The tangent can be taken as a linearization for the $f(x)$ in x_0. Point x_1 is chosen to be a new approximation to the zero point and new linearization is done. This is repeated until the approximation is accurate enough. Hence the iterative method

$$x_{k+1} = x_k - \alpha_k (f'(x_k))^{-1} f(x_k) \tag{2.12}$$

for solving the zero point is obtained. When the stationary point of the nonlinear function is searched instead of zero point then the zero point of the derivative function is needed. Thus the derivative function is linearized instead of original nonlinear function. The Newton method for solving the stationary point will be formulated in this section.

If the minimized function $F(x)$, $F : \mathbb{R}^n \to \mathbb{R}$, can be assumed to be almost quadratic, a good choice is to use quadratic approximation for $F(x)$. A quadratic function is one of the simplest smooth functions with well determined minimum. If first and second derivatives of minimized function F are available, a quadratic

model of the objective function can be obtained by taking the first three terms of the Taylor-series expansion about the current point

$$F(x_k + p_k) \approx F(x_k) + \nabla F(x_k)^T p_k + \frac{1}{2} p_k^T \nabla^2 F(x_k) p_k \ , \tag{2.13}$$

where $\nabla F(x_k)^T = (\frac{\partial F(x_k)}{\partial x_1}, \cdots, \frac{\partial F(x_k)}{\partial x_n})$ and $\nabla^2 F(x_k)$ is a symmetric matrix (Hessian matrix)

$$\nabla^2 F(x) = \nabla(\nabla F)^T = \begin{bmatrix} \frac{\partial^2 F}{\partial x_1^2} & \frac{\partial^2 F}{\partial x_1 \partial x_2} & \cdots & \frac{\partial^2 F}{\partial x_1 \partial x_n} \\ \frac{\partial^2 F}{\partial x_2 \partial x_1} & \frac{\partial^2 F}{\partial x_2^2} & \cdots & \frac{\partial^2 F}{\partial x_2 \partial x_n} \\ \vdots & \vdots & \ddots & \vdots \\ \frac{\partial^2 F}{\partial x_n \partial x_1} & \frac{\partial^2 F}{\partial x_n \partial x_2} & \cdots & \frac{\partial^2 F}{\partial x_n^2} \end{bmatrix} \tag{2.14}$$

where $\frac{\partial^2 F}{\partial x_i \partial x_j} = \frac{\partial^2 F}{\partial x_j \partial x_i}$

As in the steepest descent case the condition to be fulfilled is $F(x_k + p_k) < F(x_k)$ which can be obtained if p_k is a minimum point of the quadratic function

$$\phi(p_k) = \nabla F(x_k)^T p_k + \frac{1}{2} p_k^T \nabla^2 F(x_k) p_k \ . \tag{2.15}$$

By differentiating the function (2.15) with respect to p_k, and letting $\nabla_{p_k} \phi(p_k) = 0$

$$\nabla_{p_k} \phi(p_k) = \nabla F(x_k) + \frac{1}{2} \left(\nabla^2 F(x_k)^T + \nabla^2 F(x_k) \right) p_k \tag{2.16}$$

$$= \nabla F(x_k) + \nabla^2 F(x_k) p_k = 0 \tag{2.17}$$

which can be written in the form

$$\nabla F(x_k) = -\nabla^2 F(x_k) p_k \tag{2.18}$$

from which p_k can be solved

$$p_k = -\left(\nabla^2 F(x_k) \right)^{-1} \nabla F(x_k) \ . \tag{2.19}$$

The stationary point p_k is the unique minimum of the equation (2.15) if the second derivative of $\phi(p_k)$ $(= \nabla^2 F(x_k))$ is positive definite. The direction (2.19) is called *Newton direction*. Therefore *Newton's method* can be formulated as

$$x_{k+1} = x_k - \alpha_k \left(\nabla^2 F(x_k) \right)^{-1} \nabla F(x_k) \ . \tag{2.20}$$

If $\nabla^2 F(x_k)$ is positive definite, only one iteration is required to reach the minimum of the function (2.13) from any starting point x_0 which is also the minimum of $F(x)$ if $F(x)$ is quadratic. Convergence rate of Newton's method is quadratic if the starting point is sufficiently close to minimum point x^* (this means that the quadratic model is a good approximation for the function F), the Hessian matrix

is positive definite at x^* and Lipschitz continuous in the neighborhood. If the Hessian matrix is not positive definite, the quadratic approximation (2.13) does not have a minimum. It may not even have a stationary point. Numerous strategies have been developed to produce an efficient descent method for the indefinite and negative definite cases. These methods, called a *modified Newton Methods*, do not use Newton direction under all circumstances [26, 75].

The effectiveness of Newton's method is based on curvature information provided by the Hessian matrix. However, in practice the Hessian is quite often impossible or difficult to compute or computing takes too much time. Especially, obtaining the inverse of the Hessian is very demanding and needs a lot of computer storage. The methods in which approximation to curvature of a nonlinear function can be computed without explicitly forming the Hessian matrix have been developed. These methods are called *Quasi-Newton Methods*. Also the inverse of Hessian can be approximated directly instead of Hessian (see BFGS-method (Brouden-Fletcher-Goldfarb-Shanno) [22]). In *Discrete Newton Methods* the Hessian matrix is approximated by finite-difference approximations of the gradients.

2.1.4 Newton-Raphson method

Let us consider the situation in which the minimized function F is of form

$$F(x) = \frac{1}{2} r(x)^T r(x) = \frac{1}{2} \|r(x)\|_2^2 \,, \tag{2.21}$$

where $r(x) = (r_1(x), r_2(x), ..., r_m(x))^T$ is a function $r : \mathbb{R}^n \to \mathbb{R}^m$. Now the gradient of F is (note that $\nabla(a^T b) = (\nabla a^T)b + (\nabla b^T)a$ where a and b are vectors)

$$\begin{aligned}
\nabla F(x) &= \frac{1}{2} \nabla \left(r(x)^T r(x) \right) && (2.22)\\
&= \left(\nabla r(x)^T \right) r(x) && (2.23)\\
&= \left(\begin{bmatrix} \frac{\partial}{\partial x_1} \\ \frac{\partial}{\partial x_2} \\ \vdots \\ \frac{\partial}{\partial x_n} \end{bmatrix} \begin{bmatrix} r_1 & r_2 & \cdots & r_m \end{bmatrix} \right) r(x) && (2.24)\\
&= \begin{bmatrix} \frac{\partial r_1}{\partial x_1} & \frac{\partial r_2}{\partial x_1} & \cdots & \frac{\partial r_m}{\partial x_1} \\ \frac{\partial r_1}{\partial x_2} & \frac{\partial r_2}{\partial x_2} & \cdots & \frac{\partial r_m}{\partial x_2} \\ \vdots & \vdots & \ddots & \vdots \\ \frac{\partial r_1}{\partial x_n} & \frac{\partial r_2}{\partial x_n} & \cdots & \frac{\partial r_m}{\partial x_n} \end{bmatrix} r(x) && (2.25)\\
&= (J^{(\mathrm{r})}(x))^T r(x) && (2.26)
\end{aligned}$$

where $J^{(\mathrm{r})}(x) \in \mathbb{R}^{m \times n}$ such that $J^{(\mathrm{r})}(x)_{ij} = \frac{\partial r_i(x)}{\partial x_j}$ is called the Jacobian of r. Let us denote $J^{(\mathrm{r})} = (J_1^{(\mathrm{r})}, J_2^{(\mathrm{r})}, ..., J_n^{(\mathrm{r})})$ where $J_j^{(\mathrm{r})}$ is j'th column of $J^{(\mathrm{r})}$. Hessian of

F is now

$$\nabla^2 F(x) = \nabla \left(\nabla F(x)\right)^T \tag{2.27}$$

$$= \nabla \left((J^{(\mathrm{r})}(x))^T r(x) \right)^T \tag{2.28}$$

$$= \nabla (r(x)^T J^{(\mathrm{r})}) \tag{2.29}$$

$$= \left(\begin{bmatrix} \frac{\partial}{\partial x_1} \\ \frac{\partial}{\partial x_2} \\ \vdots \\ \frac{\partial}{\partial x_n} \end{bmatrix} \begin{bmatrix} r^T J_1^{(\mathrm{r})} & r^T J_2^{(\mathrm{r})} & \cdots & r^T J_n^{(\mathrm{r})} \end{bmatrix} \right) \tag{2.30}$$

$$= \begin{bmatrix} \frac{\partial (r^T J_1^{(\mathrm{r})})}{\partial x_1} & \cdots & \frac{\partial (r^T J_n^{(\mathrm{r})})}{\partial x_1} \\ \vdots & \ddots & \vdots \\ \frac{\partial (r^T J_1^{(\mathrm{r})})}{\partial x_n} & \cdots & \frac{\partial (r^T J_n^{(\mathrm{r})})}{\partial x_n} \end{bmatrix} \tag{2.31}$$

$$\tag{2.32}$$

$$= \begin{bmatrix} \frac{\partial r^T}{\partial x_1} J_1^{(\mathrm{r})} & \cdots & \frac{\partial r^T}{\partial x_1} J_n^{(\mathrm{r})} \\ \vdots & \ddots & \vdots \\ \frac{\partial r^T}{\partial x_n} J_1^{(\mathrm{r})} & \cdots & \frac{\partial r^T}{\partial x_n} J_n^{(\mathrm{r})} \end{bmatrix} + \begin{bmatrix} r^T \frac{\partial J_1^{(\mathrm{r})}}{\partial x_1} & \cdots & r^T \frac{\partial J_n^{(\mathrm{r})}}{\partial x_1} \\ \vdots & \ddots & \vdots \\ r^T \frac{\partial J_1^{(\mathrm{r})}}{\partial x_n} & \cdots & r^T \frac{\partial J_n^{(\mathrm{r})}}{\partial x_n} \end{bmatrix} \tag{2.33}$$

$$= \begin{bmatrix} \frac{\partial r^T}{\partial x_1} \\ \vdots \\ \frac{\partial r^T}{\partial x_n} \end{bmatrix} \begin{bmatrix} J_1^{(\mathrm{r})} & \cdots & J_n^{(\mathrm{r})} \end{bmatrix} + \begin{bmatrix} \sum_{i=1}^{m} r_i \frac{\partial^2 r_i}{\partial x_1^2} & \cdots & \sum_{i=1}^{m} r_i \frac{\partial^2 r_i}{\partial x_1 \partial x_n} \\ \vdots & \ddots & \vdots \\ \sum_{i=1}^{m} r_i \frac{\partial^2 r_i}{\partial x_n \partial x_1} & \cdots & \sum_{i=1}^{m} r_i \frac{\partial^2 r_i}{\partial x_n^2} \end{bmatrix} \tag{2.34}$$

$$= (J^{(\mathrm{r})}(x))^T J^{(\mathrm{r})}(x) + \sum_{i=1}^{m} r_i(x) G_i^{(\mathrm{r})}(x) \ , \tag{2.35}$$

where $G_i^{(\mathrm{r})}(x) = \nabla^2 r_i(x)$. Now the equation (2.20) takes the form

$$x_{k+1} = x_k - \alpha_k \left((J^{(\mathrm{r})}(x_k))^T J^{(\mathrm{r})}(x_k) + \sum_{i=1}^{m} r_i(x_k) G_i^{(\mathrm{r})}(x_k) \right)^{-1} \cdot J^{(\mathrm{r})}(x_k)^T r(x_k) \tag{2.36}$$

and it is called *Newton-Raphson method*. As can be seen it is a special case of Newton's method.

2.2 Linear and nonlinear least squares problems

Newton-Raphson method is often applied for solving *linear (*or *nonlinear) least-squares* problems. First, let us look at the finite-dimensional linear forward problem which corresponds the measurement situation in which measurements (observations) includes error. This observation model is of the form

$$z = H\,\theta + v \tag{2.37}$$

where v is the error vector of the observations z, θ is the vector of parameters to be determined (corresponds to x in previous sections), H is the mathematical model between z and θ. Columns of H are assumed to be linearly independent. The system of equations $z = H\,\theta$ is often over determined so θ has to be chosen such that it represents real θ as well as possible in "some sense". In least square (LS) estimation the estimator $\widehat{\theta}_{LS}$ for the parameter θ is obtained by choosing parameters such that the squared sum of the errors $z_i - (H\theta)_i$ will be minimized. Now the minimized function $F(\theta)$ is of form

$$\begin{aligned} F(\theta) &= \frac{1}{2}\sum_{i=1}^{n} v_i^2 = \frac{1}{2} v^T v && (2.38)\\ &= \frac{1}{2}(z - H\,\theta)^T (z - H\,\theta) && (2.39)\\ &= \frac{1}{2}\|z - H\,\theta\|_2^2 && (2.40) \end{aligned}$$

Let us differentiate the equation (2.39) with respect to θ

$$\begin{aligned} \nabla F(\theta) &= \frac{1}{2}\left(\frac{\partial}{\partial\theta}(z - H\,\theta)^T (z - H\,\theta)\right) && (2.41)\\ &= \frac{\partial (z - H\,\theta)^T}{\partial\theta}(z - H\,\theta) && (2.42)\\ &= -H^T (z - H\,\theta) && (2.43) \end{aligned}$$

Hence the stationary point $\widehat{\theta}_{LS}$ is

$$\widehat{\theta}_{LS} = (H^T H)^{-1} H^T z\ . \tag{2.44}$$

The least square estimator $\widehat{\theta}_{LS}$ is the unique minimum of the equation (2.39) if $\frac{\partial^2 F(\theta)}{\partial\theta^2} = H^T H$ is a positive definite matrix.

If observations are nonlinearly dependent on parameters θ, in other words $z = h(\theta) + v$ where $h(\theta) = (h_1(\theta), \ldots, h_m(\theta)$ ($h \in C^2$, that is, h is two times continuously differentiable), the functional $F(\theta)$ which has to be minimized is of form

$$F(\theta) = \frac{1}{2}\|z - h(\theta)\|_2^2 \tag{2.45}$$

It can be seen that the equation (2.45) equals the equation (2.21) with $r(\theta) = z - h(\theta)$ when the minimum of the equation (2.45) can be obtained from the

equation (2.36). The Jacobian matrix of $r(\theta)$ is needed and can be computed as $J^{(\mathrm{r})}(\theta)_{ij} = \frac{\partial(z_i - h_i(\theta))}{\partial\theta_j} = -\frac{\partial h_i(\theta)}{\partial\theta_j} = -J_{ij}$, where J denotes the Jacobian of the function $h(\theta)$. Similarly the Hessian of $h_i(\theta)$ is $G_i = G_i^{(\mathrm{r})}$. With these notations, the equation (2.36) takes the form

$$\widehat{\theta}_{k+1} = \widehat{\theta}_k + \alpha_k \left(J_k^T J_k + \sum_{i=1}^{m} \left(z_i - h_i(\widehat{\theta}_k) \right) G_i(\widehat{\theta}_k) \right)^{-1} J_k^T \left(z - h(\widehat{\theta}_k) \right) \ . \quad (2.46)$$

where $J_k = J(\widehat{\theta}_k)$, $J_k \in \mathbb{R}^{m \times n}$.

2.2.1 Gauss-Newton method

Computing of Hessian is very time and memory consuming. In order to reduce the computational burden the Hessian of F can be approximated in several ways. One possibility is the approximation in which the Hessian is of the form

$$\nabla^2 F(\theta) \approx J(\theta)^T J(\theta) \ . \quad (2.47)$$

This approximation is valid if the initial guess is close to minimum θ^*, in other words, $h(\widehat{\theta}_0) \approx z$ or $r(\widehat{\theta}) = z - h(\widehat{\theta}_0) \approx 0$, that is, the residual is very small. Then the term $\sum_{i=1}^{m} \left(z_i - h_i(\widehat{\theta}_k) \right) G_i(\widehat{\theta}_k)$ is negligible. The same approximation can be used if the model $h(\widehat{\theta}_k)$ is nearly linear in the neighborhood of $\widehat{\theta}_k$ and therefore G_i is almost zero. Hence the iteration (2.46) can be written in the form

$$\widehat{\theta}_{k+1} = \widehat{\theta}_k + \alpha_k \left(J(\widehat{\theta}_k)^T J(\widehat{\theta}_k) \right)^{-1} J(\widehat{\theta}_k)^T \left(z - h(\widehat{\theta}_k) \right) \ . \quad (2.48)$$

This is called *Gauss-Newton method* [10].

The same result can be obtained using *Gauss' method* in which nonlinear $h(\theta)$ is approximated with a linear function in the neighborhood of some θ_0 [92]

$$h(\theta) \approx h(\theta_0) + J(\theta_0)(\theta - \theta_0) \quad (2.49)$$

where J is the Jacobian of h.

Now the functional which has to be minimized can be written as ($J = J(\theta_0)$)

$$\begin{aligned} F(\theta) &= \frac{1}{2}\|z - h(\theta)\|^2 && (2.50)\\ &\approx \frac{1}{2}\|z - h(\theta_0) - J(\theta - \theta_0)\|^2 && (2.51)\\ &= \frac{1}{2}\|z - h(\theta_0) + J\,\theta_0 - J\,\theta\|^2 && (2.52)\\ &= \frac{1}{2}\|z' - J\,\theta\|^2 && (2.53) \end{aligned}$$

where

$$z' = z - h(\theta_0) + J\,\theta_0 \ . \quad (2.54)$$

The LS solution corresponding to this linear approximation is

$$\begin{aligned}
\widehat{\theta}_{LS} &= (J^T J)^{-1} J^T z' && (2.55)\\
&= (J^T J)^{-1} J^T (z - h(\theta_0) + J\,\theta_0) && (2.56)\\
&= (J^T J)^{-1} J^T z - (J^T J)^{-1} J^T h(\theta_0) + (J^T J)^{-1} J^T J\,\theta_0 && (2.57)\\
&= \theta_0 + (J^T J)^{-1} J^T (z - h(\theta_0)) \ . && (2.58)
\end{aligned}$$

The model $h(\theta)$ can be linearized again in $\widehat{\theta}_{LS}$ and the same step as in (2.58) can be used again. From this an iterative algorithm

$$\widehat{\theta}_{k+1} = \widehat{\theta}_k + \alpha_k \left(J(\widehat{\theta}_k)^T J(\widehat{\theta}_k) \right)^{-1} J(\widehat{\theta}_k)^T \left(z - h(\widehat{\theta}_k) \right) \qquad (2.59)$$

to solve the nonlinear problem is obtained. As can be seen it is the same as the algorithm (2.48).

2.3 Methods for ill-posed least squares problems

Let us consider the same observation model as in section 2.2 without the error v

$$z = H\,\theta \ , \qquad (2.60)$$

where $\theta \in \mathbb{R}^n$ is "a cause", $z \in \mathbb{R}^m$ is "a consequence" and $H \in \mathbb{R}^{m \times n}$ is the model between θ and z. The matrix equation (2.60) represents m linear equations in n variables ($H : \mathbb{R}^n \rightarrow \mathbb{R}^m$, $\mathbb{R}^n$ is called the *domain* of H and $\mathbb{R}^m$ denoted as $\mathcal{R}(H)$ is called the *range* of H). In the forward problem the parameters θ and the observation model H are known and the observations z are to be computed. The inverse problem corresponding the model given above can be divided in two categories

- Let z be the observed consequence and the model H is known. In that case the cause θ has to be determined.

- Let z be the observed consequence and θ the known cause. In that case the model H has to be determined. In practice this means that the "parametric" form of the model is known but some of these parameters are unknown.

If z=0, the set of equations (2.60) is called *homogeneous*. If $z \neq 0$ the set is *inhomogeneous*. It is known that the homogeneous set of equations $H\,\theta = 0$ has one trivial solution $\theta = 0$ or infinite number of solutions. These solutions compose the subspace called the *null-space* of H, denoted as $\mathcal{N}(H)$. Inhomogeneous set of equations does not necessarily have any solutions. If one solution θ_0 is known the set of all solutions is

$$\{\theta \,|\, \theta = \theta_0 + \theta_{\mathcal{N}} \ , \theta_{\mathcal{N}} \in \mathcal{N}(H)\} \ . \qquad (2.61)$$

As it can be seen, if homogeneous set of equations has only a trivial solution, that is, $\mathcal{N}(H) = \{0\}$, inhomogeneous set of equations has a unique solution $\theta = \theta_0$.

In next sections existence of the solution of the inhomogeneous set of equations is discussed more closely, that is, the inverse problems of the first category will be considered.

Rank-deficient problems

Row rank ($\Re_r(H)$) is the number of linearly independent rows of matrix H, such that $H \in \mathbb{R}^{m\times n}$, $\Re_r(H) \leq m$. Column rank ($\Re_c(H)$) is the number of the linearly independent columns of matrix H, so if $H \in \mathbb{R}^{m\times n}$, $\Re_r(H) \leq n$. Row rank and column rank are equal and they are called as rank of H ($\Re(H)$) and consequently $\Re(H) \leq \min\{m, n\}$. If $\Re(H) = \min\{m, n\}$ the matrix H is said to have *full rank* or it is *non-singular*. If $\Re(H) < \min\{m, n\}$ the matrix H is *rank-deficient* or *singular*.

In order to be able to consider if there is a unique classical solution for the set of equations (2.60) the augmented matrix $\widetilde{H} = [H\, z]$ is needed [51, 42]. If $\widetilde{H}$ and H have different rank there is no unique classical solution. When the two matrices have the same rank there is either one unique classical solution or infinite number of classical solutions. This can be realized by remembering that if equations are consistent, z is linear combination of the linearly independent column vectors of H, in other words, z must lie in the subspace of $\mathbb{R}^m$ spanned by the linearly independent columns of H. This can be denoted as $\Re(H) = \Re(\widetilde{H})$ which means that $z \in \mathbb{R}^m (= \mathcal{R}(H))$.

If H is square ($m = n$) and $\Re(H) = m$ (all columns and rows are linearly independent) the equation (2.60) has a unique solution θ for every z and therefore columns of H span the whole $\mathbb{R}^m$. Thus columns of H form *a basis for the range of* H. If $\Re(H) < \Re(\widetilde{H})$, z is not a linear combination of linearly independent column vectors of H, and therefore it does not lie in the subspace of $\mathbb{R}^m$ ($z \notin \mathbb{R}^m$) and the equations are inconsistent. In this case there is no classical solution for the set of equations.

Thus there are three possible cases.

- When $m = n$, $\Re(H) \leq m$, there is the same number of equations and variables. If all columns and rows are linearly independent H^{-1} exists and there is unique solution for the set of equations. If $\Re(H) = \Re(\widetilde{H}) < m$ there will be $m - \Re(H)$ number of free parameters in the solution. Therefore there are infinite number of the exact solutions. If $\Re(H) < \Re(\widetilde{H})$ there is no exact solution for the set of equations.

- When $m < n$, $\Re(H) \leq m$, there are more variables than equations, that is, the problem is *under determined*. If $\Re(H) = \Re(\widetilde{H})$ there will be $n - \Re(H)$ number of free parameters in the solution and infinite number of classical solutions. If $\Re(H) < \Re(\widetilde{H})$ there is no classical solution for the set of equations.

- When $m > n$, $\Re(H) \leq n$, there are more equations than variables, that is, the problem is *over determined*. If rank $\Re(H) = \Re(\widetilde{H})$ some of the equations are redundant and they can be ignored. There is a solution containing $n - \Re(H)$

number of free parameters. If H has full column rank, which means that $\Re(H) = n$, and $\Re(H) = \Re(\widetilde{H})$, the problem reduces to the non-singular square problem . Hence H^{-1} exists and the set of equations has a unique solution. Note that in case of over determined problem, full column rank does not guarantee that $z \in \mathbb{R}^m$ because the number of column vectors is less than the dimension of the range. If $\Re(H) < \Re(\widetilde{H})$ there is no exact solution.

In practice there are errors in the observations z, that is, $z = H\theta + v$ and therefore $z \notin \mathcal{R}(H)$. As noted earlier, there is no classical solution for the set of equations in that case. If H has full column rank the matrix $H^TH \in \mathbb{R}^{n\times n}$ is non-singular square matrix and therefore the set of equations $(H^TH)\theta = b$ is true for every $b \in \mathbb{R}^n$ and unique LS-estimate (2.44) exists. Note that if H is non-singular square matrix LS-estimate equals the unique classical solution $\widehat{\theta}_{LS} = (H^TH)^{-1}H^Tz = H^{-1}(H^T)^{-1}H^Tz = H^{-1}z$. For the full column rank matrix it is also true that the homogeneous set of equations $H\,\theta = 0$ has only trivial solution $\theta \equiv 0$.

As explained in section 2.2, in least square estimation the estimator is chosen such that the square sum of the errors will be minimized, in other words, square of the norm of the error vector will be minimized ($v^Tv = \|v\|_2^2$). Let us denote $H\,\theta \in \mathcal{R}(H)$. Norm of the error vector will be minimized when v is orthogonal to the vector $H\,\theta$, that is, $v \in \mathcal{R}(H)^\perp$ where $\perp$ indicates orthogonal complement.

In some problems $z \notin \mathcal{R}(H)$ and H is not full column rank matrix so there is no classical or unique LS-estimate for the set of equations. However, every vector H^Tz lies in the subspace spanned by the linearly independent columns of square matrix H^TH, that is, H^Tz is in the range of H^TH. Now the set of equations $H^TH\theta = H^Tz$ is always consistent and therefore there is always an infinite number of LS-solutions [10].

As seen earlier for the rank-deficient problems neither unique classical solution nor unique LS-solution exists. From the set of the infinite number of LS solutions, a solution has to be chosen based on some criteria. If there are infinite number of classical solutions, typically the solution is chosen to be the one that has the least norm. Also if there are infinite number of LS-solutions $\widehat{\theta}_{LS}$ who has least norm can be chosen to be the solution. The LS-solutions of the inhomogeneous problems are of form $\widehat{\theta}_{LS} = \widehat{\theta}_{LS_0} + \widehat{\theta}_{LS_\mathcal{N}}$, where $\widehat{\theta}_{LS_0}$ is a particular least squares solution and $\widehat{\theta}_{LS_\mathcal{N}} \in \mathcal{N}(H)$. The unique LS-solution of minimum norm can be obtained by choosing $\widehat{\theta}_{LS_\mathcal{N}} = 0$ and $\widehat{\theta}_{LS_0} \in \mathcal{N}(H)^\perp$.

Ill-conditioned problems

In some problems the matrix H in the observation model is nearly rank-deficient. These problems are called *ill-conditioned* or *ill-posed* problems. For ill-conditioned problems it is typical that a small perturbation in the observations (data) can lead to an enormous change in the solution. The condition number of H ($\kappa(H)$) indicates the maximum effect of perturbation on the solution and it can be computed from the equation $\kappa(H) = \|H\|_2\|H^\dagger\|_2 \geq 1$ where $H^\dagger$ is so-called pseudoinverse of

H. The condition number of the matrix $H^T H$ is square of the condition number of H, and thus, even if matrix H is only slightly ill-conditioned, that is, $\kappa(H)$ is "small", there is a big error in the LS-solution of the linear system. Hence, the LS-problem is *unstable*, that is, even in the case that a unique solution exists, it is highly biased.

A straightforward way to stabilize the LS-problem is to "regularize" the solution somehow. There are several known regularization methods such as the Levenberg-Marquardt method and Tikhonov regularization. In both methods the original minimization problem is modified in such a way that a stable solution exists. The truncated SVD method reviewed below is also one way of regularize the LS-solution. A more sophisticated approach for solving ill-posed problems, however, is to utilize prior information in the solution. In *statistical inversion* the *a priori* information of the parameters is written down in the form of probability distribution. Also, the solutions obtained in statistical inversion are actually probability distributions. However, point estimates, such as *Maximum a Posteriori* (MAP) estimate, are usually considered. With certain assumptions the MAP estimate can be written in the form of the (generalized) Tikhonov regularized solution, although the interpretation is different. Several types of spatial [47, 32, 56] and temporal [89] prior information has been utilized for example in the case of EIT. Although the construction of the prior plays a significant role in statistical inversion, it is important to notice that in many cases even the use of less informative priors leads to feasible solutions.

2.3.1 The singular value decomposition

The singular value decomposition (SVD) of the matrix $H \in \mathbb{R}^{m \times n}$ is a matrix decomposition for the treatment of least squares problems. The idea is that any $m \times n$ matrix can be written as

$$H = U \Sigma V^T \ , \tag{2.62}$$

where U is an $m \times m$ orthonormal unitary matrix, V is an $n \times n$ orthonormal unitary matrix and Σ is an $m \times n$ matrix such that

$$\Sigma = \begin{pmatrix} \Sigma_1 \\ 0 \end{pmatrix} \ , \tag{2.63}$$

where $\Sigma_1 = \mathrm{diag}(\sigma_1, \cdots, \sigma_n)$ with $\sigma_i \geq 0$ for all i. The numbers $\{\sigma_i\}$ are the *singular values* of H. They are normally ordered such that $\sigma_1 \geq \sigma_2 \geq \cdots \geq 0$. For eigenvalues and singular values it is valid that $\sigma_i = \sqrt{\Lambda_i}$ where Λ_i is i'th eigenvalue of the square matrix $H H^T$ if $m \leq n$ ($H^T H$ if $m \geq n$). If H is of rank r, the matrix has r non-zero singular values, that is, $\sigma_{r+1} = \cdots = \sigma_n = 0$. The matrices U and V can be written as

$$U = (u_1, \cdots, u_m), \qquad V = (v_1, \cdots, v_n) \ , \tag{2.64}$$

where vectors u_i and v_i represent columns of matrices U and V. Vectors u_i and v_i are the *left and right singular vectors* of H. The SVD of H can also be written

as

$$H = U_1 \Sigma_1 V_1^T = \sum_{i=1}^{r} \sigma_i u_i v_i^T \ , \tag{2.65}$$

where

$$U_1 = (u_1, \cdots, u_r), \quad \Sigma_1 = \mathrm{diag}(\sigma_1, \cdots, \sigma_r), \quad V_1 = (v_1, \cdots, v_r) \ . \tag{2.66}$$

Here the matrix H of rank r is decomposed into a sum of r matrices of rank one.

As seen before, four fundamental subspaces of matrix H are needed to be considered when the minimum norm least squares solution is explored: $\mathcal{N}(H), \mathcal{N}(H)^\perp, \mathcal{R}(H), \mathcal{R}(H)^\perp$. There are also well known relations between the subspaces

$$\mathcal{N}(H)^\perp = \mathcal{R}(H^T), \qquad \mathcal{R}(H)^\perp = \mathcal{N}(H^T) \ . \tag{2.67}$$

The SVD gives complete information about these subspaces associated with H. It can be verified that [10]

$$\begin{array}{ll} \mathcal{N}(H) = \mathrm{span}\{v_{r+1}, \cdots, v_n\} & \mathcal{R}(H) = \mathrm{span}\{u_{r+1}, \cdots, u_n\} \\ \mathcal{N}(H^T) = \mathrm{span}\{v_1, \cdots, v_r\} & \mathcal{R}(H^T) = \mathrm{span}\{u_1, \cdots, u_r\} \ , \end{array} \tag{2.68}$$

where $\mathrm{span}\{v_1, \cdots, v_r\}$ denotes the set of all linear combinations of $v_1, \cdots, v_r$. In the least square estimation the functional (residual) which has to be minimized if of form

$$F(\theta) = \frac{1}{2} \left\| z - H\,\theta \right\|_2^2 \ . \tag{2.69}$$

U and V are orthonormal matrices, that is, $U^T U = U\,U^T = I$, $V^T V = V\,V^T = I$, $\|U\|_2 = \left\|U^T\right\|_2 = 1$ and for the unitary matrices it is valid that $\|U^T A\|_2 = \|A\|_2$. Now the minimized functional can be written as [10]

$$\begin{aligned} \frac{1}{2} \left\| z - H\,\theta \right\|_2^2 &= \frac{1}{2} \left\| U^T (z - H\,V\,V^T \theta) \right\|_2^2 && (2.70) \\ &= \frac{1}{2} \left\| U^T z - U^T H\,V\,V^T \theta) \right\|_2^2 && (2.71) \\ &= \frac{1}{2} \left\| U^T z - U^T U \Sigma V^T\,V\,V^T \theta) \right\|_2^2 && (2.72) \\ &= \frac{1}{2} \left\| U^T z - \Sigma V^T \theta) \right\|_2 && (2.73) \\ &= \frac{1}{2} \left\| \begin{pmatrix} a_1 \\ a_2 \end{pmatrix} - \begin{pmatrix} \Sigma_r & 0 \\ 0 & 0 \end{pmatrix} \begin{pmatrix} b_1 \\ b_2 \end{pmatrix} \right\|_2^2 && (2.74) \\ &= \frac{1}{2} \left\| \begin{pmatrix} a_1 - \Sigma_r b_1 \\ a_2 \end{pmatrix} \right\|_2^2 \ , && (2.75) \end{aligned}$$

where

$$\begin{pmatrix} a_1 \\ a_2 \end{pmatrix} = U^T z \ , \quad \begin{pmatrix} b_1 \\ b_2 \end{pmatrix} = V^T \theta \ , \tag{2.76}$$

$\Sigma_r = \mathrm{diag}(\sigma_1, \cdots, \sigma_r)$, r is rank of H, $a_1 \in \mathbb{R}^r$, $a_2 \in \mathbb{R}^{m-(r+1)}$, $b_1 \in \mathbb{R}^r$ and $b_2 \in \mathbb{R}^{n-(r+1)}$. Thus, the residual norm will be minimized for arbitrary b_2 and $b_1 = \Sigma_r^{-1} a_1$.

Using the second equation in (2.76) it can be written that

$$\theta = V \begin{pmatrix} b_1 \\ b_2 \end{pmatrix} . \tag{2.77}$$

The choice $b_2 = 0$ minimizes the norm $\|\theta\|_2$, and therefore the minimum norm LS-solution θ_{MN} can be written in terms of the SVD [10]

$$\widehat{\theta}_{MN} = V \begin{pmatrix} \Sigma_r^{-1} a_1 \\ 0 \end{pmatrix} \tag{2.78}$$

$$= V \begin{pmatrix} \Sigma_r^{-1} & 0 \\ 0 & 0 \end{pmatrix} U^T z , \tag{2.79}$$

where $\Sigma_r^{-1} = \mathrm{diag}(\sigma_1^{-1}, \cdots, \sigma_r^{-1})$. Let us denote

$$V \begin{pmatrix} \Sigma_r^{-1} & 0 \\ 0 & 0 \end{pmatrix} U^T =: H^\dagger \in \mathbb{R}^{n \times m} . \tag{2.80}$$

$H^\dagger$ is called the *pseudoinverse of* H or *Moore-Penrose* inverse and the minimum norm least squares solution (2.79) is called *pseudoinverse solution*. If H has full column rank ($r = n$) then dimension of b_2 and there is a unique least squares solution for the set of equations. Thus pseudoinverse solution equals the LS-solution.

For nearly rank-deficient problems the smallest singular value σ_n or some of the smallest singular values are nearly zero, that is,

$$\frac{\sigma_n}{\sigma_1} \ll 1 . \tag{2.81}$$

When $\sigma_i \to 0$ then $1/\sigma_i \to \infty$ and furthermore $\widehat{\theta}_{MN} \to \infty$. One way to stabilize the solution is to treat very small singular values as zero. This is called as *regularization based on SVD* or truncated SVD-method [30]. Numerically, if singular values are less than square root of machine precision computer treats them as zero. Problems will arise when singular values decay gradually to zero. In this case it is impractical to say where is the limit after which the singular values can be treated as zero without loosing essential information. This is the case in ill-posed problems such as EIT.

2.3.2 Levenberg-Marquardt method

A weaknesses of the Gauss-Newton method is its behavior when the Jacobian matrix $J(x)$ is ill-posed, especially when singular values of $J(x)$ decay gradually to zero. Because the condition number of $J(x)^T J(x)$ is the square of $J(x)$ even small errors in observations causes a significant error in determining the search direction

p_k. In *Levenberg-Marquardt method* the line search strategy is replaced with *a trust region strategy*. In this method a convenient and often effective approximation for the Hessian matrix is used. The main idea is that the original ill-conditioned problem is modified such that the solution of the modified problem is near to the solution of the original problem but is less sensitive to errors in the data.

The idea of the trust region approach is to accept the minimum of the quadratic model only as long as the model adequately reflects the behavior of the actual minimized function. Usually, the decision as to whether the model is acceptable is based on the norm of the computed search direction [10]. In line search methods search direction is generated and then effort is focused on finding a suitable step length along this direction. Trust region methods define a region around the current iterate within which the quadratic model is assumed to be an adequate representation of the minimized function [75]. After that the step parameter in the trust region is chosen. In effect, the search direction and step length are chosen simultaneously. If the step is not acceptable, the size of the region is reduced and a new minimizer (step parameter) is found. If the region is too small, the algorithm misses an opportunity to find the direction along which it could move closer to the minimum of the objective function. If the region is too large, step parameter may lead too far from the minimum of the objective function. In this case the size of the region has to be reduced and the whole step has to be taken again. In practice, if the quadratic model predict accurately the behavior of the minimized function the size of the trust region is steadily increased to allow longer steps to be taken. The mathematical formulation of idea of the trust region methods to find search direction p is the the solution of the constrained quadratic minimization subproblem

$$\begin{aligned} \min_{p\in\mathbb{R}^n} & \left\{ \frac{1}{2} p^T A p + b^T p + \text{constant} \right\} \\ & \text{subject to} \quad \|p\|_2 \leq c \ , \end{aligned} \tag{2.82}$$

for some scalar c. It can be shown (see for example [75]) that the vector p^* is a global solution of the the trust-region problem (2.82) if and only if p^* is feasible and there is a scalar $\lambda \geq 0$ such that following conditions are satisfied:

$$(A + \lambda I)p^* = -b \tag{2.83}$$

$$\lambda(c - \|p^*\|_2) = 0 \tag{2.84}$$

$$(A + \lambda I) \quad \text{is positive semidefinite} \tag{2.85}$$

In case of nonlinear LS-problem (see Section 2.2) with the linearization $h(\theta) \approx h(\theta_0) + J(\theta_0)(\theta - \theta_0) = h(\theta_0) + J(\theta_0)p$ where $p = \theta - \theta_0$, the constrained minimization subproblem can be formulated as

$$\min_{p\in\mathbb{R}^n} \left\{ \frac{1}{2} \|z - h(\theta_0) + J(\theta_0)p\|_2^2 + \lambda \|p\|_2^2 \right\} \tag{2.86}$$

$$= \min_{p\in\mathbb{R}^n} \left\{ \frac{1}{2} \|r(\theta_0) + J(\theta_0)p\|_2^2 + \lambda \|p\|_2^2 \right\} \ , \tag{2.87}$$

where $r(\theta_0) = z - h(\theta_0)$. Minimization problem (2.87) can also be written as a least squares problem

$$\min_{p\in\mathbb{R}^n} \left\{ \frac{1}{2} \left\| \begin{bmatrix} J(\theta_0) \\ \sqrt{\lambda} I \end{bmatrix} p + \begin{bmatrix} r(\theta_0) \\ 0 \end{bmatrix} \right\|_2^2 \right\} \tag{2.88}$$

$$= \min_{p\in\mathbb{R}^n} \left\{ \frac{1}{2} \|J'p - r'\|_2^2 \right\} , \tag{2.89}$$

where

$$J' = \begin{bmatrix} J(\theta_0) \\ \sqrt{\lambda} I \end{bmatrix} \quad \text{and} \quad r' = - \begin{bmatrix} r(\theta_0) \\ 0 \end{bmatrix} . \tag{2.90}$$

It can be seen that

$$\frac{1}{2}\|J'p - r'\|_2^2 = \frac{1}{2}(J'p - r')^T(J'p - r') \tag{2.91}$$

$$= \frac{1}{2}\left((J'p)^T J'p - (J'p)^T r' - r'^T J'p + r'^T r'\right) \tag{2.92}$$

$$= \frac{1}{2} p^T J'^T J'p - r'^T J'p + \frac{1}{2} r'^T r' . \tag{2.93}$$

In the equation (2.93) the matrix $J'^T J'$ corresponds to the matrix A_k in the equation (2.82), the vector $-r'^T J'$ corresponds to the vector b^T and $\frac{1}{2} r'^T r'$ is constant with respect to the search direction p. Hence the LS-estimate for the search direction p is

$$\widehat{p}_{LS} = -(J'^T J')^{-1} J'^T r' \tag{2.94}$$

$$= \left(\begin{pmatrix} J(\theta_0)^T & \sqrt{\lambda} I \end{pmatrix} \begin{pmatrix} J(\theta_0) \\ \sqrt{\lambda} I \end{pmatrix} \right)^{-1} \begin{pmatrix} J(\theta_0) & \sqrt{\lambda} I \end{pmatrix} \begin{pmatrix} r(\theta_0) \\ 0 \end{pmatrix} \tag{2.95}$$

$$= \left(J(\theta_0)^T J(\theta_0) + \lambda I\right)^{-1} J(\theta_0)^T r(\theta_0) , \tag{2.96}$$

which is *the Levenberg-Marquardt direction*. The eigenvalues of the square matrix $J(\theta_0)^T J(\theta_0)$ are non-negative (matrix is positive semidefinite). Therefore the eigenvalues of the matrix $J(\theta_0)^T J(\theta_0) + \lambda I$ are positive for all $\lambda > 0$ (matrix is positive definite) which guarantees that the unique $\widehat{p}_{LS}$ (minimum) exists also when $J(\theta_0)$ is rank deficient. When the search direction is chosen again in every iteration step and the model $h(\theta)$ is linearized again in $\widehat{\theta}_k$ the iterative algorithm

$$\widehat{\theta}_{k+1} = \widehat{\theta}_k + \alpha_k \left(J(\theta_k)^T J(\theta_k) + \lambda_k I\right)^{-1} J(\theta_k)^T r(\theta_k) \tag{2.97}$$

is obtained. This is called *the Levenberg-Marquardt method*. As can be seen, if $\lambda_k = 0$ the direction is the same as the Gauss-Newton direction. Whereas if $\lambda_k \to \infty$, $J(\theta_0)^T J(\theta_0)$ will become negligible and the direction becomes parallel with the steepest-descent direction. Therefore, in order to ensure descent a "good" value of λ_k (or c) must be chosen in the trust region methods. Typically the scalar c is found by solving the search direction for trial values of c. The new iteration direction $\widehat{p}_{LS}$ is chosen such that the minimization subproblem gets smaller value

than in the previous iteration step. Convergence of the trust region methods can be slow for the large residual problems or very nonlinear problems. Many versions of the Levenberg-Marquardt method have been coded using various strategies to choose λ_k [45].

2.3.3 Tikhonov regularization

One of the most successful methods for solving ill-conditioned LS-problems is *Tikhonov regularization* [31]. In this method the solution space is restricted by imposing an a priori bound $\|I\,(\theta - \theta^*)\|_2$ where θ^* is initial (prior) guess for the solution and I is identity matrix.

LINEAR CASE

In linear case the constrained minimization problem is formulated as

$$\begin{aligned} &\min_{\theta\in\mathbb{R}^n} \left\{ \frac{1}{2}\|z - H\,\theta\|_2^2 \right\} \\ &\text{subject to} \quad \|I(\theta - \theta^*)\|_2^2 \le c\,, \end{aligned} \tag{2.98}$$

for some scalar c. As seen earlier, the problem (2.98) can also be formulated as

$$\min_{\theta\in\mathbb{R}^n} \frac{1}{2} \left\{ \|H\,\theta - z\|_2^2 + \lambda^2 \|I\,(\theta - \theta^*)\|_2^2 \right\}\,. \tag{2.99}$$

The parameter $\lambda \ge 0$ is called *the regularization parameter* and it controls the weight given to the side constraint $\|\,I\,(\theta - \theta^*)\|_2^2$.

The minimized functional in (2.99) can also be written in the form [52]

$$F(\theta) = \frac{1}{2} \left\| \begin{pmatrix} H \\ \lambda I \end{pmatrix} \theta - \begin{pmatrix} z \\ \lambda\theta^* \end{pmatrix} \right\|^2 \tag{2.100}$$

$$= \frac{1}{2}\|H'\,\theta - z'\|^2 \tag{2.101}$$

where

$$H' = \begin{pmatrix} H \\ \lambda I \end{pmatrix} \quad \text{and} \quad z' = \begin{pmatrix} z \\ \lambda\theta^* \end{pmatrix}\,, \quad \mathcal{N}(H') = \mathcal{N}(H'^T H') = \{0\} \ \text{ for all } \lambda > 0\,.$$

Now the LS estimate for the parameter θ is

$$\widehat{\theta}_{LS} = (H'^T H')^{-1} H'^T z \tag{2.102}$$

$$= \left((H^T \quad \lambda I) \begin{pmatrix} H \\ \lambda I \end{pmatrix} \right)^{-1} (H^T \quad \lambda I) \begin{pmatrix} z \\ \lambda\theta^* \end{pmatrix} \tag{2.103}$$

$$= (H^T H + \lambda^2 I)^{-1} (H^T z + \lambda^2 \theta^*)\,. \tag{2.104}$$

$\widehat{\theta}_{LS}$ is a regularized solution, called *the Tikhonov -approximation*, of the ill-posed problem

$$\min_{\theta\in\mathbb{R}^n} \frac{1}{2} \{ \|z - H\,\theta\|_2^2 \}\,. \tag{2.105}$$

As can be seen if λ is very small the problem is close to ill-posed problem and the Tikhonov -approximation will be unstable. If $\lambda \to \infty$ then $\widehat{\theta}_{LS} \to \theta^*$. Quite often the prior guess is chosen to be zero and in this case $\widehat{\theta}_{LS} \to 0$ when $\lambda \to \infty$.

NONLINEAR CASE

Many inverse problems are both ill-posed and nonlinear. Typically the linearization is used together with the regulation for solving nonlinear ill-posed problems.

In nonlinear case the minimized functional is of form

$$\min_{\theta \in \mathbb{R}^n} \frac{1}{2} \left\{ \|z - h(\theta)\|_2^2 + \lambda^2 \|I\,(\theta - \theta^*)\|_2^2 \right\} \ . \tag{2.106}$$

The linearization can be done in two different ways. In Gauss' method the nonlinear model $h(\theta)$ is linearized as in the equation (2.49) and the minimized functional can be written as

$$F(\theta) = \frac{1}{2} \left\{ \|(z' - J\theta)\|_2^2 + \lambda^2 \|I(\theta - \theta^*)\|_2^2 \right\} \tag{2.107}$$

where $z' = z - h(\theta_0) + J\theta_0$ and $J = J(\theta_0)$. The functional (2.107) can also be written as

$$\begin{aligned} F(\theta) &= \frac{1}{2} \left\| \begin{pmatrix} J \\ \lambda I \end{pmatrix} \theta - \begin{pmatrix} z' \\ \lambda \theta^* \end{pmatrix} \right\|_2^2 && (2.108) \\ &= \frac{1}{2} \|J'\,\theta - z''\|_2^2 && (2.109) \end{aligned}$$

where

$$J' = \begin{pmatrix} J \\ \lambda I \end{pmatrix} \quad \text{and} \quad z'' = \begin{pmatrix} z' \\ \lambda \theta^* \end{pmatrix} \ .$$

Now the LS-estimate of θ is

$$\begin{aligned} \widehat{\theta}_{LS} &= \left(J'^T J'\right)^{-1} J'^T z'' && (2.110) \\ &= \left(J^T J + \lambda^2 I\right)^{-1} \left(J^T z' + \lambda^2 \theta^*\right) && (2.111) \\ &= \left(J^T J + \lambda^2 I\right)^{-1} \left(J^T (z - h(\theta_0) + J\theta_0) + \lambda^2 \theta^*\right) && (2.112) \\ &= \left(J^T J + \lambda^2 I\right)^{-1} \left(J^T z - J^T h(\theta_0) + J^T J\theta_0 + \lambda^2 \theta^*\right) && (2.113) \end{aligned}$$

If the term $\lambda^2 \theta_0$ is added and subtracted in equation (2.113) then

$$\begin{aligned} \widehat{\theta}_{LS} &= (J^T J + \lambda^2 I)^{-1} \left(J^T z - J^T h(\theta_0) + J^T J\theta_0 + \lambda^2 \theta^* + \lambda^2 \theta_0 - \lambda^2 \theta_0\right) && (2.114) \\ &= (J^T J + \lambda^2 I)^{-1} \left(J^T (z - h(\theta_0)) + (J^T J + \lambda^2 I)\theta_0 - \lambda^2 (\theta_0 - \theta^*)\right) && (2.115) \\ &= \theta_0 + (J^T J + \lambda^2 I)^{-1} \left(J^T (z - h(\theta_0)) - \lambda^2 (\theta_0 - \theta^*)\right) \ . && (2.116) \end{aligned}$$

In the iterative form, the equation (2.116) can be written as

$$\widehat{\theta}_{k+1} = \widehat{\theta}_k + \alpha_k \left({J_k}^T J_k + \lambda^2 I\right)^{-1} \left({J_k}^T (z - h(\widehat{\theta}_k)) - \lambda^2 (\widehat{\theta}_k - \theta^*)\right) \ , \tag{2.117}$$

where $J_k = J(\theta_k)$. If the assumption $\theta^* = \widehat{\theta}_k$ is made the Levenberg-Marquardt method (2.97) is obtained. This implies that Levenberg-Marquardt algorithm minimizes only the functional $\|z - h(\theta)\|_2^2$ (ill-posed).

Another approach is to use Newton method (2.20). Accordingly the gradient and Hessian of the minimized functional (2.106) is needed. The gradient of the minimized functional (2.106) in θ_0 is

$$\begin{aligned}
\nabla F(\theta_0) &= \frac{1}{2}\frac{\partial}{\partial\theta}\left\{(z-h(\theta))^T(z-h(\theta)) + \lambda^2(\theta-\theta^*)^T(\theta-\theta^*)\right\}(\theta_0) && (2.118)\\
&= \frac{1}{2}\left\{2\left(\frac{\partial}{\partial\theta}(z-h(\theta)^T\right)(z-h(\theta))\right.\\
&\quad \left. + 2\lambda^2\left(\frac{\partial}{\partial\theta}(\theta-\theta^*)^T\right)(\theta-\theta^*)\right\} && (2.119)\\
&= -\left(\frac{\partial h}{\partial\theta}(\theta_0)\right)^T(z-h(\theta_0)) + \lambda^2(\theta_0-\theta^*) && (2.120)
\end{aligned}$$

and the second derivative is

$$\nabla^2 F(\theta_0) = -\left(\sum_{j=1}^{m}(z_j - h_j(\theta_0))G_j(\theta_0)\right) + \left(\frac{\partial h}{\partial\theta}(\theta_0)\right)^T\left(\frac{\partial h}{\partial\theta}(\theta_0)\right) + \lambda^2 I\,, \quad (2.121)$$

Where G_j is Hessian on h_j. Now the Newton-Raphson method takes the form

$$\begin{aligned}
\widehat{\theta}_{k+1} &= \widehat{\theta}_k + \alpha_k\left({J_k}^T J_k - \sum_{j=1}^{m}(z_j - h_j(\widehat{\theta}_k))G_j(\widehat{\theta}_k) + \lambda^2 I\right)^{-1}\\
&\qquad \cdot({J_k}^T(z - h(\widehat{\theta}_k)) - \lambda^2(\widehat{\theta}_k - \theta^*))\,. && (2.122)
\end{aligned}$$

When the approximation (see Section 2.2.1)

$$\sum_{j=1}^{m}(z_j - h_j(\widehat{\theta}_k))\left(\frac{\partial^2 h_j}{\partial\theta^2}(\widehat{\theta}_k)\right) \approx 0 \quad (2.123)$$

is used the iteration can be written in the form

$$\widehat{\theta}_{k+1} = \widehat{\theta}_k + \alpha_k\left({J_k}^T J_k + \lambda^2 I\right)^{-1}({J_k}^T(z - h(\widehat{\theta}_k)) - \lambda^2(\widehat{\theta}_k - \theta^*))\,. \quad (2.124)$$

as in equation (2.117).

2.3.4 Generalized Tikhonov regularization

If there is some prior information of the parameters θ or the errors v this information is worth to be utilized in order to get more accurate solution. Let us consider the non-linear functional to be minimized in the generalized form

$$F(\theta) = \frac{1}{2}\left\{\|L_1(z - h(\theta))\|^2 + \lambda^2\|L_2(\theta - \theta^*)\|^2\right\}. \quad (2.125)$$

Denote the matrices W_1 and W_2, such that $W_1 = L_1^T L_1$ and that $W_2 = L_2^T L_2$. Here the matrix W_1 is called the weighting matrix. For the Newton-Raphson method the first and the second derivatives are needed. The gradient is

$$\begin{aligned}
\nabla F(\theta_0) &= \frac{1}{2}\frac{\partial}{\partial\theta}\left\{(z-h(\theta))^T W_1(z-h(\theta)) + \lambda^2(\theta-\theta^*)^T W_2(\theta-\theta^*)\right\}(\theta_0) \\
&= \frac{1}{2}\frac{\partial}{\partial\theta}\left\{z^T W_1 z - z^T W_1 h(\theta) - (h(\theta))^T W_1 z + (h(\theta))^T W_1 h(\theta)\right\}(\theta_0) \\
&+ \frac{1}{2}\frac{\partial}{\partial\theta}\left\{\lambda^2(\theta^T W_2\theta - \theta^T W_2\theta^* - \theta^{*T} W_2\theta + \theta^{*T} W_2\theta^*)\right\}(\theta_0) \\
&= -\left(\frac{\partial h}{\partial\theta}(\theta_0)\right)^T W_1(z-h(\theta_0)) + \lambda^2 W_2(\theta_0-\theta^*) \qquad (2.126)
\end{aligned}$$

and the second derivative is

$$\begin{aligned}
\nabla^2 F(\theta_0) &= -\sum_{j=1}^{M}(L_1(j,:))(z-h(\theta_0))L_1 G_j(\theta_0) \\
&+ \left(\frac{\partial h}{\partial\theta}(\theta_0)\right)^T W_1\left(\frac{\partial h}{\partial\theta}(\theta_0)\right) + \lambda^2 W_2 \qquad (2.127)
\end{aligned}$$

where $L_1(j,:)$ denotes the j^{th} row of the matrix L_1. Now the Newton-Raphson method in the generalized form can be written as

$$\begin{aligned}
\widehat{\theta}_{k+1} = \widehat{\theta}_k + \alpha_k &\left(J_k{}^T W_1 J_k + \sum_{j=1}^{M}(L_1(j,:))(z-h(\widehat{\theta}_k))L_1 G_j(\widehat{\theta}_k) + \lambda^2 W_2\right)^{-1} \\
&\cdot(J_k{}^T W_1(z-h(\widehat{\theta}_k)) - \lambda^2 W_2(\widehat{\theta}_k-\theta^*)) \; . \qquad (2.128)
\end{aligned}$$

When the approximation $\nabla^2 F(\widehat{\theta}_k) \approx J_k{}^T W_1 J_k + \lambda^2 W_2$ is used the iteration can be written in the form

$$\begin{aligned}
\widehat{\theta}_{k+1} &= \widehat{\theta}_k + \alpha_k\left(J_k{}^T W_1 J_k + \lambda^2 W_2\right)^{-1} \\
&\cdot(J_k{}^T W_1(z-h(\widehat{\theta}_k)) - \lambda^2 W_2(\widehat{\theta}_k-\theta^*)) \; . \qquad (2.129)
\end{aligned}$$

The algorithm (2.129) is called Gauss-Newton algorithm in the generalized form. Typically the weighting matrix W_1 is chosen to be an identity matrix I. The statistical interpretation (see next section) of this choice is that all the components of the observation noise vector have equal variances and the noise components are mutually uncorrelated. If the noise components have unequal variances it can be take into account by setting $W_1 = \text{diag}(\sigma_1^{-2},\ldots,\sigma_{\text{M}}^{-2})$ where σ_k is the error in i'th observation. Hence the observations with smaller error have bigger weight to the solution. Furthermore, the correlations between the noise components can be taken into account by using nondiagonal weighting matrix.

The matrix L_2 is called the *regularization matrix*. It is typically either identity matrix or if it is known that the solution is smooth, L_2 is taken to be a discrete approximation to some derivative operator. When the regularization matrix

is chosen to be a difference matrix the prior bound $\|L_2(\theta - \theta^*)\|_2^2$ ensures that two consecutive parameters are not too far from each other. The regularization parameter λ governs the balance between a small residual and a smooth solution.

STATISTICAL INTERPRETATION

In the former it was assumed that the parameters and errors are non-random and therefore these methods are called *deterministic methods*. If the parameters and the observation noise are treated as random variables the observation model, the prior assumptions, and the estimates can be written in the form of probability distributions. Methods with type of approach are called as *probabilistic methods*. Let us consider the observation model $z = h(\theta) + v$, where θ and v are random parameters and the problem is to estimate the parameters θ. Because the model $h(\theta)$ and v are independent so the conditional probability density of the measurements z given θ can be written as

$$p(z|\theta) = p(h(\theta) + v|\theta) = \underbrace{p(h(\theta)|\theta)}_{=1}\, p(v|\theta) = p(v|\theta) \ . \tag{2.130}$$

The conditional density of θ given (measured) z is defined as

$$p(\theta|z) = \frac{p(z,\theta)}{p(z)} \ , \tag{2.131}$$

where $p(z,\theta)$ is the joint probability density of z and θ. It is also valid that

$$p(z|\theta) = \frac{p(z,\theta)}{p(\theta)} \ , \tag{2.132}$$

and thus it can be written that (Bayes' theorem)

$$p(\theta|z)\, p(z) = p(z|\theta)\, p(\theta) \tag{2.133}$$

and further

$$p(\theta|z) = \frac{p(z|\theta)\, p(\theta)}{p(z)} \ . \tag{2.134}$$

Thus $p(\theta|z)$ is proportional to $p(z|\theta)\, p(\theta)$, that is,

$$p(\theta|z) \propto p(z|\theta)\, p(\theta) \ . \tag{2.135}$$

The conditional density $p(\theta|z)$ is called *the posterior density* because it gives the probabilities for θ's *after* the measurements, in contrast to $p(\theta)$, *the prior density* which gives the probabilities for θ's *before* the measurements. The conditional density $p(z|\theta)$ is called *the density*.

Let us assume that the noise is Gaussian with expectation $E(v)$=0 and covariance matrix C_v, and the parameters θ are also Gaussian with expectation

$E(\theta) = \eta_\theta$ and covariance matrix C_θ.

$$p(z|\theta) = p(v|\theta) \quad \propto \quad \exp\left\{-\frac{1}{2}((v - E(v))^T C_v^{-1}(v - E(v))\right\} \tag{2.136}$$

$$= \quad \exp\left\{-\frac{1}{2}((z - h(\theta))^T C_v^{-1}(z - h(\theta))\right\} \tag{2.137}$$

and

$$p(\theta) = \propto \exp\left\{-\frac{1}{2}((\theta - \eta_\theta)^T C_\theta^{-1}(\theta - \eta_\theta)\right\} \tag{2.138}$$

where C_θ is the covariance matrix of parameters θ (correspondingly for v). Covariance matrix is defined as

$$C_\theta = E\left\{(\theta - \eta_\theta)(\theta - \eta_\theta)^T\right\} \tag{2.139}$$

$$= E\left\{\theta\,\theta^T - \theta\,\eta_\theta^T - \eta_\theta\,\theta^T + \eta_\theta\,\eta_\theta^T\right\} \tag{2.140}$$

$$= E\left\{\theta\,\theta^T\right\} - E\left\{\theta\right\}\,\eta_\theta^T - \eta_\theta\,E\left\{\theta\right\}^T + \eta_\theta\,\eta_\theta^T \tag{2.141}$$

$$= E\left\{\theta\,\theta^T\right\} - \eta_\theta\,\eta_\theta^T \tag{2.142}$$

The covariance matrix is thus of the form

$$C_\theta = \begin{pmatrix} E\left\{\theta_1^2\right\} - \eta_{\theta_1}^2 & \cdots & E\left\{\theta_1\theta_n\right\} - \eta_{\theta_1}\eta_{\theta_n} \\ \vdots & \ddots & \vdots \\ E\left\{\theta_n\theta_1\right\} - \eta_{\theta_n}\eta_{\theta_1} & \cdots & E\left\{\theta_n^2\right\} - \eta_{\theta_n}^2 \end{pmatrix} \tag{2.143}$$

$$= \begin{pmatrix} \sigma_{\theta_1}^2 & \cdots & \sigma_{\theta_1\theta_n} \\ \vdots & \ddots & \vdots \\ \sigma_{\theta_n\theta_1} & \cdots & \sigma_{\theta_n}^2 \end{pmatrix}, \tag{2.144}$$

where $\sigma_{\theta_k}^2$ is a variance of the parameter θ_k and $\sigma_{\theta_k\theta_j}$ is a covariance of parameters θ_k and θ_j. If parameters θ_k and θ_j are uncorrelated $\sigma_{\theta_k\theta_j} = 0$. The conditional density of θ given z now becomes

$$\begin{aligned} p(\theta|z) &\propto \exp\left\{-\tfrac{1}{2}((z - h(\theta))^T C_v^{-1}(z - h(\theta))\right\} \exp\left\{-\tfrac{1}{2}((\theta - \eta_\theta)^T C_\theta^{-1}(\theta - \eta_\theta)\right\} \\ &= \exp\left\{-\tfrac{1}{2}\left[(z - h(\theta))^T C_v^{-1}(z - h(\theta)) + (\theta - \eta_\theta)^T C_\theta^{-1}(\theta - \eta_\theta)\right]\right\} \end{aligned} \tag{2.145}$$

The maximum a posteriori estimate (MAP) is the vector θ that maximizes the posterior density (2.145). This is obtained by minimizing the functional

$$F(\theta) = \frac{1}{2}\left[(z - h(\theta))^T C_v^{-1}(z - h(\theta)) + (\theta - \eta_\theta)^T C_\theta^{-1}(\theta - \eta_\theta)\right]. \tag{2.146}$$

This is identical to the functional (2.125) in generalized Tikhonov regularization with choices $W_1 = C_v^{-1}$ and $\lambda^2 W_2 = C_\theta^{-1}$. As a consequence, increasing the parameter λ in Tikhonov regularization corresponds to decreasing C_θ, and the variances $\sigma_{\theta_k}^2$ which, loosely speaking, describe the uncertainty of the prior. Thus, increasing the regularization parameter λ can be interpreted as strengthening the prior.

2.4 Conjugate-gradient methods

The conjugate gradient method is an iterative method for solving a linear system of equations

$$Ax = b \ , \tag{2.147}$$

where A is $n \times n$ symmetric and positive definite matrix [75]. As can be seen the solution of the problem (2.147) $x = A^{-1}b$ ($n \times 1$ vector) is equal to the solution of the minimization problem

$$\phi(x) = \frac{1}{2}x^T Ax - b^T x + \text{constant} \tag{2.148}$$

whose minimum is at the stationary point.

$$\frac{\partial \phi(x)}{\partial x} = \nabla \phi(x) = Ax - b = 0 \tag{2.149}$$

from which x can be solved. The gradient of $\phi(x)$ equals the residual $r(x)$ of the linear system

$$\nabla \phi(x) = Ax - b = r(x) \tag{2.150}$$

2.4.1 Conjugate direction method

Let us interpret the conjugate direction method as a technique for minimization of convex quadratic function (2.148). Because the iteration is given in the form

$$x_{k+1} = x_k + \alpha_k p_k \tag{2.151}$$

the minimized function at $(k+1)$'th iteration step is of form

$$\begin{aligned} \phi(x_{k+1}) &= \frac{1}{2}(x_k + \alpha_k p_k)^T A(x_k + \alpha_k p_k) - b^T(x_k + \alpha_k p_k) && (2.152) \\ &= \frac{1}{2}x_k^T Ax_k + \alpha_k x_k^T Ap_k + \frac{1}{2}\alpha_k^2 p_k^T Ap_k - b^T x_k - \alpha_k b^T p_k && (2.153) \end{aligned}$$

Now the problem is to find α_k and p_k such that the quadratic function (2.153) will be minimized. Let us differentiate the function $\phi(x_{k+1})$ with respect to α_k

$$\begin{aligned} \frac{\partial \phi(\alpha_k)}{\partial \alpha_k} &= (Ax_k - b)^T p_k + \alpha_k p_k^T Ap_k && (2.154) \\ &= r(x_k)^T p_k + \alpha_k p_k^T Ap_k \ , && (2.155) \end{aligned}$$

where $r(x_k) = Ax_k - b$. The one-dimensional minimizer of the quadratic function $\phi(\cdot)$ along $x_k + \alpha_k p_k$ can therefore be given explicitly in the form

$$\alpha_k = -\frac{r_k^T p_k}{p_k^T Ap_k} \ . \tag{2.156}$$

A set of nonzero vectors $\{p_0, p_1, p_2, ..., p_{n-1}\}$ is said to be *conjugate* with respect to the symmetric positive definite matrix A if

$$p_i^T A p_j = 0 \ , \quad \forall i \neq j \ . \tag{2.157}$$

Set of conjugate vectors is also linearly independent. When one of the conjugate directions $\{p_0, p_1, p_2, ..., p_n\}$ is chosen to be the search direction in each iteration step, $\phi(\cdot)$ can be minimized in at most n steps [75]. This can be proved by writing n'th iteration with the aid of previous iteration steps as

$$\begin{aligned} x_1 &= x_0 + \alpha_0 p_0 && (2.158)\\ x_2 &= x_1 + \alpha_1 p_1 = x_0 + \alpha_0 p_0 + \alpha_1 p_1 && (2.159)\\ &\vdots \\ x_n &= x_{n-1} + \alpha_{n-1} p_{n-1} = x_0 + \alpha_0 p_0 + \alpha_1 p_1 + \cdots + \alpha_{n-1} p_{n-1} && (2.160) \end{aligned}$$

Let us multiply equation (2.160) by $p_k^T A$ $(0 \leq k \leq n-1)$

$$p_k^T A x_n = p_k^T A x_0 + \alpha_0 \underbrace{p_k^T A p_0}_{=0} + \cdots + \alpha_k p_k^T A p_k + \cdots \alpha_{n-1} \underbrace{p_k^T A p_{n-1}}_{=0} \ . \tag{2.161}$$

Now the step parameter α_k can be solved from the equation (2.161)

$$\alpha_k = -\frac{p_k^T A (x_0 - x_n)}{p_k^T A p_k} \tag{2.162}$$

If k'th iterate is multiplied by $p_k^T A$:

$$p_k^T A x_k = p_k^T A x_0 + \alpha_1 \underbrace{p_k^T A p_1}_{=0} \cdots + \alpha_{k-1} \underbrace{p_k^T A p_{k-1}}_{=0}, \tag{2.163}$$

it can be observed that $p_k^T A x_k = p_k^T A x_0$. As can be seen if the search directions are chosen to be the conjugate directions the step parameter in (2.162) will be the same as the step parameter (2.156) which is exactly the one-dimensional minimizer of the quadratic function $\phi(\cdot)$. When the search directions are chosen to be conjugate directions the method composed of equations (2.151) and (2.156) is called as *Conjugate direction method.*

From the equation (2.160) it can be seen that the solution of the minimization problem (2.148) can also be formulated as

$$x^* = x_0 + \text{span}\{p_0, p_1, \cdots, p_{n-1}\} \tag{2.164}$$

where $\text{span}\{p_0, p_1, \cdots, p_{n-1}\}$ denotes the set of all linear combinations of $p_0, p_1, \cdots, p_{n-1}$. If the matrix A is diagonal the conjugacy condition (2.157) can be obtained by choosing the search directions basis vectors of natural base $(\{e_0, e_1, ..., e_{k-1}\})$. In other words after k iterations, the quadratic function has been minimized on the subspace spanned by $\{e_0, e_1, ..., e_{n-1}\}$. Since the natural

basis vectors are orthonormal one of the components of the solution x^* is correctly determined in each iteration step whereas with conjugacy bases $\{p_0, p_1, ..., p_n\}$, all of the components are updated in each iteration steps.

If the matrix A is not diagonal it can be transformed to diagonal by defining a new variable

$$\widehat{x} = S^{-1}x \ , \tag{2.165}$$

where S is $n \times n$ matrix defined by

$$S = [p_0, p_1, ..., p_{n-1}] \ , \tag{2.166}$$

where $\{p_0, p_1, ..., p_{n-1}\}$ is the set of conjugate directions with respect to A. Now the quadratic equation (2.148) is of form

$$\widehat{\phi}(\widehat{x}) = \frac{1}{2}\widehat{x}^T(S^TAS)\widehat{x} - (S^Tb)^T\widehat{x} \ . \tag{2.167}$$

By the conjugacy condition (2.157) the matrix S^TAS is diagonal and therefore the minimum of $\widehat{\phi}$ can be found by using the natural basis. Because of the relation (2.165) each direction e_k in $\widehat{x}$-space corresponds to the direction p_k in x-space. Hence the conjugate direction method applied to $\widehat{\phi}$ with direction e_k is equivalent to the conjugate direction method applied to ϕ with direction p_k.

One important result which will be utilized when conjugate gradient method is considered is that the residual $r(x_k) =: r_k$ (gradient of the quadratic function) is orthogonal to all the previous search directions

$$\begin{aligned}
r_{k+1}^T p_j &= (Ax_{k+1} - b)^T p_j \ , \qquad j < k+1 && (2.168)\\
&= (A(x_j + \alpha_j p_j + \alpha_{j+1}p_{j+1} + \cdots + \alpha_k p_k) - b)^T p_j && (2.169)\\
&= (Ax_j - b)^T p_j + \alpha_j (Ap_j)^T p_j + \alpha_{j+1}(Ap_{j+1})^T p_j + \cdots && (2.170)\\
&+ \alpha_k (Ap_k)^T p_j && (2.171)\\
&= r_j^T p_j + \alpha_j p_j^T A p_j + \alpha_{j+1} \underbrace{p_{j+1}^T A p_j}_{=0} + \cdots + \alpha_k \underbrace{p_k^T A p_j}_{=0} && (2.172)\\
&= r_j^T p_j - \frac{r_j^T p_j}{p_j^T A p_j} p_j^T A p_j && (2.173)\\
&= 0 \ . && (2.174)
\end{aligned}$$

2.4.2 Conjugate gradient method

In previous section the conjugate direction methods were discussed. They were based on any choice of the conjugate direction set $\{p_0, p_1, ..., p_{n-1}\}$. For large-scale applications it is not practical to compute and/or store the complete set of direction vectors. In conjugate gradient method a new direction vector p_k can be computed by using previous vector p_{k-1} and therefore only one direction vector need to be stored. New direction is also conjugate to the previous search vectors [75].

In conjugate gradient method the steepest descent direction is chosen to be the first search direction and the next ones are chosen to be a linear combination of the steepest descent direction $-\nabla\phi(x_k) = -r_k$ and the previous search direction p_{k-1}

$$p_k = -r_k + \beta_k p_{k-1} \ . \tag{2.175}$$

The scalar β_k is to be determined by the requirement that p_{k-1} and p_k must be A conjugate such that $\beta_0 = 0$. Formulation for β_k can be obtained by multiplying equation (2.175) by $p_{k-1}^T A$

$$\underbrace{p_{k-1}^T A p_k}_{=0} = p_{k-1}^T A(-r_k + \beta_k p_{k-1}) \tag{2.176}$$

and furthermore

$$\beta_k = \frac{r_k^T A p_{k-1}}{p_{k-1}^T A p_{k-1}} \ . \tag{2.177}$$

Now the complete algorithm for solving the linear system by conjugate gradient method can be expressed as

Algorithm 1

Given x_0
Set $r_0 = Ax_0 - b$, $p_0 = -r_0$, $k = 0$
While $r_k \neq 0$ (or $r_k > \epsilon$)

$$\alpha_k = \frac{-r_k^T p_k}{p_k^T A p_k} \tag{2.178}$$

$$x_{k+1} = x_k + \alpha_k p_k \tag{2.179}$$

$$r_{k+1} = Ax_{k+1} - b \tag{2.180}$$

$$\beta_{k+1} = \frac{r_{k+1}^T A p_k}{p_k^T A p_k} \tag{2.181}$$

$$p_{k+1} = -r_{k+1} + \beta_{k+1} p_k \tag{2.182}$$

$$k = k + 1 \tag{2.183}$$

end

More economical form for the conjugate gradient method can be formulated by using the equation (2.182) and the fact that the residual is orthogonal to previous search directions. Let us multiply equation (2.182) by r_{k+1}^T

$$r_{k+1}^T p_{k+1} = -r_{k+1}^T r_{k+1} + \beta_{k+1} \underbrace{r_{k+1}^T p_k}_{=0} \tag{2.184}$$

$$= -r_{k+1}^T r_{k+1} \tag{2.185}$$

As can be seen from the equation (2.185) the step parameter α_k can also be formulated as

$$\alpha_k = \frac{r_k^T r_k}{p_k^T A p_k} \ . \tag{2.186}$$

From the equation (2.180) it can be obtained that $x_k = A^{-1}(r_k + b)$ and further $x_{k+1} = A^{-1}(r_{k+1} + b)$. When these are inserted into equation (2.179) iterative form for the residual can be formulated as

$$r_{k+1} = r_k + \alpha_k A p_k \tag{2.187}$$

and furthermore

$$r_{k+1} - r_k = \alpha_k A p_k \ . \tag{2.188}$$

From the result that the residual r_k is orthogonal to all previous search directions it can be obtained that r_k is also orthogonal to all the previous residuals r_j in conjugate gradient method:

$$r_{k+1}^T p_j = r_{k+1}^T(-r_j + \beta_j p_{j-1}) = 0, \qquad j < k+1 \tag{2.189}$$

thus

$$r_{k+1}^T r_j = \beta_j \underbrace{r_{k+1}^T p_{j-1}}_{=0} = 0. \tag{2.190}$$

Now β_k can be computed as

$$\beta_k = \frac{r_{k+1}^T A p_k}{p_k^T A p_k} \tag{2.191}$$

$$= \frac{r_{k+1}^T (r_{k+1} - r_k)}{p_k^T (r_{k+1} - r_k)} \tag{2.192}$$

$$= \frac{r_{k+1}^T r_{k+1} - \overbrace{r_{k+1}^T r_k}^{=0}}{\underbrace{p_k^T r_{k+1}}_{=0} - \underbrace{p_k^T r_k}_{=-r_k^T r_k}} \tag{2.193}$$

$$= \frac{r_{k+1}^T r_{k+1}}{r_k^T r_k} \tag{2.194}$$

and the algorithm takes the form

Algorithm 2

Given x_0
Set $r_0 = Ax_0 - b$, $p_0 = -r_0$, $k = 0$

While $r_k \neq 0$ (or $r_k > \epsilon$)

$$\alpha_k = \frac{r_k^T r_k}{p_k^T A p_k} \tag{2.195}$$

$$x_{k+1} = x_k + \alpha_k p_k \tag{2.196}$$

$$r_{k+1} = A x_{k+1} - b \tag{2.197}$$

$$\beta_{k+1} = \frac{r_{k+1}^T r_{k+1}}{r_k^T r_k} \tag{2.198}$$

$$p_{k+1} = -r_{k+1} + \beta_{k+1} p_k \tag{2.199}$$

$$k = k + 1 \tag{2.200}$$

end

Algorithm 2 is more economical than algorithm 1 because the matrix A is not needed for the computation of β_k.

Because the search directions are conjugates also the linear conjugate gradient method converges to x^* in at most n steps.

2.4.3 Nonlinear conjugate gradient method

When general nonlinear functions are considered only small modification to the Algorithm 2 is needed [75, 26]. Let us consider the case when the functional to be minimized is of form

$$\phi(x) = \frac{1}{2}\|b - A(x)\|_2^2 \, . \tag{2.201}$$

By using the linearization $A(x) \approx A(x_0) + J(x_0)(x - x_0)$ equation (2.201) can be formulated such that it corresponds with the quadratic function (2.148) which is minimized by linear conjugate gradient method as in section 2.3.2.

$$\phi(x) = \frac{1}{2}\|b' - Jx\|_2^2 \tag{2.202}$$

$$= \frac{1}{2}x^T J^T J x - (J^T b')^T x + \frac{1}{2} b'^T b' \, , \tag{2.203}$$

where $J = J(x_0)$ and $b' = b - A(x_0) + J(x_0)x_0$. Thus $J^T J$ corresponds to A, $J^T b'$ corresponds to b and $\frac{1}{2}b'^T b'$ is constant with respect to x. The step parameters α_k must be computed with an iterative process explained in the section 2.1.1 rather than in closed form . There are different methods to choose the scalar β_k in order to ensure that the search directions are close to the conjugate directions. In next two section two commonly used methods are discussed.

The Fletcher-Reeves method

Let us consider the case of minimizing a general functional $F(x)$. In the Fletcher-Reeves method the residual $r(x)$, which equals the gradient of quadratic function

$\phi(x)$ in linear case, is replaced by gradient of the nonlinear function $F(x)$

$$\beta_{k+1}^{FR} = \frac{\nabla F(x_{k+1})^T \nabla F(x_{k+1})}{\nabla F(x_k)^T \nabla F(x_k)} \tag{2.204}$$

and the algorithm takes the form

Algorithm 3

Given x_0
Evaluate $\nabla F(x_0)$
Set $p_0 = -\nabla F(x_0)$, $k = 0$
While $\nabla F(x_k) \neq 0$ (or $\nabla F(x_k) > \epsilon$)

$$\begin{aligned}
\text{Compute} \quad & \alpha_k \\
x_{k+1} &= x_k + \alpha_k p_k && (2.205) \\
\text{Evaluate} \quad & \nabla F(x_{k+1}) \\
\beta_{k+1}^{FR} &= \frac{\nabla F(x_{k+1})^T \nabla F(x_{k+1})}{\nabla F(x_k)^T \nabla F(x_k)} && (2.206) \\
p_{k+1} &= -\nabla F(x_{k+1}) + \beta_{k+1}^{FR} p_k && (2.207) \\
k &= k + 1 && (2.208)
\end{aligned}$$

end

If minimization problem was quadratic and α_k was the exact minimizer this algorithm would be equal to the linear conjugate gradient method. When inexact minimizer is used α_k has to be chosen such that the search direction is a descent direction.

Polak-Ribière Method

In Polak-Ribière method β_k is computed as

$$\beta_{k+1}^{PR} = \frac{\nabla F(x_{k+1})^T \left(\nabla F(x_{k+1}) - \nabla F(x_k)\right)}{\nabla F(x_k)^T \nabla F(x_k)} \,. \tag{2.209}$$

If α_k is the exact minimizer, the equation (2.209) equals the equation (2.206) since the gradients are mutually orthogonal.

As explained in the section 2.1.2, if the search direction p_{k+1} is a descent direction then $\nabla F(x_{k+1})^T p_{k+1} < 0$. Hence from (2.207)

$$\nabla F(x_{k+1})^T p_{k+1} = -\nabla F(x_{k+1})^T \nabla F(x_{k+1}) + \beta_{k+1}^{PR} \nabla F(x_{k+1})^T p_k < 0 \,. \tag{2.210}$$

If β_{k+1}^{PR} is negative and p_k is a descent direction the term $\beta_{k+1}^{PR} \nabla F(x_{k+1})^T p_k$ is positive and may be larger than $\nabla F(x_{k+1})^T \nabla F(x_{k+1}) = \|\nabla F(x_{k+1})\|_2^2$ in which case $\nabla F(x_{k+1})^T p_{k+1} > 0$ and the direction p_{k+1} is not a descent direction. In

order to assure that a new direction is descent the condition that only positive β_{k+1}^{PR} are accepted a condition

$$\beta_{k+1}^{PR} = \max\{\beta_{k+1}^{PR}, 0\} \tag{2.211}$$

has to be included in Polak-Ribière method. The condition (2.211) means that when β_{k+1}^{PR} is negative a new search direction is chosen to be the steepest descent direction $-\nabla F(x_{k+1})$. If β_{k+1}^{PR} is positive the new search direction will be a sum of two descent directions and therefore descent as well.

When the angle between $\nabla F(x_{k+1})$ and $\nabla F(x_k)$ is less than $\pi/2$ then $\beta_{k+1}^{PR} < \beta_{k+1}^{FR}$ which means that in Polak-Ribière method the new search direction is closer to steepest descent direction than in Fletcher-Reeves method. When the angle is more than $\pi/2$ then $\beta_{k+1}^{PR} > \beta k + 1^{FR}$, which means that in Polak-Ribière method the new search direction is closer to previous search direction than in Fletcher-Reeves method.

Comparison between Fletcher-Reeves and Polak-Ribière methods

When search direction p_k is very poor, which means that p_k is almost orthogonal to the steepest descent direction $(\nabla F(x_k)^T p_k \approx 0)$, it is obvious that the step parameter will be very small. Furthermore, x_{k+1} will be approximately same as x_k and $\nabla F(x_{k+1}) \approx \nabla F(x_k)$, and therefore

$$\beta_{k+1}^{FR} \approx 1 \tag{2.212}$$

and

$$p_{k+1} \approx -\nabla F(x_k) + p_k \ . \tag{2.213}$$

Numerical experience indicates that Polak-Ribière method is more robust and efficient than Fletcher-Reeves method [75].

There are many other choices for β_k that coincide with Fletcher-Reeves formula β_k^{FR} in the case where the objective function is quadratic and the line search is exact but these methods have not been found to be more efficient than Polak-Ribière method [75]. However, in every method choosing of step parameter α_k has a significant effect on convergence rate of nonlinear conjugate gradient method.

Restarting

In nonlinear conjugate gradient method quadratic assumptions have been used. If minimized function is not quadratic the method may generate a poor search direction. A typical requirement for good search direction is that p_{k+1} should be sufficiently downhill. There are numerous strategies for investigating if search direction is good. A common strategy is based on observation that the gradients are mutually orthogonal for the quadratic functions which means that

$$\cos\theta = \frac{\nabla F(x_{k+1})^T \nabla F(x_k)}{\|\nabla F(x_{k+1})\|_2 \|\nabla F(x_k)\|_2} = 0 \tag{2.214}$$

where θ is the angle between $\nabla F(x_{k+1})$ and $\nabla F(x_k)$. If gradients are far from orthogonal which means that

$$\cos\theta \geq \gamma \tag{2.215}$$

(typical value for the parameter γ is 0.1) a restart is performed, that is, a new search direction is chosen to be the steepest descent direction. Also other choices for restarting can be made [75].

CHAPTER III

Forward problem in EIT

In EIT, weak alternating currents are injected into the object through the electrodes which are attached on the boundary of the object. The resulting voltages can be measured with the same electrodes. An estimate for the internal resistivity distribution of the object is obtained by using these voltage measurements. In order to estimate the resistivity distribution, that is, to solve the inverse problem of EIT, the forward problem of EIT has to be solved. The forward problem of EIT is to compute the boundary voltages when the resistivity distribution and the injected currents are known. Several different mathematical models for the forward problem have been developed. The most accurate model is called the complete electrode model. In this thesis the complete electrode model is used as the forward model, and in order to approximate the solution of the associated mixed boundary value problem the finite element method is used.

In this section the complete electrode model, and its variational form are discussed. Also the FEM discretization, the integration over the elements with mapping method and infinite elements in 3D EIT are discussed.

3.1 The complete electrode model

The complete electrode model is the most accurate model for the EIT since it takes into account the effects of the electrodes and the contact impedances between the object and the electrodes [17, 91]. With the complete electrode model the measured potentials can be predicted at the precision of the measurement system [91].

Electromagnetic field inside the object can be modelled by Maxwell equations

$$\nabla \cdot D = \rho_c \tag{3.1}$$

$$\nabla \cdot B = 0 \tag{3.2}$$

$$\nabla \times E = -\frac{\partial B}{\partial t} \tag{3.3}$$

$$\nabla \times H = J + \frac{\partial D}{\partial t}. \tag{3.4}$$

where $\nabla\times$ is the curl operator, $\nabla\cdot$ is the divergence operator, $\frac{\partial}{\partial t}$ partial derivative with respect to time, E electric field, H magnetic field, B magnetic induction, D electric displacement. The charge density has been denoted by ρ_c and the current density by J, $J = J^s + J^o$ = source current + ohmic current. Further, in linear isotropic medium

$$D = \varepsilon E \tag{3.5}$$
$$B = \mu H \tag{3.6}$$
$$J = \sigma E\ , \tag{3.7}$$

are also valid. Here ε is permittivity and μ permeability of the medium. The conductivity σ is the inverse of the resistivity ρ.

In EIT, the so-called quasi-static approximation is usually made. That is, although the alternating currents are used, the time-dependence is neglected. The quasi-static approximation is adequate in the cases in which the frequencies of the alternating currents are small enough, see for example [100].

With the quasi-static approximation the time derivatives in equations (3.3) and (3.4) are zero. Further, the current source J^s is assumed to be zero inside the object. Because $\nabla \times E = 0$ there is an electric potential u such that

$$E = -\nabla u\ . \tag{3.8}$$

Since

$$\nabla \cdot J = \nabla \cdot (\nabla \times H) = 0\ ,$$

from the equation (3.7)

$$\nabla \cdot \sigma E = 0\ , \tag{3.9}$$

and thus, by using equation (3.8)

$$\nabla \cdot \sigma \nabla u = 0\ . \tag{3.10}$$

The equation (3.10) is the model corresponding to the interior of the object. In the following section the boundary conditions are derived.

3.1.1 Boundary conditions

The current source J^s on the boundary of the object $\partial\Omega$ is not zero in EIT. On the boundary the equation (3.9) gets the form

$$\nabla \cdot \sigma E = \nabla \cdot J^s. \tag{3.11}$$

Consider a situation shown in Fig. 3.1. A small volume element is placed on the surface of an object so that the top and the bottom of the domain are parallel with the boundary [101]. Assume that the current density J^s injected into the object is a continuous function. Integrating the equation (3.11) over the volume τ

$$\int_\tau \nabla \cdot \sigma E\ d\tau = \int_\tau \nabla \cdot J^s\ d\tau \tag{3.12}$$

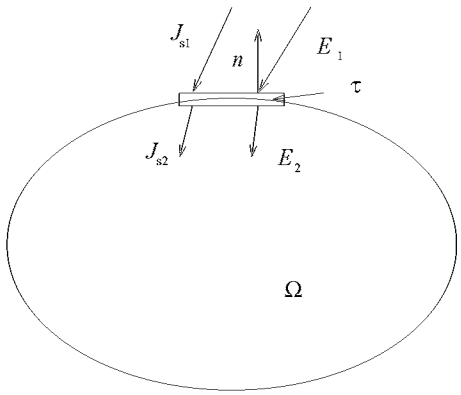

Figure 3.1: Derivation of the Neumann boundary condition. The electric field is zero outside the object and thus $E = E_2$. Further, the source current density J^s inside the object is zero, and thus $J^s = J_{s1}$ [101].

and by using the Gauss theorem the form

$$\int_S \sigma E \cdot n \ dS = -\int_S J^s \cdot n \ dS \tag{3.13}$$

is obtained. Here S is the boundary of τ and n is the outward unit normal. When the volume $\tau \longrightarrow 0$ the top and the bottom of the cylinder coincide. Since $J^s = 0$ inside the object and on the other hand $E = 0$ outside the object, the equation (3.13) gets the form

$$-\sigma E \cdot n|_{\text{inside}} = -J^s \cdot n|_{\text{outside}} \ , \tag{3.14}$$

Furthermore, by using equation (3.8), the boundary condition (Neumann)

$$\sigma \frac{\partial u}{\partial n} = -J^s \cdot n \equiv j \tag{3.15}$$

is obtained, where j is the negative normal component of the injected current density J^s. The equation (3.10) together with the equation (3.15) is called *the continuum model*

In the real case, however, the current density j under the electrodes is not known. However, the total current $I_\ell = \int_{e_\ell} j \ dS$ is known. For this reason the Neumann condition (3.15) is rewritten in the form

$$\int_{e_\ell} \sigma \frac{\partial u}{\partial n} \ dS = I_\ell \ , \qquad \ell = 1, 2, ..., L \tag{3.16}$$

where e_ℓ is the surface of the ℓ'th electrode, I_ℓ is injected current into the ℓ'th electrode and $\partial\Omega$ the boundary of the object. Furthermore, on the boundary

between the electrodes the current density $j = 0$, and thus

$$\sigma \frac{\partial u}{\partial n} = 0 \ , \qquad x \in \partial\Omega \backslash \bigcup_{\ell=1}^{L} e_\ell \tag{3.17}$$

Moreover, the shunting effect on the electrodes can be taken into account by considering the following condition

$$u = U_\ell, \quad \ell = 1, 2, ..., L, \quad x \in e_\ell \tag{3.18}$$

where U_ℓ is the voltage on the ℓ'th electrode. The equation (3.10) together with the equations (3.16)-(3.18) is called *the shunt model*.

If both the shunting effect of the electrodes and the contact impedance between the electrodes and tissue are taken into account *the complete electrode model* is obtained. In that case the equation (3.18) is replaced by equation

$$u + z_\ell \sigma \frac{\partial u}{\partial n} = U_\ell, \quad \ell = 1, 2, ..., L, \quad x \in e_\ell \tag{3.19}$$

where z_ℓ is the effective contact impedance between the ℓ'th electrode and object.

Thus, the complete electrode model consists of the following equations

$$\nabla \cdot (\sigma \nabla u) = 0 \ , \qquad x \in \Omega \tag{3.20}$$

$$u + z_\ell \sigma \frac{\partial u}{\partial n} = U_\ell \ , \qquad x \in e_\ell, \ \ell = 1, 2, ..., L \tag{3.21}$$

$$\int_{e_\ell} \sigma \frac{\partial u}{\partial n} \, dS = I_\ell \ , \qquad x \in e_\ell, \ \ell = 1, 2, ..., L \tag{3.22}$$

$$\sigma \frac{\partial u}{\partial n} = 0 \ , \qquad x \in \partial\Omega \backslash \bigcup_{\ell=1}^{L} e_\ell \tag{3.23}$$

In addition, the charge conservation law

$$\sum_{\ell=1}^{L} I_\ell = 0 \tag{3.24}$$

must be fulfilled. Furthermore, in order to find a unique solution for the forward problem, the reference point for the potential has to be fixed. This can be done for example by setting

$$\sum_{\ell=1}^{L} U_\ell = 0 \ . \tag{3.25}$$

The existence and uniqueness of the solution for the complete electrode model has been proven in [91].

3.2 Finite element method in EIT

Finite element method (FEM) is traditionally used to solve problems in structure analysis. However, it can be used to solve numerically most of the problems which can be described as differential equations, partial differential equations, integral equations or variational equations in general. As the name, finite element method, indicates that the region of interest is divided into a finite number of regions or *elements*. The elements can be segments of the line in one dimension (1D), triangles or quadrilaterals in two dimensions (2D), and tetrahedron, hexahedron or wedges in three dimensions (3D). An element is composed of nodes and one or more faces of the element.

Before using numerical methods, such as FEM, one should be guaranteed that a unique solution exists, that is, the problem has to be mathematically sound [29]. Advantages of FEM are that dimension, time dependence or nonlinearity do not necessarily limit the method. The physical qualities such as density or resistivity can vary inside the object. They can also depend on the solution of another mathematical model. Also the convergence analysis of FEM is rigorous [12] and different boundary conditions (Dirichlet, Neumann, Newton) can be used.

In comparison with other methods, for example finite difference method, the biggest advantage of FEM is that complicated geometries can be used. Furthermore, the unknown functions can be approximated inside each element by linear or higher order polynomials. In finite difference method, the unknown functions are approximated only in the nodes, so a denser mesh is needed in order to obtain the same accuracy as in FEM. In addition, the implementation of complex boundary conditions may be difficult when using finite difference methods.

In order to use FEM for the numerical solution of differential equations, partial differential equations or integral equations one first needs to write down the so-called variational form (weak form) for the equation. The variational form is an alternative way to formulate the original equation and the associated boundary conditions. For the variational equation the residual of the original differential equation (or partial differential equation or integral equation) is formed. The residual is multiplied by a test function $v(x)$ and integrated over the domain Ω. Test functions v belong to some Sobolev space (in EIT $v(x) \in H^1(\Omega)$). In FEM, the next step is to find a finite dimensional approximation for the solution of the variational problem. The solution $u(x)$ of the partial differential equation is thus approximated by the finite sum

$$u(x) \approx \sum_{i=1}^{K} u_i \varphi_i(x) \tag{3.26}$$

where $\varphi_i(x), i = 1, ..., K$ are the basis functions which form the basis of the discrete solution space, and K is the number of the nodes. In *Galerkin FEM approximation* the test functions v are also chosen to be the basis functions φ_i. When the approximation (3.26) is inserted into the variational problem, a system of linear equations is obtained which can be written in the matrix form. This will be discussed later when finite element method in EIT is considered.

Depending on the partial differential equations and their boundary conditions the basis functions can be chosen to be whatever linearly independent functions from the discrete solution space. However, the basis functions in FEM are usually chosen such that the requirements between the basis functions φ_i and the nodes (x_j)

$$\varphi_i(x_j) = \begin{cases} 1, & i = j \\ 0, & \text{otherwise} \end{cases} \tag{3.27}$$

are fulfilled. In that case the system of equations is faster to solve since most of the integrals in the variational form will be zero. Note also that with this choice the parameters u_i in equation (3.26) are the values of the solution in i'th node. With certain partial differential equations (2nd order) the basis functions can be chosen to be piecewise linear or piecewise higher order polynomials.

3.2.1 Variational form for the complete electrode model

For the FEM solution of the complete electrode model the variational equation is needed. In this section the variational form for the complete electrode model is derived formally. For more rigorous proof for the variational formulation, see for example [91] or [103].

Let us consider the complete electrode model as a group of connected partial differential equations. The object which is studied separates into two parts, boundary of the domain $\partial\Omega$ and domain Ω. Let us denote that test functions $v \in H^1(\Omega)$ (for the potential u) and $V \in \mathbb{R}^L$ ($V = (V_1, \ldots, V_L)$) (for the voltages U_ℓ on the electrodes) such that the condition $\sum_{\ell=1}^{L} V_\ell = 0$ is fulfilled and let $H = H^1(\Omega) \times \mathbb{R}^L$. By multiplying equation (3.20) by test functions v and by integrating over the domain Ω

$$\int_\Omega v\nabla \cdot (\sigma \nabla u)\, dx = 0 \tag{3.28}$$

is obtained. From Green's formula (if $\partial\Omega$ is smooth enough)

$$\int_\Omega v\nabla \cdot (\sigma \nabla u)\, dx = \int_{\partial\Omega} \sigma \frac{\partial u}{\partial n} v\, dS - \int_\Omega \sigma \nabla u \cdot \nabla v\, dx = 0\ , \tag{3.29}$$

is obtained for all $u, v \in H^1(\Omega)$ when $\nabla \cdot (\sigma \nabla u) \in L^2(\Omega)$. Here $L^2(\Omega)$ is a set of Lebesque square integrable functions. The boundary of the domain can be separated into two parts, domain under the electrodes e_ℓ and domain between the electrodes $\partial\Omega \backslash \bigcup_{\ell=1}^{L} e_\ell$, and thus from (3.29) it can be written that

$$\underbrace{\int_{\partial\Omega \backslash \bigcup_{\ell=1}^{L} e_\ell} \sigma \frac{\partial u}{\partial n} v\, dS}_{=0} + \sum_{\ell=1}^{L} \int_{e_\ell} \sigma \frac{\partial u}{\partial n} v\, dS - \int_\Omega \sigma \nabla u \cdot \nabla v\, dx = 0\ . \tag{3.30}$$

The first integral is because of the equation (3.23). Furthermore, the equation (3.21) implies

$$\sigma \frac{\partial u}{\partial n} = -\frac{u - U_\ell}{z_\ell}\ , \tag{3.31}$$

where the contact impedance z_ℓ is constant under the electrode. Now the equation (3.30) can be written in the form

$$\sum_{\ell=1}^{L} \frac{1}{z_\ell} \int_{e_\ell} (u - U_\ell) v \, dS + \int_\Omega \sigma \nabla u \cdot \nabla v \, dx = 0 \; . \tag{3.32}$$

Next, let us multiply the equation (3.21) by the test function V_ℓ and integrate the product over the electrode e_ℓ.

$$\int_{e_\ell} (u + z_\ell \sigma \frac{\partial u}{\partial n}) V_\ell \, dS = \int_{e_\ell} U_\ell \, V_\ell \, dS \; , \qquad \ell = 1, 2, ..., L \; , \tag{3.33}$$

which is equivalent with the equation (V_ℓ is constant under the electrode)

$$\int_{e_\ell} (u - U_\ell) V_\ell \, dS + z_\ell V_\ell \underbrace{\int_{e_\ell} \sigma \frac{\partial u}{\partial n} \, dS}_{= I_\ell} = 0 \; , \qquad \ell = 1, 2, ..., L \; . \tag{3.34}$$

The second integral in the equation (3.34) is equal with the injected current I_ℓ according to the equation (3.22). Let us divide the equation (3.34) by z_ℓ

$$\frac{1}{z_\ell} \int_{e_\ell} (u - U_\ell) V_\ell \, dS + V_\ell I_\ell = 0 \; , \qquad \ell = 1, 2, ..., L \; , \tag{3.35}$$

which is equivalent with the equation

$$\sum_{\ell=1}^{L} \frac{1}{z_\ell} \int_{e_\ell} (u - U_\ell) V_\ell \, dS + \sum_{\ell=1}^{L} V_\ell I_\ell = 0 \; . \tag{3.36}$$

Combining the equations (3.32) and (3.36)

$$\begin{aligned} &\textstyle\sum_{\ell=1}^{L} \frac{1}{z_\ell} \int_{e_\ell} (u - U_\ell) v \, dS + \int_\Omega \sigma \nabla u \cdot \nabla v \, dx \\ &= \textstyle\sum_{\ell=1}^{L} \frac{1}{z_\ell} \int_{e_\ell} (u - U_\ell) V_\ell \, dS + \sum_{\ell=1}^{L} V_\ell I_\ell \; , \end{aligned} \tag{3.37}$$

which is equal with the equation

$$\sum_{\ell=1}^{L} \frac{1}{z_\ell} \int_{e_\ell} (u - U_\ell)(v - V_\ell) \, dS + \int_\Omega \sigma \nabla u \cdot \nabla v \, dx = \sum_{\ell=1}^{L} V_\ell I_\ell \; . \tag{3.38}$$

The left hand side in the equation (3.38)

$$\mathcal{B}((u, U), (v, V)) = \int_\Omega \sigma \nabla u \cdot \nabla v \, dx + \sum_{\ell=1}^{L} \frac{1}{z_\ell} \int_{e_\ell} (u - U_\ell)(v - V_\ell) \, dS \tag{3.39}$$

is so called bilinear form $\mathcal{B} : H \times H \to \mathbb{R}$. Hence the variational equation for the complete electrode model is of form

$$\mathcal{B}((u, U), (v, V)) = \sum_{\ell=1}^{L} I_\ell V_\ell \; , \quad \forall (v, V) \in H \; . \tag{3.40}$$

3.2.2 FEM approximation of the complete electrode model

The finite element method is used to turn the variational (infinite dimensional) equation given above into a finite dimensional formulation. First, the domain Ω is discretized into small elements (tetrahedron in our case). Next, the finite dimensional approximations are written for the unknown functions. The potential distribution within the object is approximated with the finite sum

$$u^h(x) = \sum_{i=1}^{\mathcal{N}} \alpha_i \phi_i(x) \tag{3.41}$$

and the potentials on the electrodes as

$$U^h = \sum_{j=1}^{L-1} \beta_j n_j, \tag{3.42}$$

where the functions ϕ_i form a basis for the finite dimensional subspace H^h of $H^1(\Omega)$ and the basis functions n_j are chosen, for example, so that $n_1 = (1, -1, 0, ..., 0)^T$, $n_2 = (1, 0, -1, 0, ..., 0)^T \in \mathbb{R}^{L\times 1}$ etc. This choice for n_j ensures that the condition (3.25) is fulfilled. In (3.41) $\mathcal{N}$ is the number of nodes in the finite element mesh and the coefficients α_i and β_j are to be determined. Inserting these two approximative functions into the variational equation (3.40) and by choosing $v = \phi_i$ and $V = n_j$, when the set of test functions is of form $Q = [(\phi_1, 0), \ldots, (\phi_{\mathcal{N}}, 0), (0, n_1), \ldots, (0, n_{L-1})]$, results in a system of linear equations which can be written in the matrix form as [12]

$$A\theta = f \tag{3.43}$$

where $\theta = (\alpha, \beta)^T$, if $\alpha = (\alpha_1, \alpha_2, ..., \alpha_{\mathcal{N}})$ and $\beta = (\beta_1, \beta_2, ..., \beta_{L-1})$. Thus the approximation for the potentials u^h and U^h are obtained by solving (3.43)

$$\theta = A^{-1} f \ . \tag{3.44}$$

In equation (3.43) $f = (\mathbf{0}, \widehat{I})^T$, where $\mathbf{0} \in \mathbb{R}^{1\times\mathcal{N}}$ and $\widehat{I} = (I_1 - I_2, I_1 - I_3, ..., I_1 - I_L)$. The matrix A is of the form

$$A = \begin{pmatrix} B & C \\ C^T & D \end{pmatrix} , \tag{3.45}$$

where

$$B(i,j) = \mathcal{B}((\phi_i,0),(\phi_j,0)) = \int_\Omega \sigma \nabla\phi_i \cdot \nabla\phi_j \, dx\, dy\, dz + \sum_{\ell=1}^{L} \frac{1}{z_\ell} \int_{e_\ell} \phi_i \phi_j \, dS \,, \quad i,j = 1,2,...,\mathcal{N} \tag{3.46}$$

$$C(i,j) = \mathcal{B}((\phi_i,0),(0,n_j)) = -\left(\frac{1}{z_1} \int_{e_1} \phi_i \, dS - \frac{1}{z_{j+1}} \int_{e_{j+1}} \phi_i \, dS \right) \,, \quad i = 1,2,...,\mathcal{N}, \quad j = 1,2,...,L-1 \tag{3.47}$$

$$D(i,j) = \mathcal{B}((0,n_i),(0,n_j)) = \sum_{\ell=1}^{L} \frac{1}{z_\ell} \int_{e_\ell} (n_i)_\ell (n_j)_\ell \, dS = \begin{cases} \frac{|e_1|}{z_1} \,, & i \neq j \\ \frac{|e_1|}{z_1} + \frac{|e_{j+1}|}{z_{j+1}} \,, & i = j \end{cases} \quad i,j = 1,\ldots,L-1 \tag{3.48}$$

where $|e_j|$ is the measure (area) of the electrode j. The potentials U_ℓ^h ($\ell = 1, \cdots, L$, L is the number of the electrodes) on the electrodes can be written according equation (3.42) as

$$\begin{aligned} U^h &= \begin{bmatrix} U_1^h & U_2^h & U_2^h & \cdots & U_L^h \end{bmatrix}^T = \sum_{j=1}^{L-1} \beta_j n_j, \\ &= \begin{pmatrix} \beta_1 \\ -\beta_1 \\ 0 \\ 0 \\ 0 \\ 0 \\ \vdots \end{pmatrix} + \begin{pmatrix} \beta_2 \\ 0 \\ -\beta_2 \\ 0 \\ 0 \\ 0 \\ \vdots \end{pmatrix} + \begin{pmatrix} \beta_3 \\ 0 \\ 0 \\ -\beta_3 \\ 0 \\ 0 \\ \vdots \end{pmatrix} + \cdots + \begin{pmatrix} \beta_{L-1} \\ 0 \\ 0 \\ 0 \\ \vdots \\ 0 \\ -\beta_{L-1} \end{pmatrix} \\ &= \begin{pmatrix} \sum_{\ell=1}^{L-1} \beta_\ell \\ -\beta_1 \\ -\beta_2 \\ -\beta_3 \\ -\beta_4 \\ \vdots \\ -\beta_{L-1} \end{pmatrix} \end{aligned} \tag{3.49}$$

This can be written in the matrix form

$$U^h = \mathcal{C}\beta^T \,, \tag{3.50}$$

where $\mathcal{C} \in \mathbb{R}^{L\times(L-1)}$ is a sparse matrix such that

$$\mathcal{C} = \begin{pmatrix} 1 & 1 & 1 & \cdots & 1 \\ -1 & 0 & 0 & \cdots & 0 \\ 0 & -1 & 0 & \cdots & 0 \\ 0 & 0 & -1 & \cdots & 0 \\ \vdots & \vdots & \vdots & \ddots & \vdots \\ 0 & 0 & 0 & 0 & -1 \end{pmatrix} \tag{3.51}$$

and $\beta = (\beta_1, \beta_2, \cdots, \beta_{L-1})$. Let us return to the solution (3.44) giving approximations for both the internal potential distribution and the electrode potentials. In equation (3.44) the relation between injected currents and the electrode potentials is thus of the form

$$U^h = \mathcal{C}\beta^T = \mathcal{C}\tilde{R}(\rho)\widehat{I} = \mathcal{C}\tilde{R}(\rho)\mathcal{C}^T I = R(\rho)I \ , \tag{3.52}$$

where $\tilde{R}(\rho) \in \mathbb{R}^{(L-1)\times(L-1)}$ is a block of the inverse matrix A^{-1}, $R(\rho) = \mathcal{C}\tilde{R}(\rho)\mathcal{C}^T \in \mathbb{R}^{L\times L}$ and $I = (I_1, I_2, \cdots, I_L)^T \in \mathbb{R}^L$ is the vector of injected currents. The vector I is in the sequel called *the current pattern*. Equation (3.52) implies that the dependence between the electrode potentials and the currents is linear. The matrix $R(\rho)$ is called the resistivity matrix.

If there are more than one current pattern α, β and I can be written in matrix form

$$\alpha = \begin{pmatrix} \alpha_1^1 & \alpha_1^2 & \cdots & \alpha_1^{\mathcal{L}} \\ \alpha_2^1 & \alpha_2^2 & \cdots & \alpha_2^{\mathcal{L}} \\ \vdots & \vdots & \ddots & \alpha_1^{\mathcal{L}} \\ \alpha_{\mathcal{N}}^1 & \alpha_{\mathcal{N}}^2 & \cdots & \alpha_{\mathcal{N}}^{\mathcal{L}} \end{pmatrix} \qquad \beta = \begin{pmatrix} \beta_1^1 & \beta_1^2 & \cdots & \beta_1^{\mathcal{L}} \\ \beta_2^1 & \beta_2^2 & \cdots & \beta_2^{\mathcal{L}} \\ \vdots & \vdots & \ddots & \beta_1^{\mathcal{L}} \\ \beta_{L-1}^1 & \beta_{L-1}^2 & \cdots & \beta_{L-1}^{\mathcal{L}} \end{pmatrix}$$

$$\theta = \begin{pmatrix} \alpha \\ \beta \end{pmatrix} \qquad I = \begin{pmatrix} I_1^1 & I_1^2 & \cdots & I_1^{\mathcal{L}} \\ I_2^1 & I_2^2 & \cdots & I_2^{\mathcal{L}} \\ \vdots & \vdots & \ddots & I_1^{\mathcal{L}} \\ I_L^1 & I_L^2 & \cdots & I_L^{\mathcal{L}} \end{pmatrix} ,$$

where $\mathcal{L}$ is the number of the current patterns. For example, if the adjacent current pattern is used the matrix of the current patterns $I \in \mathbb{R}^{L\times\mathcal{L}}$ is

$$I = a \begin{pmatrix} 1 & 0 & 0 & \cdots & -1 \\ -1 & 1 & 0 & \cdots & 0 \\ 0 & -1 & 1 & \cdots & 0 \\ 0 & 0 & -1 & \cdots & 0 \\ \vdots & \vdots & \vdots & \ddots & \vdots \\ 0 & 0 & 0 & \cdots & 1 \end{pmatrix} , \tag{3.53}$$

where a is the amplitude of the injected currents. When $\mathcal{L}$ current patterns are used U^h takes the form

$$U^h = \begin{pmatrix} U_1^1 & U_1^2 & \cdots & U_1^{\mathcal{L}} \\ U_2^1 & U_2^2 & \cdots & U_2^{\mathcal{L}} \\ \vdots & \vdots & \ddots & U_1^{\mathcal{L}} \\ U_L^1 & U_L^2 & \cdots & U_L^{\mathcal{L}} \end{pmatrix}, \tag{3.54}$$

where j'th ($j = 1, ..., \mathcal{L}$) column includes the potentials on the electrodes corresponding to j'th current pattern.

For the static reconstruction voltages U that would correspond the actual measurements are needed. Denote the matrix of measurement patterns by M, analogously to the matrix of current patterns I. The matrix M indicates between which electrodes the voltages are measured. For example in the case of adjacent voltage measurements M is equal to matrix I in (3.53), with $a = 1$. Thus, the voltages U are obtained by multiplying U^h by the transpose of the matrix of the measurement patterns M

$$U = M^T U^h = M^T \mathcal{C} \beta^T, \qquad M \in \mathbb{R}^{L \times \mathcal{L}} \tag{3.55}$$

An alternative formulation for the solution of the complete electrode model with the finite element method can be found in [79].

In EIT, the matrix A is a sparse symmetric positive definite matrix, so the Cholesky factorization

$$A = R^T R\,, \tag{3.56}$$

where R is a general upper-triangular matrix, can be done. Matrix R is called the Cholesky factor of A. Using permutation, in which the rows and/or columns are interchanged, the matrix which have a sparser Cholesky factor than A can be obtained. The sparser the matrix is the faster the set of equation (3.43) is to solve. For the EIT forward problem the existing Matlab [36] routines can be used. Furthermore, the matrix A is positive-definite symmetric matrix which means that θ can solved using conjugate gradient method (see section 2.4.2).

In the equations (3.46–3.48) integrals over the discretized elements (tetrahedron) and over the electrodes (unions of triangles) e_ℓ have to be computed. The conductivity σ is assumed to be constant in each element. These constants are the parameters that are to be estimated in the EIT problem. In the following two sections computation of these integrals using linear and second order basis functions are discussed. More details have been shown in [103].

3.2.3 Integration with linear basis functions

The heart of the integration over the tetrahedron is a mapping which relates the actual element (global element) to an element of more regular shape and with axes in a more convenient position. This element is called the local (or the master) element. A schematic picture of the mapping in the linear case between the local and the global elements is shown in Fig. 3.2 [12, 35, 34].

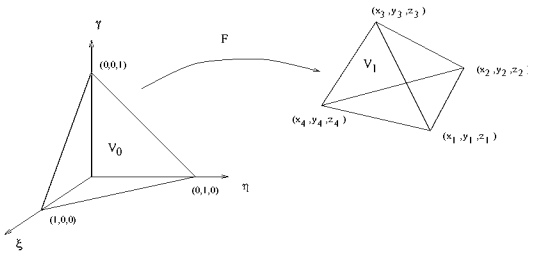

Figure 3.2: The mapping F between a global element E_1 and a local element E_0 in three dimensions.

Using this kind of mapping the following transformation

$$\int_{E_1} g(x,y,z) = \int_{E_0} (g \circ F)(\xi,\eta,\gamma)|J_F| \tag{3.57}$$

can be exploited to compute the integrals over the tetrahedron. In equation (3.57) $(g \circ F) = g(F(\xi,\eta,\gamma))$ is the composite function of F and g, $|J_F|$ is the absolute value of the determinant of the Jacobian J_F and F is an element-specific mapping of the form

$$F(\xi,\eta,\gamma) = \sum_{i=1}^{4} \varphi_i(\xi,\eta,\gamma)(x_i,y_i,z_i) \tag{3.58}$$

when the first order basis functions $\varphi_i(\xi,\eta,\gamma)$ are used. In equation (3.58) (x_i,y_i,z_i) are the nodes of the global element, and the functions $\varphi_i(\xi,\eta,\gamma)$ are the basis functions in the local element E_0. These local basis functions are formed so that the ith basis function takes the value 1 in ith node and zero at each of the others and outside the element E_0 as explained in Section 3.2. The linear basis functions are of form

$$\varphi_1(\xi,\eta,\gamma) = 1-\xi-\eta-\gamma \tag{3.59}$$
$$\varphi_2(\xi,\eta,\gamma) = \xi \tag{3.60}$$
$$\varphi_3(\xi,\eta,\gamma) = \eta \tag{3.61}$$
$$\varphi_4(\xi,\eta,\gamma) = \gamma\,. \tag{3.62}$$

With these transformations all the integrals over the global elements can be calculated as integrals over the local element. In the equation (3.46) the integral over the tetrahedron can be written with the formula (3.57) in the form

$$\int_{E_1} \sigma \nabla\varphi_j^{(e)} \cdot \nabla\varphi_i^{(e)}\, dx\, dy\, dz$$

$$= \sigma \int_{E_0} ((\nabla\varphi_j^{(e)} \cdot \nabla\varphi_i^{(e)}) \circ F)|J_F|\, d\xi\, d\eta\, d\gamma$$

$$= \sigma \int_{E_0} ((\nabla \varphi_j^{(e)} \circ F) \cdot (\nabla \varphi_i^{(e)} \circ F)) \, |J_F| \, d\xi \, d\eta \, d\gamma \ , \tag{3.63}$$

where $\varphi_i^{(e)}$ denotes the basis function of the global element. The gradients of the basis functions that are needed in the integrations can be computed with the aid of the chain rule of differentiation. For saving the computational time the integral (3.63) can be written in the matrix form so that the gradients of all basis functions corresponding to each element can be computed at the same time. For all basis functions the integral takes the form

$$\sigma \int_{E_0} ((\nabla N_e \circ F) \cdot (\nabla N_e \circ F)) \, |J_F| \, d\xi \, d\eta \, d\gamma \ . \tag{3.64}$$

where

$$N_e = \begin{bmatrix} \varphi_1^{(e)} & \varphi_2^{(e)} & \varphi_3^{(e)} & \varphi_4^{(e)} \end{bmatrix} . \tag{3.65}$$

In [103] it has been shown the the integral (3.64) can also be written in form

$$\sigma \int_{E_0} ((J_F^T)^{-1} L)^T ((J_F^T)^{-1} L) \, |J_F| \, d\xi \, d\eta \, d\gamma \ , \tag{3.66}$$

where

$$L = \begin{bmatrix} \frac{\partial \varphi_1}{\partial \xi} & \frac{\partial \varphi_2}{\partial \xi} & \frac{\partial \varphi_3}{\partial \xi} & \frac{\partial \varphi_4}{\partial \xi} \\ \frac{\partial \varphi_1}{\partial \eta} & \frac{\partial \varphi_2}{\partial \eta} & \frac{\partial \varphi_3}{\partial \eta} & \frac{\partial \varphi_4}{\partial \eta} \\ \frac{\partial \varphi_1}{\partial \gamma} & \frac{\partial \varphi_2}{\partial \gamma} & \frac{\partial \varphi_3}{\partial \gamma} & \frac{\partial \varphi_4}{\partial \gamma} \end{bmatrix} , \tag{3.67}$$

where $\varphi_i = \varphi_i(\xi, \eta, \gamma)$. When linear basis function are used the matrices J_F and L do not depend on local coordinates (ξ, η, γ). The integral of the equation (3.66) can be difficult to compute when the higher order basis functions are used. Therefore, a numerical integration scheme (Gaussian quadrature) is utilized and the integral is approximated with the finite sum [35]

$$\int_{E_0} \hat{g}(\xi, \eta, \gamma) \, d\xi \, d\eta \, d\gamma = \sum_{i=1}^{n} W_i \hat{g}(\bar{\xi}_i, \bar{\eta}_i, \bar{\gamma}_i) \ . \tag{3.68}$$

The weighting coefficients W_i and the integration points $\bar{\xi}_i$, $\bar{\eta}_i$ and $\bar{\gamma}_i$ are shown in the Table 3.1 [19].

In equations (3.46–3.47) the surface integrals over the electrodes e_ℓ is needed. The mesh is constructed so that the electrodes correspond to (a union of) some element faces and therefore the surface integrals are over some faces of the tetrahedron. In the integration over the face of the element the transformation

$$\int_{K_1} g(x, y, z) = \int_{K_0} (g \circ F)(\xi, \eta) \| \partial_\xi F \times \partial_\eta F \| d\xi \, d\eta \tag{3.69}$$

where ∂_ξ refers to differentiation with respect to ξ, ∂_η to differentiation with respect to η and $\| \cdot \|$ denotes the used norm. The basis functions and the mapping F in (3.69) can be constructed from (3.58) by setting $\gamma = 0$.

Table 3.1: The weighting coefficients W_i of the numerical integration scheme (3.68) and the integration points $\bar{\xi}_i$, $\bar{\eta}_i$ and $\bar{\gamma}_i$, $\alpha = 0.58541020$ and β=0.13819660, n denotes the number of integration points.

	i	$\bar{\xi}_i$	$\bar{\eta}_i$	$\bar{\gamma}_i$	W_i
n=1	1	$\frac{1}{4}$	$\frac{1}{4}$	$\frac{1}{4}$	$\frac{1}{6}$
n=4	1	β	β	β	$\frac{1}{24}$
	2	α	β	β	$\frac{1}{24}$
	3	β	α	β	$\frac{1}{24}$
	4	β	β	α	$\frac{1}{24}$

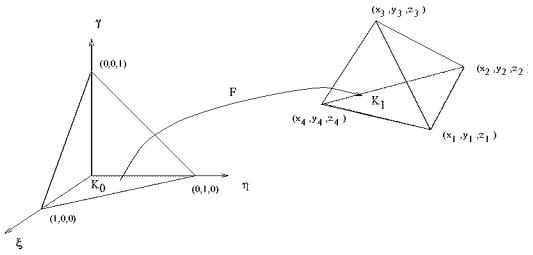

Figure 3.3: The mapping F between a global element K_1 and a local element K_0 in three dimensions.

The latter integral of the equation (3.46) can be computed as

$$\int_{e_\ell} \varphi_i^{(e)} \varphi_j^{(e)} \, dS = \int_{K_0} ((\varphi_i^{(e)} \varphi_j^{(e)}) \circ F)(\xi, \eta) \parallel \partial_\xi F \times \partial_\eta F \parallel \, d\xi \, d\eta$$

$$= \int_{K_0} (\varphi_i^{(e)} \circ F)(\xi, \eta)(\varphi_j^{(e)} \circ F)(\xi, \eta) \parallel \partial_\xi F \times \partial_\eta F \parallel \, d\xi \, d\eta$$

$$= \int_{K_0} \varphi_i(\xi, \eta) \varphi_j(\xi, \eta) \parallel \partial_\xi F \times \partial_\eta F \parallel \, d\xi \, d\eta \tag{3.70}$$

or all the products of the basis functions at the same time

$$\int_{e_\ell} N_e^T N_e \, dS$$

$$= \int_{K_0} N^T(\xi, \eta) N(\xi, \eta) \parallel \partial_\xi F \times \partial_\eta F \parallel \, d\xi \, d\eta \, . \tag{3.71}$$

Respectively, the integral of the equation (3.47) can be formulated as

$$\int_{e_\ell} \varphi_i^{(e)} \, dS = \int_{K_0} (\varphi_i^{(e)} \circ F)(\xi, \eta) \parallel \partial_\xi F \times \partial_\eta F \parallel \, d\xi \, d\eta$$

Table 3.2: The weighting coefficients W_i of the Radau's rule (3.74) and the integration points $\bar{\xi}_i$, $\bar{\eta}_i$ and $\bar{\gamma}_i$.

	i	$\bar{\xi}_i$	$\bar{\eta}_i$	W_i
n=1	1	$\frac{1}{3}$	$\frac{1}{3}$	$\frac{1}{2}$
n=3	1	$\frac{1}{2}$	0	$\frac{1}{6}$
	2	$\frac{1}{2}$	$\frac{1}{2}$	$\frac{1}{6}$
	3	0	$\frac{1}{2}$	$\frac{1}{6}$
n=7	1	0	0	$\frac{1}{40}$
	2	$\frac{1}{2}$	0	$\frac{1}{15}$
	3	1	0	$\frac{1}{40}$
	4	$\frac{1}{2}$	$\frac{1}{2}$	$\frac{1}{15}$
	5	0	1	$\frac{1}{40}$
	6	0	$\frac{1}{2}$	$\frac{1}{15}$
	7	$\frac{1}{3}$	$\frac{1}{3}$	$\frac{9}{40}$

$$= \int_{K_0} \varphi_i(\xi,\eta) \parallel \partial_\xi F \times \partial_\eta F \parallel d\xi\, d\eta \,. \tag{3.72}$$

For all the basis functions

$$\int_{e_\ell} N_e \, dS$$

$$= \int_{K_0} N(\xi,\eta) \parallel \partial_\xi F \times \partial_\eta F \parallel d\xi\, d\eta \,. \tag{3.73}$$

Hence the surface integrals of the global basis functions over the global elements are converted to the surface integrals of the local basis functions over the local element. Radau's rule is used for the numerical integration of the equations (3.71) and (3.73) [35]

$$\int_{K_0} \hat{g}(\xi,\eta) d\xi d\eta = \sum_{i=1}^{n} W_i \hat{g}(\bar{\xi}_i, \bar{\eta}_i) \,. \tag{3.74}$$

The weighting coefficients W_i and the integration points $\bar{\xi}_i$ and $\bar{\eta}_i$ are shown in the Table 3.2 [35].

3.2.4 Integration with second order basis functions

In the quadratic case there would be six more nodes between the vertices of the elements and in addition the global element could be curve sided. In this case the additional 6 nodes are located in the middle of each edge of the local element E_0

when the basis functions of the local element are [35]

$$\tilde{\varphi}_1(\xi,\eta,\gamma) = (2q-1)q \tag{3.75}$$
$$\tilde{\varphi}_2(\xi,\eta,\gamma) = (2\xi-1)\xi \tag{3.76}$$
$$\tilde{\varphi}_3(\xi,\eta,\gamma) = (2\eta-1)\eta \tag{3.77}$$
$$\tilde{\varphi}_4(\xi,\eta,\gamma) = (2\gamma-1)\gamma \tag{3.78}$$
$$\tilde{\varphi}_5(\xi,\eta,\gamma) = 4\xi q \tag{3.79}$$
$$\tilde{\varphi}_6(\xi,\eta,\gamma) = 4\xi\eta \tag{3.80}$$
$$\tilde{\varphi}_7(\xi,\eta,\gamma) = 4\eta q \tag{3.81}$$
$$\tilde{\varphi}_8(\xi,\eta,\gamma) = 4\gamma q \tag{3.82}$$
$$\tilde{\varphi}_9(\xi,\eta,\gamma) = 4\xi\gamma \tag{3.83}$$
$$\tilde{\varphi}_{10}(\xi,\eta,\gamma) = 4\eta\gamma \tag{3.84}$$

where

$$q = 1-\xi-\eta-\gamma\ .$$

When the second order basis functions $\tilde{\varphi}_i(\xi,\eta,\gamma)$ are used the mapping F is of the form

$$\tilde{F}(\xi,\eta,\gamma) = \sum_{i=1}^{10} \tilde{\varphi}_i(\xi,\eta,\gamma)(x_i,y_i,z_i)\ . \tag{3.85}$$

Formally the computation of the integrals with second order basis functions equals to the case with linear basis functions. However, computation of the gradients is more complicated with second order basis functions and the matrices J_F and L depend on local coordinates (ξ,η,γ) [103].

3.3 Infinite elements

Unbounded domain appear in a wide variety of practical engineering problems. In this section two different infinite element methods are described in 1D. The first one is based on choosing of the shape functions [8] and the second one on mapped infinite elements [61, 90, 118]. Convergence analysis of the infinite elements of the type $\frac{1}{r^n}$ where n is greater or equal to 1 is discussed in [25].

3.3.1 Infinite elements based on choosing of the basis functions

In choosing a basis function for an element which extends to infinity there are two requirements to satisfy. First, the basis function should be realistic and second, it should lead to the integrations over the element domain which are finite [8]. The basis functions can be chosen based on Lagrange polynomials multiplied by exponential decay. If there are n nodes in the infinite element, the first $n-1$ having finite t coordinates and the n'th being infinitely distant, a set of basis functions φ_i is defined for $i = 1,...,n-1$

$$\varphi_i = \varphi_i(t) = e^{(t_i - t)/L} \prod_{j=1, j\neq i}^{n-1} \left(\frac{t_j - t}{t_j - t_i} \right) . \tag{3.86}$$

This is comparable with the conventional Lagrange polynomial $\mathcal{M}_i$

$$\mathcal{M}_i = \prod_{j=1, j\neq i}^{n-1} \left(\frac{t_j - t}{t_j - t_i} \right) . \tag{3.87}$$

In equation (3.86) L determines the rate of the exponential decay. If φ_n is required it can be found from

$$\varphi_n = 1 - \sum_{i=1}^{n-1} \varphi_i . \tag{3.88}$$

Basis functions for the infinite element are shown in Fig. 3.4.

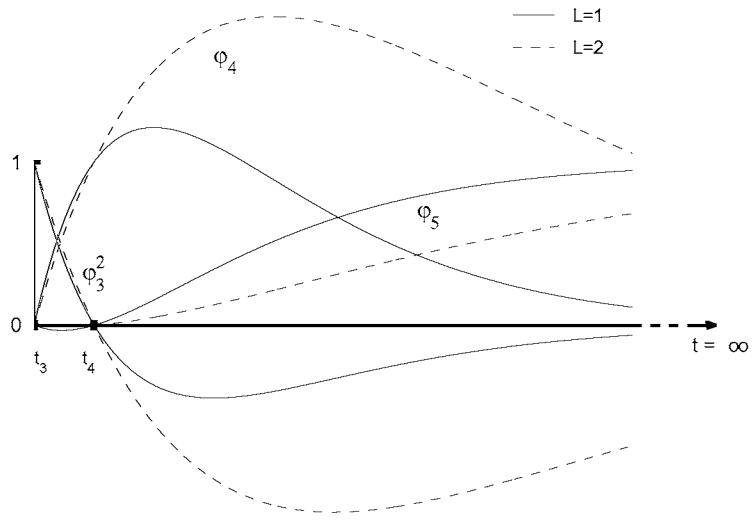

Figure 3.4: The basis functions for infinite element with two different values for L. The nodes are $t_3 = 1$ and $t_4 = \frac{3}{2}$ and the basis functions $\varphi_3^2 = 2e^{(1-t)/L}(\frac{3}{2} - t)$, $\varphi_4 = -2e^{(\frac{3}{2}-t)/L}(1-t)$ and $\varphi_5 = 1 - (\varphi_3^2 + \varphi_4)$.

3.3.2 Mapped infinite elements

Mapped infinite elements are based on a simple mapping technique that applies to both the modelling of the geometry and the field variables (solution of the partial differential equation) [61],[90]. Let us consider the one-dimensional case

shown in Fig. 3.6 in which the infinite element ranging from node 1 to node 3 (at infinity) through node 2 is mapped onto the local element defined by the local coordinate system $-1 \leq \xi \leq 1$. Point t_0 in global coordinates is called the pole of the transformation and is positioned arbitrarily, with the only restriction that, once it is positioned, the location of node 2 is defined by

$$t_2 = 2t_1 - t_0 \ . \tag{3.89}$$

The mapping from the local to the global coordinates is obtained by means of the standard finite element method for isoparametric elements

$$F(\xi) = t = \sum_{i=1}^{2} M_i(\xi) t_i \tag{3.90}$$

where the summation extends over the finite nodes only and the mapping functions are

$$M_1(\xi) = \frac{-2\xi}{1-\xi} \tag{3.91}$$

$$M_2(\xi) = \frac{1+\xi}{1-\xi} \ . \tag{3.92}$$

From these relations it follows that in global coordinates the positions $t = t_1, t_2, \infty$ correspond to the points $\xi = -1, 0, 1$. The mapping functions M_1 and M_2 are plotted in Fig. 3.7.

The requirement that the mapping must be independent of the choice of coordinate system necessitates that $M_1(\xi) + M_2(\xi) = 1$ [61]. Standard basis functions in local system of coordinates for the three-node element $-1 \leq \xi \leq 1$ are

$$\varphi_1(\xi) = \frac{1}{2}\xi(\xi - 1) \tag{3.93}$$

$$\varphi_2(\xi) = 1 - \xi^2 \tag{3.94}$$

$$\varphi_3(\xi) = \frac{1}{2}\xi(\xi + 1) \tag{3.95}$$

and the solution u can be interpolated using these basis functions

$$u(\xi) = \sum_{i=1}^{3} u_i \varphi_i(\xi) = \frac{1}{2}\xi(\xi-1)u_1 + (1-\xi^2)u_2 + \frac{1}{2}\xi(\xi+1)u_3 \tag{3.96}$$

where u_i is the value of the solution at the i'th node. Let us solve ξ from the equation (3.90)

$$\xi = \xi(t) = \frac{t_2 - t}{2t_1 - t_2 - t} \ . \tag{3.97}$$

When $a = t_2 - t_1 = t_1 - t_0$ and $r = t - t_0$ as in Fig. 3.6

$$t_2 = a + t_1 \tag{3.98}$$

$$r = a - t_1 + t \tag{3.99}$$

are obtained. When the equations (3.98) and (3.99) are inserted in the equation (3.97)

$$\xi = \frac{a + t_1 - t}{t_1 - a - t} \tag{3.100}$$

$$= \frac{t - t_1 - a + 2a - 2a}{r} \tag{3.101}$$

$$= \frac{t - t_1 + a - 2a}{r} \tag{3.102}$$

$$= \frac{r - 2a}{r} \tag{3.103}$$

$$= 1 - \frac{2a}{r} \, . \tag{3.104}$$

Substituting (3.104) in (3.96) gives the unknown $u(\xi)$ in terms of the global coordinate, r, as follows

$$u(1 - \frac{2a}{r}) = u_3 + (-u_1 + 4u_2 - 3u_3)\frac{a}{r} + (2u_1 - 4u_2 + 2u_3)\frac{a^2}{r^2} \, . \tag{3.105}$$

Thus the decay of the (approximative) solution is of the form $\frac{1}{r^2}$.

If the linear element (nodes -1 and 1, $\varphi_1 = \frac{1}{2} - \frac{1}{2}\xi$, $\varphi_2 = \frac{1}{2} + \frac{1}{2}\xi$) is chosen to be a 1D local element the solution $u(\xi)$ of the differential equation is

$$u(\xi) = \left(\frac{1}{2} - \frac{1}{2}\xi\right) u_1 + \left(\frac{1}{2} + \frac{1}{2}\xi\right) u_2 \, . \tag{3.106}$$

Let us insert the equation (3.104) in the equation (3.106) to obtain

$$u(1 - \frac{2a}{r}) = u_2 + (u_1 - u_2)\frac{a}{r} \, . \tag{3.107}$$

As it can be seen, if the linear element is used the decay of the (approximative) solution is of the form $\frac{1}{r}$.

3.3.3 Positioning of poles (t_0)

The geometry and the unknown variable expansions involved in the mapped infinite element technique are both referred to the same point or a set of points termed the pole(s). Therefore the geometric and the physical characteristics of the problem must both be taken into account when positioning the pole(s). The reference pole must be exterior to the infinite element. Also the element faces in higher dimensions extending to infinity must be either of parallel or of a diverging type and in no case should these be of a converging type, since convergence would lead to overlapping of elements and non-uniqueness of mapping. It is also essential to explore the effect of shifting of the pole position to improve the decay characteristics. To ensure continuity across the transition boundary between finite and infinite elements, the number and location of the connecting nodes must coincide. The results for the different pole positions of the previous example are presented in Fig. 3.8.

3.3.4 Infinite element methods in EIT

In many cases the object to be imaged is so large that extending the computational domain to cover the whole object would lead extremely large dimensional systems of equations in the FEM. For this reason, the computational domain usually covers only a part of the object. However, cutting of the domain causes errors in the computed potentials since the electric field also spreads outside the domain. The problem due to cutting effect can be significantly reduced by using the *infinite elements* [9] in the computation.

When using infinite elements the object is assumed to extend to infinity in some direction(s) The decay of the potentials along some axis can be approximated with infinite elements. In this thesis the separable infinite elements have been used for the modelling of the far field behavior. This method is suitable only in situations in which the object to be imaged is symmetric along one axis and the domain is assumed to extend to infinity along this axis. The separable infinite elements would be the most suitable in the industrial applications since the long pipes to be imaged are cylindrical. In medicine the infinite element approach might be applicable in the imaging of the human leg or thorax which are almost symmetrical. In these situations the voltages may decay enough so that the infinite elements can be used.

Let us assume that the shape functions of the 3D infinite elements are separable

$$\varphi_j = \begin{cases} \varphi_j(x,y,z) & ,(x,y,z) \in \Omega_1 \\ \varphi_k(x,y)\,\phi_l(z) & ,(x,y,z) \in \Omega_2 \end{cases} \tag{3.108}$$

$\varphi_k(x,y)$ are the basis functions of the 2D element, $\phi_l(z)$ are the basis functions of the 1D element, Ω_1 is a domain of the finite elements and Ω_2 is a domain of the infinite elements. In Ω_2, the integration over the 3D element in the equation (3.46) can be written in the form

$$\int_E \nabla(\varphi_i^{(e)}(x,y)\phi_j^{(e)}(z)) \cdot \nabla(\varphi_k^{(e)}(x,y)\phi_l^{(e)}(z))\,dx\,dy\,dz$$

$$
\begin{aligned}
&= \int_E (\frac{\partial}{\partial x}, \frac{\partial}{\partial y}, \frac{\partial}{\partial z})(\varphi_i^{(e)}(x,y)\phi_j^{(e)}(z)) \cdot (\frac{\partial}{\partial x}, \frac{\partial}{\partial y}, \frac{\partial}{\partial z})(\varphi_k^{(e)}(x,y)\phi_l^{(e)}(z))\, dx\, dy\, dz \\
&= \int_E \left\{ \left[\left(\frac{\partial \varphi_i^{(e)}(x,y)}{\partial x}, \frac{\partial \varphi_i^{(e)}(x,y)}{\partial y}, 0 \right) \phi_j^{(e)}(z) + \left(0, 0, \frac{\partial \phi_j^{(e)}(z)}{\partial z} \right) \varphi_i^{(e)}(x,y) \right] \right. \\
&\left. \cdot \left[\left(\frac{\partial \varphi_k^{(e)}(x,y)}{\partial x}, \frac{\partial \varphi_k^{(e)}(x,y)}{\partial y}, 0 \right) \phi_l^{(e)}(z) + \left(0, 0, \frac{\partial \phi_l^{(e)}(z)}{\partial z} \right) \varphi_k^{(e)}(x,y) \right] \right\} dx\, dy\, dz \\
&= \int_E \left\{ \left(\frac{\partial \varphi_i^{(e)}(x,y)}{\partial x} \phi_j^{(e)}(z), \frac{\partial \varphi_i^{(e)}(x,y)}{\partial y} \phi_j^{(e)}(z), \frac{\partial \phi_j^{(e)}(z)}{\partial z} \varphi_i^{(e)}(x,y) \right) \right. \\
&\left. \cdot \left(\frac{\partial \varphi_k^{(e)}(x,y)}{\partial x} \phi_l^{(e)}(z), \frac{\partial \varphi_k^{(e)}(x,y)}{\partial y} \phi_l^{(e)}(z), \frac{\partial \phi_l^{(e)}(z)}{\partial z} \varphi_k^{(e)}(x,y) \right) \right\} dx\, dy\, dz \\
&= \int_E \left(\frac{\partial \varphi_i^{(e)}(x,y)}{\partial x} \frac{\partial \varphi_k^{(e)}(x,y)}{\partial x} + \frac{\partial \varphi_i^{(e)}(x,y)}{\partial y} \frac{\partial \varphi_k^{(e)}(x,y)}{\partial y} \right) \phi_j^{(e)}(z) \phi_l^{(e)}(z)\, dx\, dy\, dz \\
&+ \int_E \frac{\partial \phi_j^{(e)}(z)}{\partial z} \frac{\partial \phi_l^{(e)}(z)}{\partial z} \varphi_i^{(e)}(x,y) \varphi_k^{(e)}(x,y)\, dx\, dy\, dz \\
&= \int_K \nabla \varphi_i^{(e)}(x,y) \cdot \nabla \varphi_k^{(e)}(x,y)\, dx\, dy \int_S \phi_j^{(e)}(z) \phi_l^{(e)}(z)\, dz \\
&+ \int_S \nabla \phi_j^{(e)}(z) \cdot \nabla \phi_l^{(e)}(z)\, dz \int_K \varphi_i^{(e)}(x,y) \varphi_k^{(e)}(x,y)\, dx\, dy
\end{aligned} \tag{3.109}
$$

where K is the 2D element and S is the 1D element (see Fig. 3.9). The integrals over the global elements (K, S) in equation (3.109) can be replaced by integrals over the local elements (K_0, S_0).

$$
\begin{aligned}
&\int_K \nabla \varphi_i^{(e)}(x,y) \cdot \nabla \varphi_k^{(e)}(x,y)\, dx\, dy \int_S \phi_j^{(e)}(z) \phi_l^{(e)}(z)\, dz \\
&+ \int_S \nabla \phi_j^{(e)}(z) \cdot \nabla \phi_l^{(e)}(z)\, dz \int_K \varphi_i^{(e)}(x,y) \varphi_k^{(e)}(x,y)\, dx\, dy \\
&= \int_{K_0} ((J_{F_2}^T)^{-1} L_i(\xi,\eta))^T ((J_{F_2}^T)^{-1} L_k(\xi,\eta)) |J_{F_2}|\, d\xi\, d\eta \int_{S_0} \phi_j(\gamma) \phi_l(\gamma) |J_{F_1}|\, d\gamma \\
&+ \int_{S_0} ((J_{F_1}^T)^{-1} L_j(\gamma))^T ((J_{F_1}^T)^{-1} L_l(\gamma)) |J_{F_1}|\, d\gamma \int_{K_0} \varphi_i(\xi,\eta) \varphi_k(\xi,\eta) |J_{F_2}|\, d\xi\, d\eta
\end{aligned}
$$

The integrals over the 2D elements in the equation (3.109) can be calculated by using mapping method. The Jacobian matrix can be obtained from

$$
J_{F_2} = L(\xi,\eta) X_2 \tag{3.110}
$$

where X_2 are the nodes of the 2D global element. The basis functions φ_i are

obtained from the 3D basis functions (3.75–3.84) by setting $\gamma = 0$

$$L(\xi,\eta) = \begin{bmatrix} \frac{\partial\varphi_1}{\partial\xi} & \frac{\partial\varphi_2}{\partial\xi} & \frac{\partial\varphi_3}{\partial\xi} & \frac{\partial\varphi_4}{\partial\xi} & \frac{\partial\varphi_5}{\partial\xi} & \frac{\partial\varphi_6}{\partial\xi} \\ \frac{\partial\varphi_1}{\partial\eta} & \frac{\partial\varphi_2}{\partial\eta} & \frac{\partial\varphi_3}{\partial\eta} & \frac{\partial\varphi_4}{\partial\eta} & \frac{\partial\varphi_5}{\partial\eta} & \frac{\partial\varphi_6}{\partial\eta} \end{bmatrix} \tag{3.111}$$

$$= \begin{bmatrix} -2+4\xi+4\eta & 4\xi-1 & 0 & 4-4\eta-8\xi & 4\eta & -4\eta \\ -2+4\xi+4\eta & 0 & 4\eta-1 & -4\xi & 4\xi & 4-4\xi-8\eta \end{bmatrix} \tag{3.112}$$

Note that the subscripts of the basis functions are different from the ones in (3.75–3.84).

If the γ- direction is assumed to extend to the infinity and mapped infinite elements and $\frac{1}{r^2}$ decay are used J_{F_1} can be obtained as in the equation (3.110) and

$$L(\gamma) = \begin{bmatrix} \frac{d\phi_1(\gamma)}{d\gamma} & \frac{d\phi_2(\gamma)}{d\gamma} \end{bmatrix} = \begin{bmatrix} \gamma - \frac{1}{2} & 2\gamma \end{bmatrix} \tag{3.113}$$

where $\phi_1(\gamma) = \frac{1}{2}\gamma(\gamma-1)$ and $\phi_2(\gamma) = 1-\gamma^2$ are the basis functions of the 1D local element whose nodes are $-1, 0, 1$ (compare with the equations (3.93) and (3.94)). The basis function for the local node 1 is not needed because the voltages in it are assumed to be zero. This means that there is the homogeneous Dirichlet boundary condition at infinity which also defines the ground potential. The condition (3.25) is not used in this case.

If exponential decay is used the basis functions can be chosen as explained in Section 3.3.1. In that case, the integrals (in γ-direction) in the equation (3.109) are computed over the global 1D elements from z_1 to infinity. The global elements in z-direction are same in every element and therefore the integrals need to be computed only for one element.

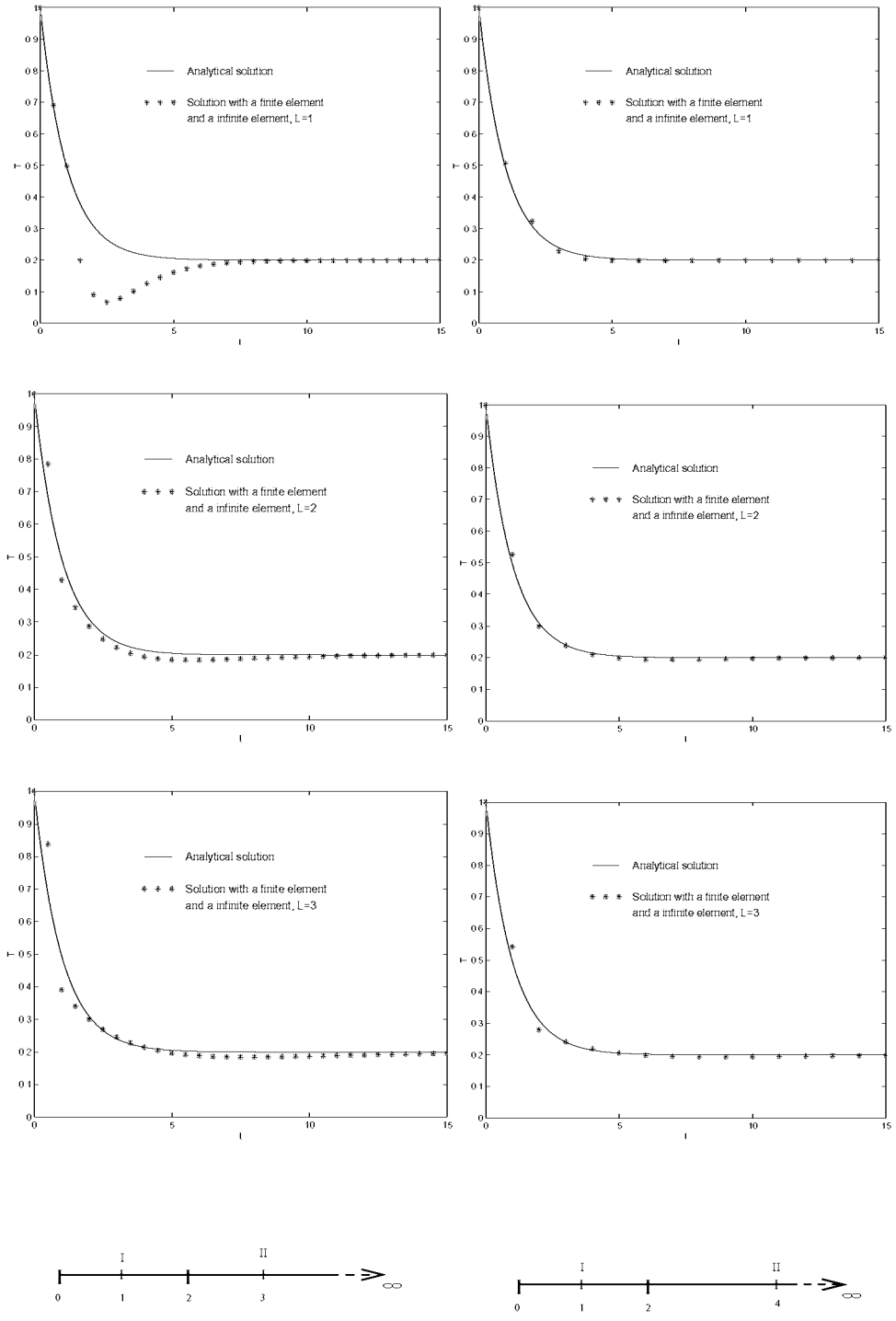

Figure 3.5: The role of the parameter L for two different meshes. The mesh which has been used is shown below the series of figures.

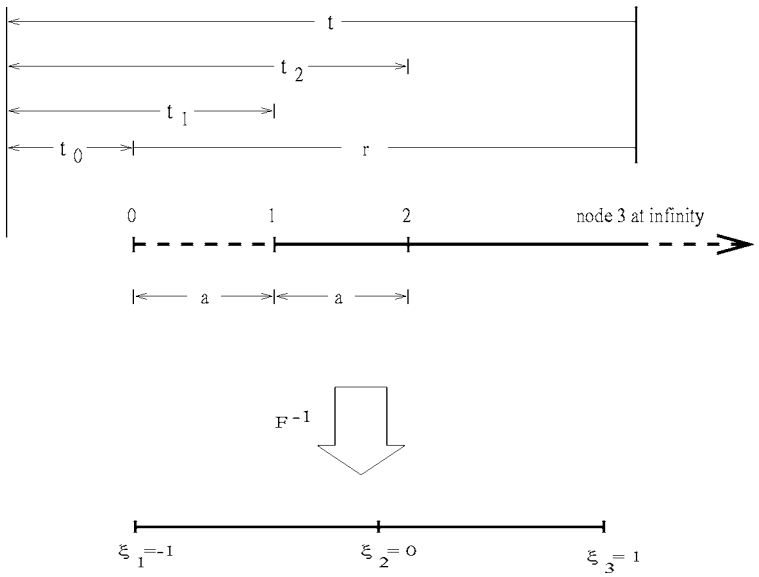

Figure 3.6: Mapping between a local element and a global infinite element in one dimension [61].

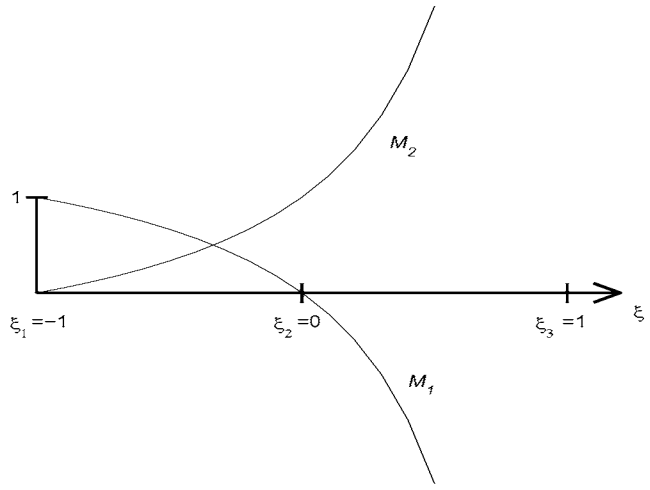

Figure 3.7: The mapping functions for the one dimensional infinite element. $M_1 = M_1(\xi) = -2\xi/(1-\xi)$ and $M_2 = M_2(\xi) = (1+\xi)/(1-\xi)$.

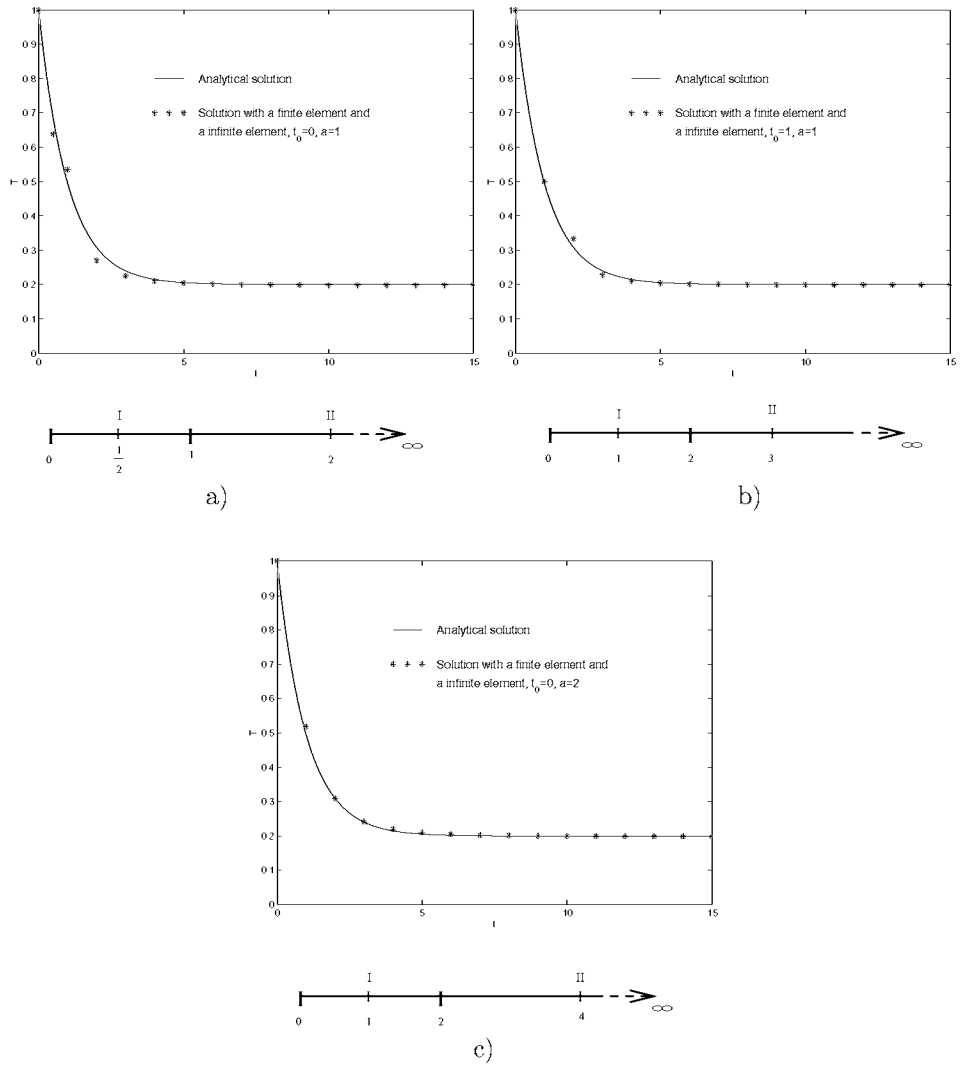

Figure 3.8: The role of the pole position. a) The position of the pole $t_0 = 0$, $t_2 = 2$ and $a = 1$, b) $t_0 = 1$, $t_2 = 3$ and $a = 1$, c) $t_0 = 0$, $t_2 = 4$ and $a = 2$. The mesh which has been used is shown below the figures.

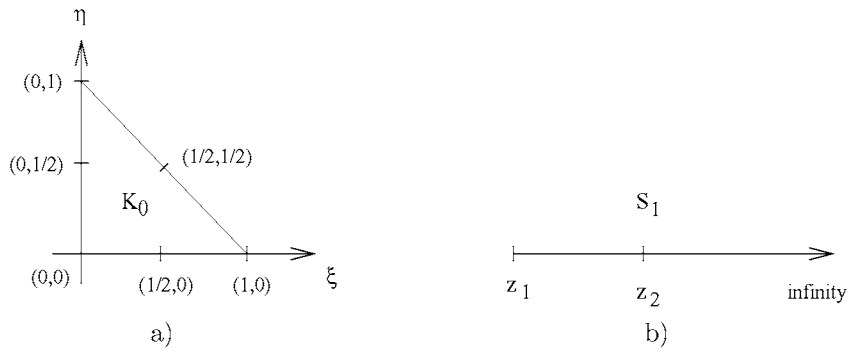

Figure 3.9: a) a local 2D element, b) a global 1D infinite element.

CHAPTER IV

Inverse problem in EIT

In EIT the injected currents are known and the formed voltages can be measured. The inverse problem is to determine the parameters σ (conductivity distribution) of the mathematical model. There have been many studies on the uniqueness of the recovery of the conductivity inside an object based on the measurements made on the boundary of the object also for the three-dimension case if conductivity distribution is isotropic [91, 16]. EIT inverse problem is both ill-posed and nonlinear with respect to conductivity distribution. Furthermore, especially in three-dimensional cases, the number of the parameters which has to be solved can be huge, when the approaches which are effective for two-dimensional problems are inappropriate.

In this thesis the inverse problem of EIT is considered as an LS-problem. Since the inverse problem is ill-posed, one has to consider minimization of the regularized functional

$$F(\rho) = \|U_{\text{meas}} - U(\rho, z_0)\|_2^2 + \lambda^2 \|L_2(\rho - \rho^*)\|_2^2 \tag{4.1}$$

where U_{meas} and $U(\rho, z_0)$ are the vectors of the measured and computed voltages on the electrodes, λ is the regularization parameter, ρ is estimated resistivity distribution, ρ^* is the prior for the solution and L_2 is the regularization matrix. In equation (4.1) z_0 is the contact impedance which is assumed to be known. See [111, 33] for estimating the contact impedances simultaneously with the resistivity distribution.

4.1 The Jacobian matrix in EIT

In EIT the parameter x in the Chapter 2 is the resistivity distribution ρ, $h(x)$ are the calculated voltages $U(\rho, z_0)$ in some distribution ρ and z measured potentials U_{meas}. The Jacobian can be computed as follows. Assume, that the resistivity distribution is piecewise constant, i.e.

$$\rho = \sum_{m=1}^{N} \rho_m \chi_m \tag{4.2}$$

where N is number of the elements in FEM discretization and χ_m is the characteristic function of the m'th element. Consider a matrix

$$\tilde{\mathcal{C}} = \begin{pmatrix} 0 & \mathcal{C} \end{pmatrix} \tag{4.3}$$

where $0 \in \mathbb{R}^{L \times \mathcal{N}}$. The derivatives of the voltages $U^h = \mathcal{C}\beta^T$ on the electrodes with respect to each ρ_m are wanted to be determined for the Jacobian matrix. By using the equation (4.3) it can be obtained that $U^h = \mathcal{C}\beta^T = \tilde{\mathcal{C}}\theta$ where $\theta = (\alpha, \beta)^T$. Now

$$\frac{\partial U^h}{\partial \rho_m} = \frac{\partial(\tilde{\mathcal{C}}\theta)}{\partial \rho_m} \tag{4.4}$$

is wanted to be computed. If measurement pattern $M \in \mathbb{R}^{L \times K}$, where K is the number of measurements made, is used, the voltages on the electrodes become $U = M^T U^h = M^T \tilde{\mathcal{C}}\theta = \tilde{M}\theta$ and the derivative becomes

$$\frac{\partial U}{\partial \rho_m} = \frac{\partial(\tilde{M}\theta)}{\partial \rho_m} = \tilde{M}\frac{\partial \theta}{\partial \rho_m} \, . \tag{4.5}$$

Consider the term $\frac{\partial \theta}{\partial \rho_m}$. From the equation (3.43) it can be obtained

$$\frac{\partial \theta}{\partial \rho_m} = \frac{\partial(A^{-1}f)}{\partial \rho_m} \, . \tag{4.6}$$

The right hand side of (4.6) can be expanded as

$$\frac{\partial(A^{-1}f)}{\partial \rho_m} = -A^{-1}\frac{\partial A}{\partial \rho_m}A^{-1}f = -A^{-1}\frac{\partial A}{\partial \rho_m}\theta \, . \tag{4.7}$$

Since only the matrix B in A depends on ρ the derivative $\partial A/\partial \rho_m$ can be computed as

$$\frac{\partial A}{\partial \rho_m} = \begin{pmatrix} \frac{\partial B}{\partial \rho_m} & 0 \\ 0 & 0 \end{pmatrix} \tag{4.8}$$

where

$$\frac{\partial B(i,j)}{\partial \rho_m} = -\frac{1}{\rho_m^2}\int_{\mathrm{supp}(\chi_m)} \nabla\varphi_i \cdot \nabla\varphi_j \, dx\, dy\, dz, \;\; i,j = 1,2,\ldots,\mathcal{N} \, . \tag{4.9}$$

Here $\mathrm{supp}(\chi_m)$ denotes the support of the function χ_m. Now the derivatives with respect to the actual measurements become

$$\begin{aligned} \frac{\partial U}{\partial \rho_m} &= \tilde{M}\frac{\partial \theta}{\partial \rho_m} = -\tilde{M}A^{-1}\frac{\partial A}{\partial \rho_m}\theta \\ &= -\left((A^{-1})^T\tilde{M}^T\right)^T\frac{\partial A}{\partial \rho_m}\theta = -\left(A^{-1}\tilde{M}^T\right)^T\frac{\partial A}{\partial \rho_m}\theta \\ &= -\gamma^T\frac{\partial A}{\partial \rho_m}\theta \end{aligned} \tag{4.10}$$

where $\gamma = A^{-1}\tilde{M}^T \in \mathbb{R}^{\mathcal{N}+(L-1)\times K}$, where K was the number of actual measurements. The last steps are based on the fact that the matrix A is symmetric. In (4.10) there are two separate potential distributions, θ from the true injected currents and γ that is due to the measurement pattern $\tilde{M}^T = (M^T\tilde{C})^T$. The matrix obtained from the equation (4.10) is $\mathbb{R}^{K\times\mathcal{L}}$ where $\mathcal{L}$ was the number of current patterns (right hand sides). After reshaping the m'th column of the Jacobian is obtained. The same procedure is carried out for each ρ_m to obtain the other columns of J. Similar procedure to compute the Jacobian has been utilized also for example in optical tomography and is known as the *adjoint differentiation* [2]. The Jacobian matrix is of form

$$J = \begin{pmatrix} \frac{\partial U_1^1}{\partial \rho_1} & \frac{\partial U_1^1}{\partial \rho_2} & \cdots & \frac{\partial U_1^1}{\partial \rho_M} \\ \frac{\partial U_2^1}{\partial \rho_1} & \frac{\partial U_2^1}{\partial \rho_2} & \cdots & \frac{\partial U_2^1}{\partial \rho_M} \\ \vdots & \vdots & \vdots & \vdots \\ \frac{\partial U_K^1}{\partial \rho_1} & \frac{\partial U_K^1}{\partial \rho_2} & \cdots & \frac{\partial U_K^1}{\partial \rho_M} \\ \frac{\partial U_1^2}{\partial \rho_1} & \frac{\partial U_1^2}{\partial \rho_2} & \cdots & \frac{\partial U_1^2}{\partial \rho_M} \\ \vdots & \vdots & \vdots & \vdots \\ \frac{\partial U_K^2}{\partial \rho_1} & \frac{\partial U_K^2}{\partial \rho_2} & \cdots & \frac{\partial U_K^2}{\partial \rho_M} \\ \vdots & \vdots & \vdots & \vdots \\ \frac{\partial U_K^{\mathcal{L}}}{\partial \rho_1} & \frac{\partial U_K^{\mathcal{L}}}{\partial \rho_2} & \cdots & \frac{\partial U_K^{\mathcal{L}}}{\partial \rho_M} \end{pmatrix} \tag{4.11}$$

where j indicates the j'th voltage measurement and k indicates the k'th current pattern in the notation U_j^k and M is the number of the elements in the finite element mesh used in the inverse computations. .

When the zero columns and rows of the matrix $\frac{\partial A}{\partial \rho_m}$ are utilized the m'th column of the Jacobian can be obtained from

$$\frac{\partial U^h}{\partial \rho_m} = -\gamma(1:\mathcal{N},:)^T \frac{\partial B}{\partial \rho_m}\alpha \ , \tag{4.12}$$

where the notation $\gamma(1:\mathcal{N},:)$ refers to the part of the matrix γ that includes the first $\mathcal{N}$ rows and all columns.

From the equation (4.9) it can be seen that the matrix $\frac{\partial B}{\partial \rho_m}$ can be written of form

$$\frac{\partial B}{\partial \rho_m} = -\frac{1}{\rho_m^2}\begin{pmatrix} \int_\Omega \nabla\varphi_1 \cdot \nabla\varphi_1 \, dx\, dy & \cdots & \int_\Omega \nabla\varphi_1 \cdot \nabla\varphi_{\mathcal{N}} \, dx\, dy \\ \vdots & \ddots & \vdots \\ \int_\Omega \nabla\varphi_1 \cdot \nabla\varphi_{\mathcal{N}} \, dx\, dy & \cdots & \int_\Omega \nabla\varphi_{\mathcal{N}} \cdot \nabla\varphi_{\mathcal{N}} \, dx\, dy \end{pmatrix} \tag{4.13}$$

$$= -\frac{1}{\rho_m^2} B_{\text{grad}} \ , \tag{4.14}$$

where B_{grad} is the matrix which includes the integrals of the terms $\nabla\varphi_i \cdot \nabla\varphi_j$ over the element. As can be seen when iterative methods are used the matrix B_{grad} is needed to be computed only once, and this can be done in advance.

4.2 The Hessian in EIT

Let us consider the term

$$\frac{\partial^2 U}{\partial\rho_j \partial\rho_m} \tag{4.15}$$

in the Hessian matrix. By using the formulation of the m'th column of the Jacobian matrix it can be written

$$\begin{aligned}
\frac{\partial^2 U}{\partial\rho_j\partial\rho_m} &= \frac{\partial}{\partial\rho_j}\left(\frac{\partial U}{\partial\rho_m}\right) \\
&= -\frac{\partial}{\partial\rho_j}\left[\left(A^{-1}\tilde{M}^T\right)^T \frac{\partial A}{\partial\rho_m}\theta\right] \\
&= -\left[\frac{\partial\left(A^{-1}\tilde{M}^T\right)^T}{\partial\rho_j}\frac{\partial A}{\partial\rho_m}\theta + \left(A^{-1}\tilde{M}^T\right)^T\left(\frac{\partial^2 A}{\partial\rho_j\partial\rho_m}\theta + \frac{\partial A}{\partial\rho_m}\frac{\partial\theta}{\partial\rho_j}\right)\right] \\
&= -\tilde{M}\frac{\partial A^{-1}}{\partial\rho_j}\frac{\partial A}{\partial\rho_m}\theta - \left(A^{-1}\tilde{M}^T\right)^T\left(\frac{\partial^2 A}{\partial\rho_j\partial\rho_m} - \frac{\partial A}{\partial\rho_m}A^{-1}\frac{\partial A}{\partial\rho_j}\theta\right) \\
&= -\tilde{M}\left(-A^{-1}\frac{\partial A}{\partial\rho_j}A^{-1}\right)\frac{\partial A}{\partial\rho_m}\theta \\
&\quad + \left(A^{-1}\tilde{M}^T\right)^T\left(\frac{\partial A}{\partial\rho_m}A^{-1}\frac{\partial A}{\partial\rho_j}\theta - \frac{\partial^2 A}{\partial\rho_j\partial\rho_m}\right) \\
&= \left(A^{-1}\tilde{M}^T\right)^T\left[\left(\frac{\partial A}{\partial\rho_j}A^{-1}\frac{\partial A}{\partial\rho_m} + \frac{\partial A}{\partial\rho_m}A^{-1}\frac{\partial A}{\partial\rho_j}\right)\theta - \frac{\partial^2 A}{\partial\rho_j\partial\rho_m}\right] \\
&= \gamma^T\left[\left(\frac{\partial A}{\partial\rho_j}A^{-1}\frac{\partial A}{\partial\rho_m} + \frac{\partial A}{\partial\rho_m}A^{-1}\frac{\partial A}{\partial\rho_j}\right)\theta - \frac{\partial^2 A}{\partial\rho_j\partial\rho_m}\right] .
\end{aligned} \tag{4.16}$$

From the equations (4.8) and (4.9) it can be seen that

$$\frac{\partial A}{\partial\rho_j}A^{-1}\frac{\partial A}{\partial\rho_m} = \frac{\partial A}{\partial\rho_m}A^{-1}\frac{\partial A}{\partial\rho_j} \tag{4.17}$$

so it can be written

$$\frac{\partial^2 U}{\partial\rho_j\partial\rho_m} = 2\gamma^T\frac{\partial A}{\partial\rho_j}A^{-1}\frac{\partial A}{\partial\rho_m}\theta - \gamma^T\frac{\partial^2 A}{\partial\rho_j\partial\rho_m} . \tag{4.18}$$

In equation (4.18) the second derivatives $\frac{\partial^2 A}{\partial\rho_j\partial\rho_m}$ are of the form

$$\frac{\partial^2 A}{\partial\rho_j\partial\rho_m} = \frac{\partial}{\partial\rho_j}\left[\frac{\partial A}{\partial\rho_m}\right] = \frac{\partial}{\partial\rho_j}\begin{bmatrix}\frac{\partial B}{\partial\rho_m} & 0\\ 0 & 0\end{bmatrix} = \begin{bmatrix}\frac{\partial^2 B}{\partial\rho_j\partial\rho_m} & 0\\ 0 & 0\end{bmatrix} \tag{4.19}$$

where

$$\begin{aligned}\frac{\partial^2 B(i,j)}{\partial\rho_j\partial\rho_m} &= \frac{\partial}{\partial\rho_j}\left(-\frac{1}{\rho_m^2}\int_{\mathrm{supp}(\chi_m)}\nabla\varphi_i\cdot\nabla\varphi_j\,dx\,dy\,dz\right)\\ &= \begin{cases}\frac{2}{\rho_m^3}\int_{\mathrm{supp}(\chi_m)}\nabla\varphi_i\cdot\nabla\varphi_j\,dx\,dy\,dz & ,\ if\ \ j=m\\ 0 & ,\ if\ \ j\neq m.\end{cases}\end{aligned} \tag{4.20}$$

Now, the matrix $\frac{\partial^2 U}{\partial\rho_j\partial\rho_m}\in\mathbb{R}^{K\times\mathcal{L}}$ gives the components $G_i(j,m)$ of Hessians G_i corresponding to all the measurements U_i. Thus, the matrices $\frac{\partial^2 U}{\partial\rho_j\partial\rho_m}$ need to be computed corresponding to all combinations (j,m). Further, the Hessian $\nabla^2 F$ can be computed using equation (2.35), where $G_i^{(\mathrm{r})}=G_i$ as noticed above. Even if the Hessian G_i is symmetric, the computation takes a lot of computer time.

4.3 Block form for computing ∇F

Both in steepest descent method and in nonlinear conjugate gradient method a gradient of the minimized functional has to be computed. With the choice $W_1=I$ the equation (2.126) gets the following form in the case of EIT

$$\nabla F(\rho_k) = -J(\rho_k)^T(U_{\mathrm{meas}}-U(\rho_k,z_0))+\lambda^2 W_2(\rho_k-\rho^*) \tag{4.21}$$

$$= -J(\rho_k)^T b+\lambda^2 W_2(\rho_k-\rho^*)\ , \tag{4.22}$$

where $b=U_{\mathrm{meas}}-U(\rho_k,z_0)\in\mathbb{R}^{\mathcal{L}K\times 1}$. In practice the computation of the Jacobian matrix J takes a lot of computer time in large dimensional problems. In addition, in EIT the Jacobian matrix is also full. Multiplication of the large dimensional and full matrix and vector b is also toilsome problem. Let us consider an approach to steepest descent method in which the Jacobian matrix is not computed completely and the multiplication J^Tb is done for one current injection at a time.

Consider the vector $J^Tb\in\mathbb{R}^{\mathcal{N}\times 1}$, which can be written in the form

$$J^Tb=\begin{pmatrix}\sum_{i=1}^{\mathcal{L}K}J(i,1)b_i\\ \vdots\\ \sum_{i=1}^{\mathcal{L}K}J(i,\mathcal{N})b_i\end{pmatrix}\ , \tag{4.23}$$

where the notation b_i refers to the i'th index of the vector b and $J(i,m)$ $m=1,...,\mathcal{N}$ refers to the index of the matrix J in i'th row and m'th column. For each index of the vector J^Tb one column of the Jacobian matrix is needed. Let us consider the m'th index of J^Tb. If the vector b is reshaped such that $b^h\in\mathbb{R}^{K\times\mathcal{L}}$ and each column corresponds measurements with one current pattern as in (3.54)

it can be seen that

$$\sum_{i=1}^{\mathcal{L}K} J(i,m)b_i = \sum_{j=1}^{\mathcal{L}} J\left((j-1)K+1:jK,m\right)^T b_j^h \tag{4.24}$$

$$= \sum_{j=1}^{\mathcal{L}} \left(-\gamma(1:\mathcal{N},:)^T \frac{\partial B}{\partial \rho_m}\alpha_j\right)^T b_j^h \tag{4.25}$$

$$= -\sum_{j=1}^{\mathcal{L}} \left[\left(\underbrace{\gamma(1:\mathcal{N},:)b_j^h}_{=:\Gamma_j}\right)^T \frac{\partial B}{\partial \rho_m}\alpha_j\right]^T \tag{4.26}$$

$$= -\sum_{j=1}^{\mathcal{L}} \Gamma_j^T \frac{\partial B}{\partial \rho_m}\alpha_j \in \mathbb{R}\,, \tag{4.27}$$

where the notation $J\left((j-1)K+1:jK,m\right)$ refers to the part of the Jacobian that includes the rows which corresponds to the j'th current pattern and m'th column, b_j^h refers to the column of b^h that corresponds to the j'th current pattern and α_j refers to the column of α that corresponds to the j'th current pattern. Each term in summation (4.27) can be computed in parallel. The same procedure is carried out for each column of the Jacobian (ρ_m) to obtain all the terms of the vector $J^T b$.

4.4 Alternative formulation for the Levenberg-Marquardt method

When Gauss-Newton and Levenberg-Marquardt methods are used in EIT the large dimensional matrix $J^T J \in \mathbb{R}^{\mathcal{N}\times\mathcal{N}}$, where $\mathcal{N}$ is number of the parameters has to be inverted. There is another formulation for the Levenberg-Marquardt method in which the inverted matrix is of form $J\,J^T$.The dimension of the matrix $J\,J^T \in \mathbb{R}^{\mathcal{L}K\times\mathcal{L}K}$, where $\mathcal{L}$ is number of the current patterns and K is number of the measurements, is in many realistic 3D EIT problems considerably smaller than the dimensions of the matrix $J^T J$.

Let us consider the search direction p_k in Levenberg-Marquardt method

$$p_k = (J_k^T J_k + \lambda_k I)^{-1} J_k^T (U_{\text{meas}} - U(\rho_k, z_0))\,, \tag{4.28}$$

where $J_k = J(\rho_k)$. Using the matrix inversion lemma (if $B = XRY + A$ then $B^{-1} = A^{-1} - A^{-1}X(R^{-1} + YA^{-1}X)^{-1}YA^{-1}$) the equation (4.28) can be written

in the form

$$\begin{aligned} p_k &= \left(\lambda_k^{-1} I - \lambda_k^{-1} J_k^T (I + J_k \lambda_k^{-1} J_k^T)^{-1} J_k \lambda_k^{-1} I\right) J_k^T (U_{\text{meas}} - U(\rho_k, z_0)) \\ &= \left(\lambda_k^{-1} I - \lambda_k^{-1} J_k^T (\lambda_k^{-1}(\lambda_k I + J_k J_k^T))^{-1} J_k \lambda_k^{-1} I\right) J_k^T (U_{\text{meas}} - U(\rho_k, z_0)) \\ &= \left(\lambda_k^{-1} J_k^T - \lambda_k^{-1} J_k^T (J_k J_k^T + \lambda_k I)^{-1} J_k J_k^T\right) (U_{\text{meas}} - U(\rho_k, z_0)) \\ &= \left(\lambda_k^{-1} J_k^T (J_k J_k^T + \lambda_k I)^{-1} (J_k J_k^T + \lambda_k I) - \lambda_k^{-1} J_k^T (J_k J_k^T + \lambda_k I)^{-1} J_k J_k^T\right) \\ &\quad \cdot (U_{\text{meas}} - U(\rho_k, z_0)) \\ &= \lambda_k^{-1} J_k^T (J_k J_k^T + \lambda_k I)^{-1} \left(J_k J_k^T + \lambda_k I - J_k J_k^T\right) (U_{\text{meas}} - U(\rho_k, z_0)) \\ &= J_k^T (J_k J_k^T + \lambda_k I)^{-1} (U_{\text{meas}} - U(\rho_k, z_0)) \end{aligned} \tag{4.29}$$

The matrix inversion lemma can be used also in other regularizations in order to be obtain new formulations for the algorithms.

4.5 Kaczmarz -method

There are also other methods that avoid the expense of inverting $J^T J$ but has faster convergence than the gradient based methods [3, 73]. When each iteration step is obtained from the equation

$$\rho_{k+1} = \rho_k + \alpha_k J_k^T W_k (U_{\text{meas}} - U(\rho_k, z_0)) \tag{4.30}$$

the method is called as filtered back propagation and W_k can be any positive definite operator. The step parameter α_k is fixed in ordinary filtered back propagation. However, the step parameter can be chosen by inexact line search, as explained in 2.1.1. If W_k is chosen to be

$$W_k = (J_k J_k^T)^{-1} \tag{4.31}$$

each iteration step is of form

$$\rho_{k+1} = \rho_k + \alpha_k J_k^T (J_k J_k^T)^{-1} (U_{\text{meas}} - U(\rho_k, z_0)) \ . \tag{4.32}$$

In EIT problem the Jacobian is ill-conditioned and therefore the regularization is needed. One way to regularize the filtered back propagation method is to modify the matrix W_k so that [3]

$$\rho_{k+1} = \rho_k + \alpha_k J_k^T (J_k J_k^T + \lambda I)^{-1} (U_{\text{meas}} - U(\rho_k, z_0)) \ . \tag{4.33}$$

It can be seen that the modified version of the filtered back propagation method (4.33) is of the form of Levenberg-Marquardt algorithm (4.29). The only difference is that in Levenberg-Marquardt method the weight coefficient λ is chosen in each iteration step k. Even though inverse of the matrix $J_k J_k^T$ is not as hard to compute as inverse of the matrix $J_k^T J_k$ it takes a lot of computer time and storage. In Kaczmarz method the matrix W_k is replaced with a simpler expression

$$W_k = \begin{pmatrix} (J_{k,1} J_{k,1}^T)^{-1} & 0 & \dots & 0 \\ 0 & (J_{k,2} J_{k,2}^T)^{-1} & \dots & 0 \\ \vdots & \vdots & \ddots & \vdots \\ 0 & 0 & \dots & (J_{k,\mathcal{L}} J_{k,\mathcal{L}}^T)^{-1} \end{pmatrix} , \tag{4.34}$$

where $J_{k,j}$ indicates the block of the Jacobian witch corresponds the j'th current pattern in k'th iteration step [74]. The iteration is done for each current pattern separately. Disadvantage of the method is that the forward problem has to be computed frequently for updating ρ_k

4.6 Extended Kalman filter

In the case that the resistivity distribution changes during the measurements the inverse problem of EIT can be considered as a state estimation problem [102, 50]. The state estimation approach is based on so-called state-space representation

$$\rho_{t+1} = F_t\rho_t + w_t \ , \tag{4.35}$$

$$U_{\text{meas},t} = U(\rho_t) + v_t \ , \tag{4.36}$$

where t is the time index, $\rho_t \in \mathbb{R}^M$ is the resistivity distribution at time t, M is the number of the elements in the finite element mesh used in the inverse computations. The equation (4.35) is called the state equation, and it describes the time-dependence of the resistivity distribution. The matrix F_t is called the state transition matrix. Further, $U_{\text{meas},t}$ is the vector containing the voltage measurements corresponding to current pattern that was applied at time t. This means that the voltages are measured in parallel such that all measurements corresponding to a single current pattern are made simultaneously. The vector v_t represents the measurement errors and w_t is called the state noise process. The equation (4.35) is called the state evolution equation and equation (4.36) the observation equation.

The state estimation problem is to compute the expectation

$$\rho_{t|k} = E\{\rho_t|U_{\text{meas},1}, ..., U_{\text{meas},k}\} \ . \tag{4.37}$$

The only computationally feasible approach to solve the state estimation problem is to use recursive algorithms. In linear case the most common algorithms are called *Kalman recursions*. The task is to compute the optimal estimator for each ρ_t based on measurements $U_{\text{meas},k}$, $k \in \mathcal{I}(t)$, where $\mathcal{I}(t)$ denotes a subset of available measurements that are used to compute the estimates. The most common recursive estimators of the state ρ_t are called the Kalman predictor $\rho_{t|t-1}$ and Kalman filter $\rho_{t|t}$. For general discussion of the state estimation problem, see e.g. [1].

In nonlinear case the expectation cannot be written in recursive form. This leads to the tedious computation which can be done for example with Monte Carlo methods. However, suboptimal algorithms exist, for example extended Kalman filter, which is of the form

$$G_t = C_{\tilde{\rho}_{t|t-1}} J_t^T (J_t C_{\tilde{\rho}_{t|t-1}} J_t^T + C_{v_t})^{-1} \tag{4.38}$$

$$C_{\tilde{\rho}_{t|t}} = (I - G_t J_t) C_{\tilde{\rho}_{t|t-1}} \tag{4.39}$$

$$\rho_{t|t} = \rho_{t|t-1} + G_t(U_{\text{meas},t} - U(\rho_{t|t-1})) \tag{4.40}$$

$$C_{\tilde{\rho}_{t+1|t}} = F_t C_{\tilde{\rho}_{t|t}} F_t^T + C_{w_t} \tag{4.41}$$

$$\rho_{t+1|t} = F_t \rho_{t|t} \tag{4.42}$$

where C_{v_t} is the observation noise covariance matrix, C_{w_t} is the state noise covariance matrix, $C_{\tilde{\rho}_{t|t-1}}$ is the covariance of the estimation error $\tilde{\rho}_{t|t-1} = \rho_t - \rho_{t|t-1}$, $U(\rho_{t|t-1})$ is the calculated voltages and $J_t = J(\rho_{t|t-1})$ part of the Jacobian matrix. In stationary case there is no evolution of the resistivity distribution and the trivial choice $F_t \equiv I$, where I the identity matrix (the random walk model) is relevant. Also the state noise covariance matrix equals zero but for the computational reasons it is chosen to be $C_{w_t} = a_1 I$ in which a_1 is some small constant. EIT inverse problem is ill-posed and therefore the regularization is needed. The spatial regularization can be appended to the observation equation (4.36) using the same strategy as in equation (2.100) corresponding to Tikhonov regularization in stationay case. The state space representation of the dynamic (time-varying) EIT problem, its solution with the Kalman filter and the associated spatial regularization have been proposed earlier in [102, 50, 46, 107, 106] for 2D cases.

4.7 Regularization matrix

In this study the regularization matrix L_2

$$L_2 = \begin{bmatrix} \alpha_1 L_h \\ \alpha_2 L_v \end{bmatrix} . \tag{4.43}$$

has been used. The matrices L_h and L_v approximate the directional derivatives in the (x, y) plane and in the z direction, respectively. The parameters α_1 and α_2 are the regularization parameters. In L_h we take into account ten nearest elements in the horizontal plane and in L_v two nearest elements from the vertical direction, except on the bottom and on the top of the discretized image, where we take into account only one nearest element. The chosen elements are weighted by the inverse of the distances between the centers of the elements. Because the matrix L_2 is of difference type, the prior assumption that the solution is smooth is used. More accurate priors can be used but quite often they lead to tedious computations [56].

The regularization parameters α_1 and α_2 have to be chosen based on some criteria. Because the regularization parameter is connected to a priori assumptions about the solution it should be chosen in a way that these prior assumptions are taken into account [101]. In practice, the less noise the smaller parameter can be used. In this thesis the regularization parameters were adjusted *a posteriori* by visual examination.

4.8 Difference imaging

In difference imaging two different data sets are needed and the reconstruction is based on voltage difference δU between these measurements. Because one is interested in only the resistivity changes $\delta\rho$ and the difference $\delta\rho$ is assumed to be small, it is adequate to solve only a linearized version of the problem. When the Tikhonov regularization is used the solution can be obtained from the equation

$$\delta\rho = (J^T J + L_2^T L_2)^{-1} (J^T \delta U) . \tag{4.44}$$

4.9 Starting point for iteration

In static imaging the reference data is not available as in the case of difference imaging. Thus even in the case of one-step reconstruction the voltages corresponding to the linearization distribution ρ_0 are needed to be calculated with great accuracy [103, 109]. If the original nonlinear problem is to be solved, the voltages have to be computed in each iteration step. In this study iterative methods such as Gauss-Newton, Steepest descent, Conjugate gradient, Kaczmarz and Extended Kalman filter have been used for the static reconstructions. In each method the initial guess ρ_0 for the resistivity distribution has to be determined. In this study a homogeneous estimate for the resistivity distribution has been used as ρ_0. The best homogeneous resistivity distribution can be computed in the following way. It has been shown in [43] that for any homogeneous distribution $\rho(x) \equiv \tilde{\rho} \in \mathbb{R}$ the voltages can be computed in the form

$$U(\rho, z_0) = \tilde{\rho} U(1, \tau) \tag{4.45}$$

where $\tau = \frac{1}{\tilde{\rho}} z_0$ and $z_0 \in \mathbb{R}^L$ includes the contact impedances. If τ is fixed to some value, corresponding to a prior guess for $\tilde{\rho}$, the best homogeneous resistivity distribution ρ_{best} that minimizes the functional

$$\|U_{\text{meas}} - \rho U(1, \tau)\|_2^2 \tag{4.46}$$

can be solved using LS-estimation as described in Section 2.2 when observation model $H = U(1, \tau)$ and $\theta = \rho$. The solution is

$$\rho_{\text{best}} = (H^T H)^{-1} H^T U_{\text{meas}} \tag{4.47}$$

from which the reference voltages for the first iteration step can be computed as

$$U(\rho_0, z_0) = H \rho_{\text{best}} \tag{4.48}$$

Similar ideas in 2D have also been used in [57].

CHAPTER V

Numerical studies

In this chapter two numerical simulations with different geometries are presented. In section 5.1 results of comparison between different iterative reconstruction methods are shown. Cylindrical tank geometry is used in this study. In section 5.2 the model truncation problem is studied with infinite elements in long pipe geometry.

5.1 Comparison of iterative reconstruction methods

The proposed approaches were evaluated with a numerical simulation. When comparing different methods, it is important to notice that when the minimized functional is fixed (fixed prior), different iterative methods should converge to the same solution. Indeed, the solution obtained with Gauss-Newton, conjugate gradient and steepest descent method are equal in this study. The aim of this study is thus not to compare the quality of the reconstructions. Instead, the main interest in this study is to compare the efficiency and the computer storage in different methods. However, some of the compared methods, such as Kaczmarz and Extended Kalman filter iterations, do not converge to the same solution due to different priors associated with those methods.

5.1.1 Simulated measurements

As a numerical test phantom a cylindrical tank with 48 electrodes, 16 electrodes in three planes was used, see Fig. 5.1. The radius of the tank was 15 cm and height was 20 cm. To study the efficiency of the different reconstruction methods, a simulated resistivity distribution shown in Fig. 5.2 was used. In the sequel this distribution is referred to as *true distribution*. The simulated data was computed in a mesh of 6180 tetrahedral elements and 1434 nodes and the resistivity distribution was represented in piecewise linear basis. The tetrahedral elements formed five layers, height of each layer being 4 cm. The cut surfaces in Fig. 5.2 are taken from the middle of each layer. As the figure indicates, there were two inhomogeneities inside the cylinder, differing from the constant background resistivity of 300 Ωcm.

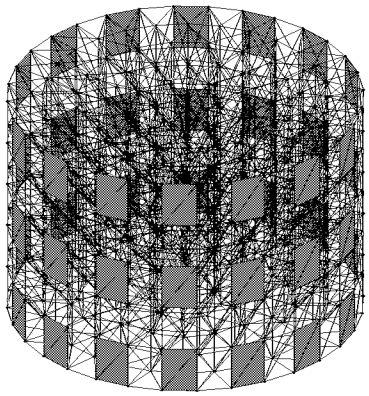

Figure 5.1: An example of the finite element mesh used in the calculations. The red-faced elements are located under the electrodes.

The resistivity of the lower inhomogeneity was 100 Ωcm in the first element layer from the bottom, increasing linearly to the background value 300 Ωcm inside the second layer. The resistivity of the upper inhomogeneity was 500 Ωcm in two uppermost element layers, decreasing linearly to the background value 300 Ωcm inside the third layer.

There are numerous possibilities to inject current and measure voltages in three dimensions. The quality of the images depends on the data collection strategy [15, 64, 48, 49]. The more independent data is obtained, the better the spatial resolution can be. In this study, only in-plane current injection and voltage measurements between adjacent in-plane electrodes have been used. For each current injection the voltages were measured on the remaining pairs of electrodes from each electrode plane. The voltage measurements from the current carrying electrodes were not used in the reconstructions and therefore 2160 voltage measurements were obtained. The reason for neglecting the voltages corresponding to the current carrying electrodes is that improper knowledge of the contact impedances in the real case may cause high errors in modeling those measurements [33].

Voltage observations were computed by applying the FEM to 3D complete electrode model. Since the resistivity is now represented in linear basis, the computation of the integrals in FEM scheme slightly differs from the computation in the case of constant basis in Section 3.2. However, the modification is straightforward.

Zero-mean Gaussian observation noise was added to the computed voltages. The observation noise consisted of two parts. The standard deviation (std) of the first part was 0.01% of the maximum voltage. The second part was inhomogeneous white noise, each component of the noise vector having std 1% of the value of the

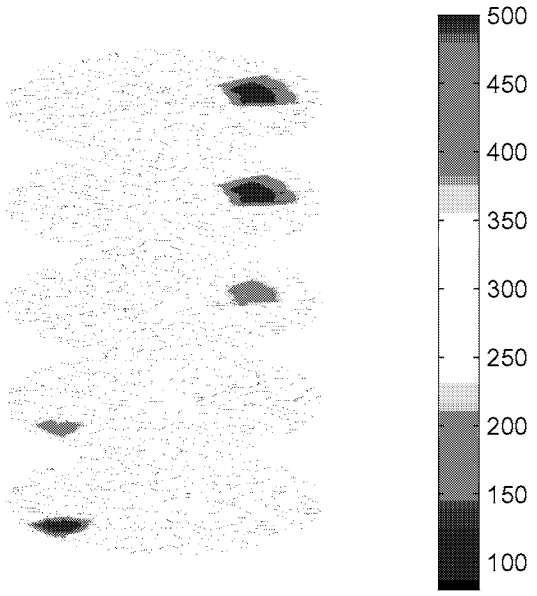

Figure 5.2: True resistivity distribution.

corresponding observation.

In the inverse computations 2060 parameters such that one parameter corresponds the union of three tetrahedral elements (wedge element) and the first order FEM basis have been used. The voltages $U(\rho, z_0)$ in static imaging were computed with the first order FEM basis in mesh of 6180 tetrahedral elements and 1434 nodes and the resistivity distribution was presented in piecewise constant basis.

5.1.2 Iterative reconstructions

GAUSS-NEWTON RECONSTRUCTION

Gauss-Newton reconstruction was computed using the algorithm (2.124). The Jacobian matrix J was constructed using the adjoint differentiation explained in Section 4.1. The best homogeneous estimate for the resistivity distribution (see Section 4.9) was used as both the initial guess ρ_0 and the prior distribution ρ^*. The weighting matrix W_1 was chosen to be an identity matrix I, and the regularization matrix L_2 corresponding to smoothness prior was constructed as explained in Section 4.7.

Inexact line search was used with Gauss-Newton algorithm. As mentioned in Section 2.1.1, in cases when functionals to be minimized are quadratic, an effective way to choose the step parameter α_k is to compute the value of the functional (4.1) with few different choices of α_k and then find the optimal α_k by fitting a quadratic

function to the computed values. Acceptable range for the step parameter was chosen so that negative values for the resistivities were not allowed. Quadratic function was fitted to four points that were chosen adaptively inside the range of acceptable step parameters.

Gauss-Newton algorithm converged in ten iteration steps. The final iterate is visualized in Fig. 5.3. The absolute values of the inhomogeneities are well recovered. In Fig. 5.3 also one step reconstruction is visualized. Inhomogeneities are already located well by using one step reconstruction but resistivity values are far from the real values especially in case of the inhomogeneity with the resistivity 500Ωcm. When choosing the weight of the regularization, compromise between accuracy of the absolute values and the level of image noise was made. Naturally, when the weight of the regularization corresponding to smoothness is high, the reconstructions are smooth, and the values of the inhomogeneities are close to background resistivity. On the other hand, use of too weak regularization results in noisy images. In this study the regularization parameter was adjusted by visual examination, because the traditional methods for choosing the regularization parameter are not suitable in the case of EIT. It is worth to notice, however, that in the real case the use of visual examination is not possible, since the true resistivity distribution is unknown. The question of choosing the regularization parameters in different types of inverse problems is a topic of on-going research. The aim of this study is not to consider this topic. Instead, the aim is to compare the efficiency and computational storage of different optimization methods applied to minimization problems with predetermined priors.

Nonlinear conjugate gradient reconstruction

Nonlinear conjugate gradient reconstruction was computed using the Algorithm 3 in Section 2.4.3. Scalar β_{k+1} was chosen as in Polak-Ribière method. Gradient of the minimized functional was computed in block form explained in Section 4.3. The functional to be minimized was the same as in Gauss-Newton reconstruction.

Nonlinear conjugate gradient algorithm converged in 260 iteration steps when inexact line search was used. The step parameter was chosen in the same way as in case of Gauss-Newton method. As expected, the iteration converged to the same solution as in the case of Gauss-Newton method. The final iterate is visualized in Fig. 5.4. The estimate after 30 iterations is also shown in Fig. 5.4. Inhomogeneities in this iterate are already located well but the resistivity values are still far from the real values. The restarting explained in Section 2.4.3 was tested but it did not increase the convergence rate substantially.

Steepest descent reconstruction

Steepest descent reconstruction was computed using the algorithm (2.11). Gradient of the minimized functional was computed in block form as in the case of conjugate gradient method. The functional to be minimized was the same as in Gauss-Newton reconstruction. Convergence rate of the steepest descent method is slow even when the inexact line search for choosing the step parameter described

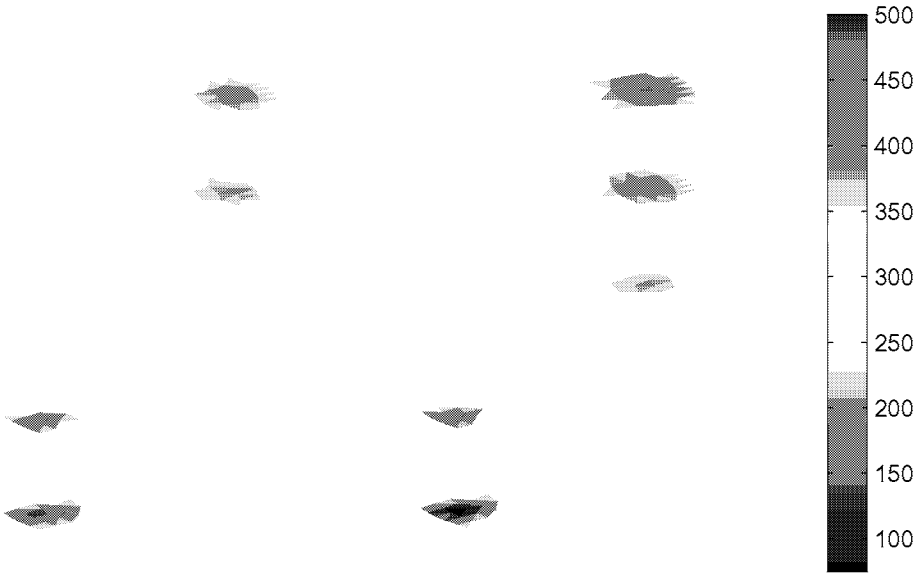

Figure 5.3: Gauss-Newton reconstruction after the first iteration step (left) and 10 iteration steps (right)

earlier was used. After 4 000 steps the iteration was not converged yet. However, the iterate was already close to the final iterates of Gauss-Newton and Conjugate gradient algorithms. The iterate after 4 000 steps is visualized in Fig. 5.5.

KACZMARZ RECONSTRUCTION

The functional to be minimized in Kaczmarz method is

$$F(\rho) = \|U_{\text{meas}} - U(\rho, z_0)\|_2^2 \tag{5.1}$$

Kaczmarz reconstruction was computed using the algorithm (4.33). Jacobian matrix J was computed for each current pattern separately as in case of conjugate gradient method and steepest descent method. Inexact line search was performed after each current pattern. Because the functional (5.1) does not include any prior information for the resistivity distribution, the solution is unstable. The solution is thus stabilized by cutting the iteration after chosen number of iteration steps. Fig. 5.6 represents the iterates after 53 steps and 3 steps. Here the number of iteration steps refers to the number of the repetitions of the iteration (4.33) corresponding to all current injections. The order of the injections in the iteration (4.33) was chosen randomly. This procedure improves the performance of the iteration because, loosely speaking, the sensitivity of the measurements covers the domain more rapidly.

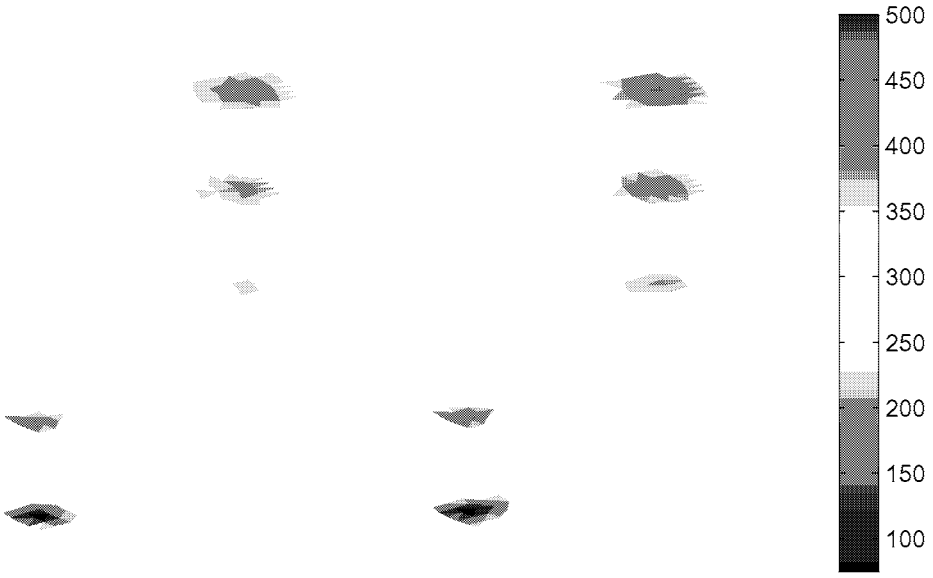

Figure 5.4: Conjugate gradient reconstructions after 30 iteration steps (left) and 260 iteration steps (right).

Extended Kalman filter reconstruction

Extended Kalman filter reconstruction was computed using the equations (4.38–4.42). Since extended Kalman filter was applied to the stationary case the evolution matrix was chosen to be $F_t \equiv I$. The state noise covariance matrix $C_{w_t} = \sigma_w^2 I$ where σ_w was 0.01% of the best homogeneous estimate ρ_0 for resistivity distribution. This implies that the recursion allows small changes in resistivity distributions between consecutive current injections. The covariance of the initial state was $C_{\tilde{\rho}_{0|0}} = \sigma_0^2 I$ where σ_0 was 2% of ρ_0. The observation noise covariance matrix was $C_{v_t} = \sigma_v^2 I$ where the σ_v was 0.01% of the maximum voltage.

Spatial regularization was included in the iteration as explained in Section 4.6. The spatial prior was the same as in Gauss-Newton, conjugate gradient and steepest descent methods. The drawback of using spatial regularization with extended Kalman filter is that the storage needs and the computation time increase considerably.

The iteration (4.38–4.42) was repeated five times. The reconstructions were also computed by using mixed order for the current patterns, as in the case of Kaczmarz iteration. The estimates after five iterations both with and without mixing the order of injections are shown in Fig. 5.7. When order of injections was mixed the reconstruction was improved.

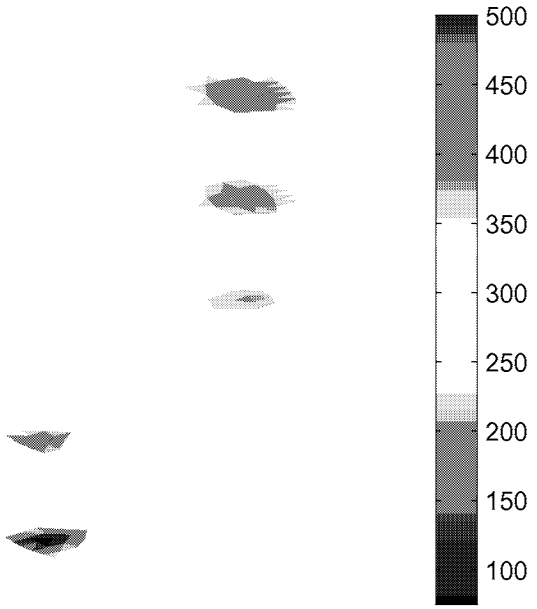

Figure 5.5: Steepest descent reconstruction.

5.1.3 Discussion of the results

In Table 5.1 the comparison between the proposed approaches is shown. The quality of different estimates have been evaluated by computing the error norm defined as

$$e = \frac{1}{V} \int_{\Omega} (\rho - \hat{\rho}) \, \mathrm{d}x \tag{5.2}$$

where ρ is the true distribution, $\hat{\rho}$ is the estimate and V is the volume of Ω. When comparing different methods, note that only in Gauss-Newton, Conjugate gradient and Steepest descent reconstructions the functional to be minimized is same. As assumed, the solutions obtained with these methods are same. The convergence rate of the Gauss-Newton method is the best (Fig. 5.8) but it requires memory storage far more than the other methods. Inexact line search has remarkable impact for convergence rate in the cases of the conjugate gradient (Fig. 5.9) and steepest descent methods, whereas in Gauss-Newton method it did not affect the convergence rate significantly (Fig. 5.10). As Fig. 5.9 indicates, in the beginning of the iteration the optimal values of the step parameter $\alpha_k >> 1$.

In this test case the Gauss-Newton iteration required shortest time for convergence. However, the memory demand in Gauss-Newton method was five times bigger than in the cases of Conjugate gradient and Steepest descent methods. The cases in which the computer storage is limited, and Gauss-Newton method cannot be used, the Conjugate gradient method is preferable to Steepest descent

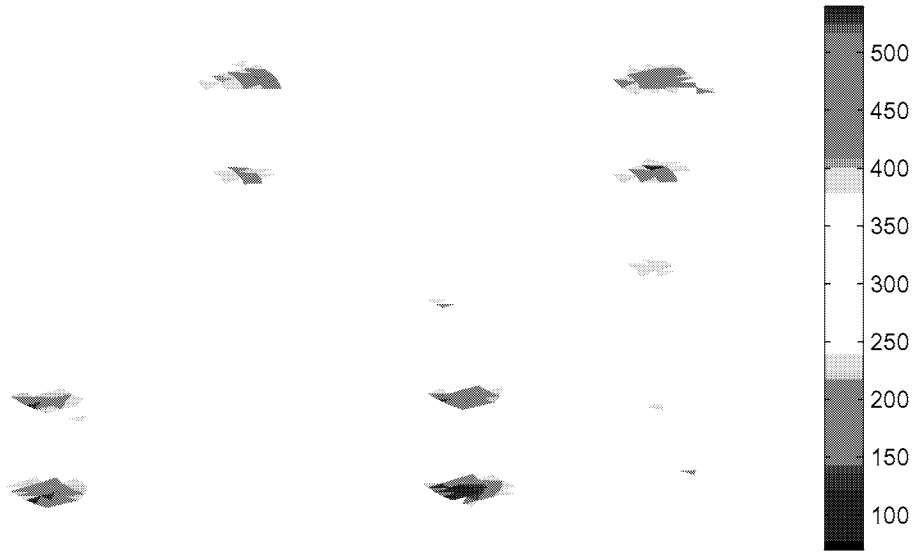

Figure 5.6: Kaczmarz reconstructions. Left: reconstruction after 3 iteration steps Right: reconstruction after 53 iteration steps.

method, because of significantly shorter computational time. Furthermore, if one is satisfied with qualitative images, not necessarily absolute values, the Gauss-Newton and Conjugate gradient methods already give feasible solutions after a few iterations.

Kaczmarz and Extended Kalman filter iterations do not converge to the same solution due to different priors associated. As mentioned above, the memory need for Extended Kalman filter with spatial regularization is huge. Changing the order of current injections improved the quality of the estimate considerably. The memory need of the Kaczmarz iteration is smallest. However, the problem in Kaczmarz method arises from the instability of the solution. In order to get feasible solutions one should know when to stop the iteration.

In this study it was observed that the convergence of the resistivity value of 100Ωcm was faster than that of the resistivity value of 500Ωcm. This can be clearly seen in Fig. 5.11 for the three different methods for the maximum and minimum resistivity values of the reconstructions. The final values of the maximum and minimum resistivities depend a lot on the prior used. This feature can be explained by investigating the sensitivity of the measurements to different types of changes in resistivity distribution. For this purpose a following test was performed. Multiple targets with equal sized cylindrical inhomogeneities with varying resistivities were constructed. The EIT observations were calculated for different targets. Fig. 5.12 represents the norm of the difference ϵ between the voltages corresponding to a

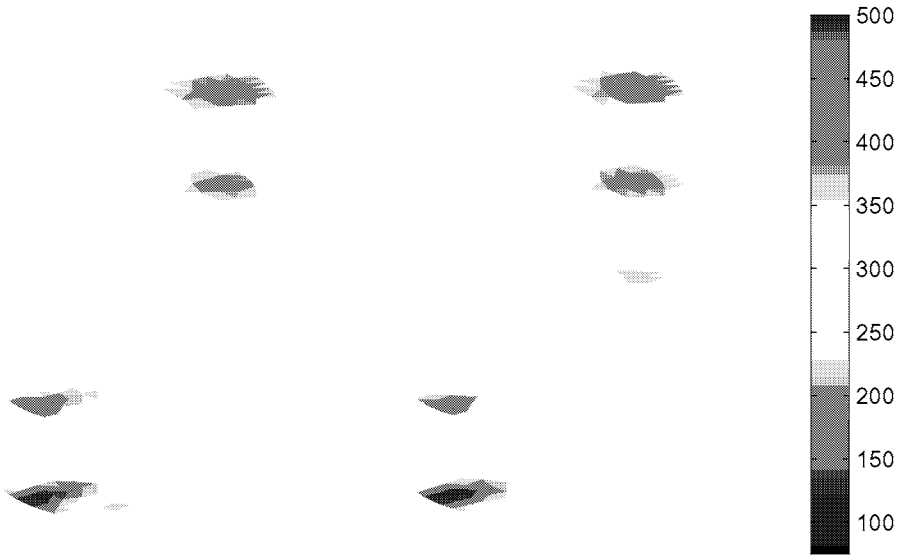

Figure 5.7: Extended Kalman filter reconstructions. The estimates after five iterations without (left) and with (right) mixing the order of injections.

Table 5.1: Comparison of different optimization methods. The error norm e is defined in equation (5.2), $F = F(\hat{\rho})$ is the minimized functional, and the memory need is expressed in Megabytes. CG is abbreviation for conjugate gradient.

Method	Iteration steps	e	$F(\cdot 10^{-7})$	Memory need
Gauss-Newton	10	10.3296	1.5704	41.3230
Nonlinear CG	260	10.3170	1.5704	8.1984
- restarting c=0.3	247	10.3169	1.5704	8.1984
Steepest descent	4 000	9.8946	1.5722	8.1654
Kaczmarz	3	11.1960	0.1760	7.2177
	53	15.0810	0.1280	7.2177
Extended Kalman filter	5	13.2600	5.4685	144.8100
- changed order	5	10.6812	2.9110	144.8100

homogeneous distribution and the voltages corresponding to targets with inhomogeneities with different resistivities. The background resistivity in the target cases and the homogeneous distribution were 300Ωcm. Obviously negative changes

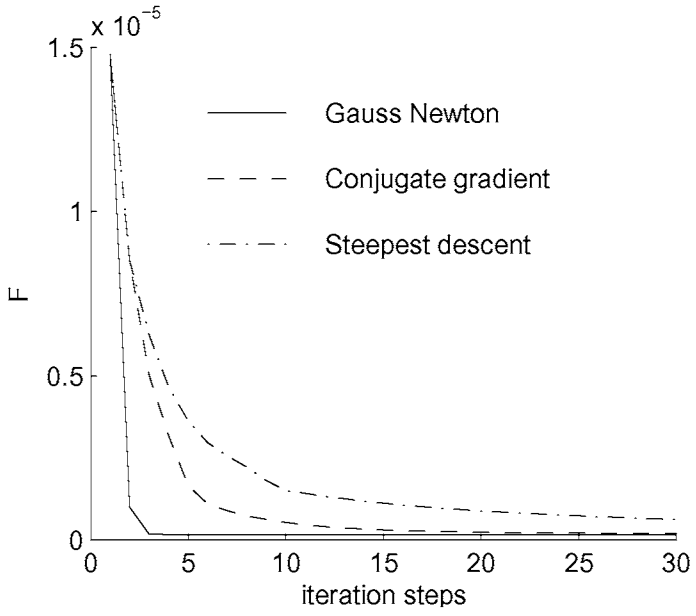

Figure 5.8: Comparison of the convergence rates. Value of functional $F(\rho)$ in first 30 iteration steps for different optimization methods.

in resistivity of inhomogeneity cause remarkably bigger changes in voltage observations. That is the measurements are more sensitive for negative changes in resistivity. Thus, in this case the problem of finding resistive inhomogeneities is more ill-posed than the problem of finding conductive inhomogeneities. For this reason the prior has more impact on the resistive target than on the conductive one in our example case.

5.2 Infinite elements

5.2.1 Effect of the model truncation

In a real 3D situation the whole domain to be imaged, e.g. a human body, should be discretized for the computations. However, far from the current carrying electrodes the voltages and the currents are diminished so much that the model can be truncated. Now the question is, how does the model truncation effect on the image reconstruction and how far from the current carrying electrodes should the domain be discretized.

In 3D EIT, when the model is truncated the boundary condition that the component of the current density in normal direction (Neumann) is zero on the boundary is normally used. However, as it can be seen e.g. from the Fig. 5.14 a)

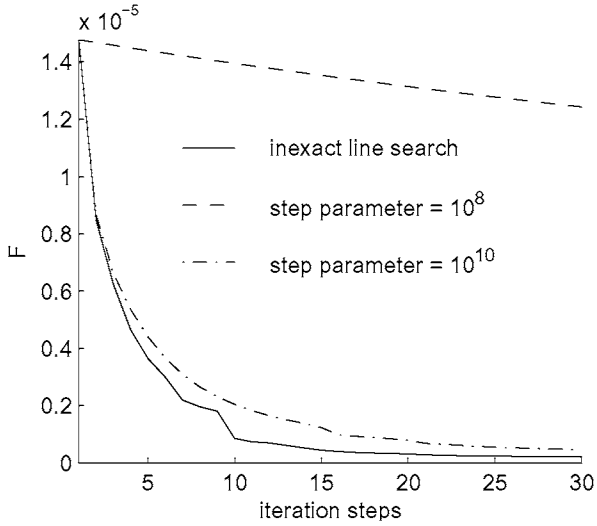

Figure 5.9: Convergence of the Conjugate gradient iteration with inexact line search and with two fixed step parameters.

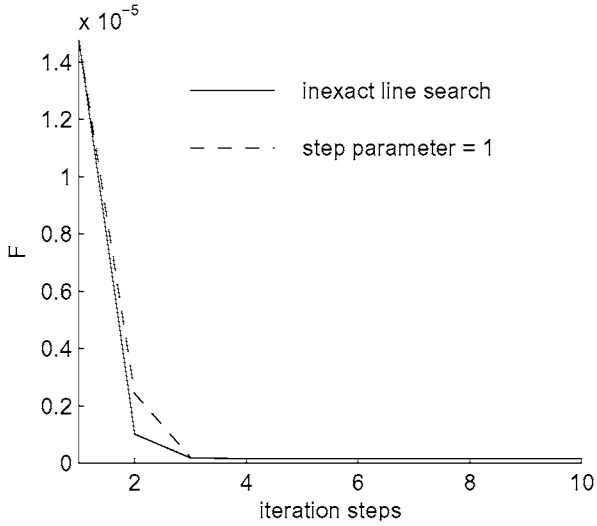

Figure 5.10: Convergence of the Gauss-Newton iteration with inexact line search and with standard choice $\alpha_k = 1$.

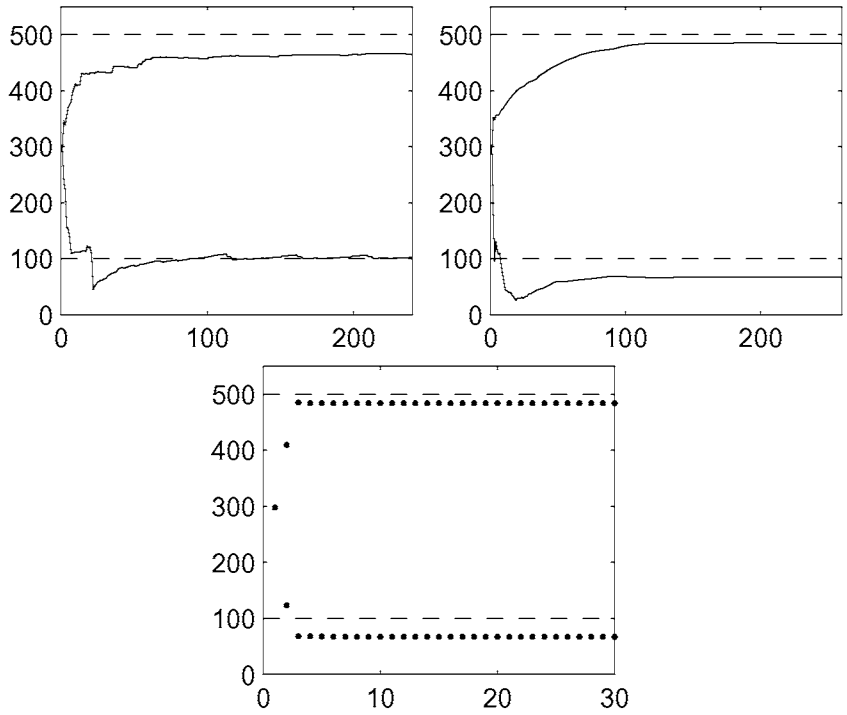

Figure 5.11: Convergences of the maximum and minimum resistivity values of the reconstructions during the iterations. Above left: extended Kalman filter method, above right: conjugate gradient method, below: Gauss-Newton method. The dashed lines mark the true minimum and maximum values.

the voltage gradient in z-direction is not zero until after 50 cm from the current carrying electrodes when the whole domain (a cylinder) is 100 cm high. This means that there is current flow in the vertical, z-direction, and the homogeneous Neumann boundary condition is not valid. The voltages in Fig. 5.14 were computed for homogenous target.

Before studying effects of the model truncation on the reconstructed images, the sensitivities with respect to the distance from the electrode planes were studied. Here target is still assumed to be homogeneous.

First the norms of the columns of the Jacobian J (sensitivities) were compared in order to see how far from the electrode planes is the level in which all the norms of J are smaller than the minimum norm ("smallest sensitivity") in the region of interest. The region of interest was assumed to include the domain from the bottom to 14 cm, see Fig. 5.16, when the whole domain was 32 cm in z-direction. The result is shown plotted in Fig. 5.13. It tells that in this case the level is at 24 cm from the bottom of the cylinder (12 cm above the uppermost electrode plane)

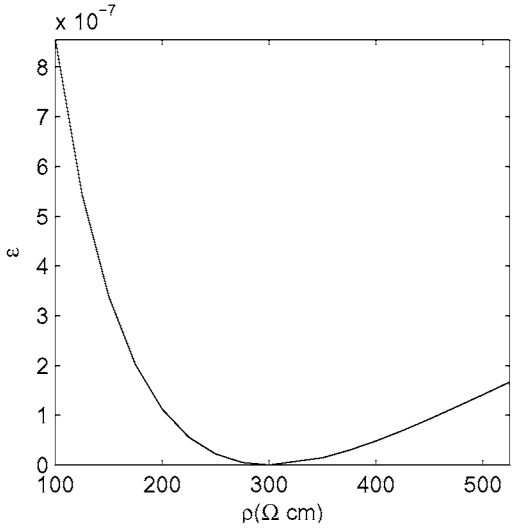

Figure 5.12: Norm of the difference ϵ between the voltages corresponding to a homogeneous target and the targets with inhomogeneity having resistivity ρ

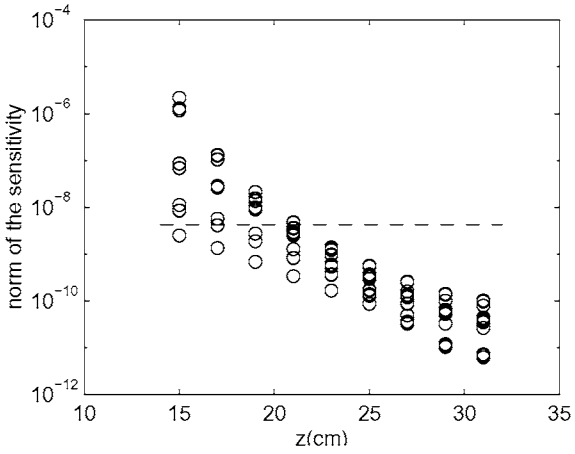

Figure 5.13: The norms of the columns of the Jacobian out of the region of interest in different heights of the cylinder (plotted with 'o'). Each column of o's correspond to one element layer in the mesh, i.e., all the elements have the same height in z-direction. Also shown is the minimum column norm of the Jacobian from the region of interest, plotted with dashed line (- -).

where all the sensitivities are smaller than the smallest one in the region of interest. There are quite large differences between the sensitivities on each layer (columns of o's in the Fig. 5.13). This is clear since the elements near the boundary of the cylinder have bigger sensitivity than the elements near the center. Similar results to these shown here were obtained from the cylindrical phantom studies, see [83].

The effect of the model truncation is clearly seen in Fig. 5.14. In Fig. 5.14 a) the first current injection from the first electrode plane was used. The different model truncation situations (different heights of the cylindrical mesh) were tested and the corresponding voltages compared to the voltages of the "true" situation in which the height of the cylinder was 100 cm. As the model is truncated at $z = 32$ cm, the difference in the voltages is not enormously large. As the voltages are computed in a smaller cylinder, the difference increases rapidly. Similarly when electrodes on the uppermost electrode plane are used for the current injection, the errors are fairly large when the model is truncated just above the corresponding electrode plane, Fig. 5.14 b). The errors on the electrode voltages in the same situations are shown in Table 5.2. As it can be seen when the model is truncated at 32 cm the error is negligible but, for example, when the truncation is made at z=14 cm, the error is big enough to affect on the reconstructed image. However, when the mesh of 32 cm is used the number of nodes is more than twice the number of nodes of the 14 cm mesh. This can be seen in Table 5.3. The relative errors in the computed reference voltages $U(\rho_0, z_0)$ are computed as $E = \|U_{\text{meas}} - U(\rho_0, z_0)\|_2 / \|U_{\text{meas}}\|_2$.

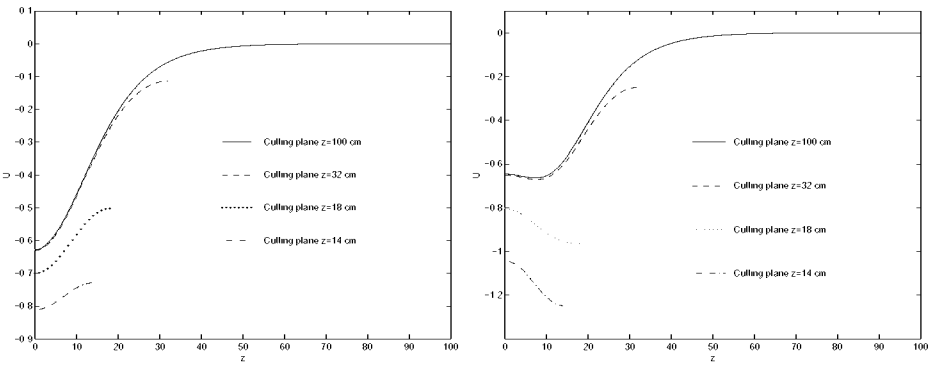

Figure 5.14: Voltages U as a function of height z when different height of tank has been used with a) 1st current injection and b) 33rd current injection.

In the static image reconstruction it is important to have as accurate forward solution (voltages on the electrodes) as possible. This, however, would necessitate the use of large meshes in order to avoid the above mentioned truncation error. To overcome this problem it is possible to use "long" elements in the mesh, starting e.g. from the furthermost current carrying electrodes or by using infinite elements

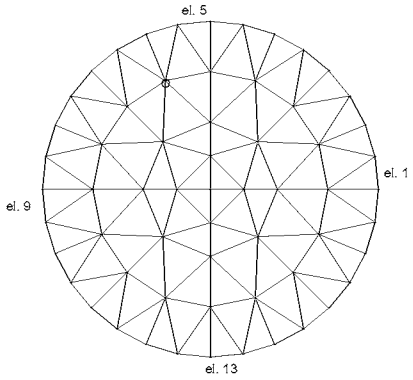

Figure 5.15: Positions of the electrodes (el.) and the point, where the decay of the voltages have been studied with different values of z, in $x-y$ -plane.

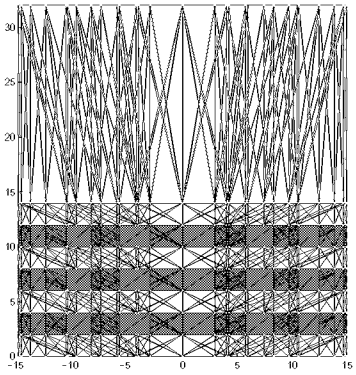

Figure 5.16: Mesh with equal size elements from the bottom to 14 cm and "long" elements from 14 cm to 32 cm.

Table 5.2: Errors (E) in voltages on the electrodes when different heights of the meshes have been used.

height of the mesh	E
14 cm	0.1117
18 cm	0.0274
32 cm	0.0008

Table 5.3: Number of the elements and nodes in the meshes with different heights.

height of the mesh	# of elements	# of nodes
14 cm	1848	3135
18 cm	2376	3971
32 cm	4224	6897
100 cm	13200	21109
infinite	1936	3344

Table 5.4: Errors (E) in voltages on the electrodes, when different heights of "long" elements have been used. z_s is the position where the "long" element starts from and z_s is end of the "long" element.

type of element	$z_s - z_e$	E
"long" element	14 cm - 32 cm	0.0156
"long" element	14 cm - 50 cm	0.0371
"long" element	14 cm - 100 cm	0.0680
"long" separable element	14 cm - 32 cm	0.0060
"long" separable element	14 cm - 50 cm	0.0193
"long" separable element	14 cm - 100 cm	0.0474

as explained in Section 3.3.4. These approaches were studied by computing the voltages on the electrodes using separable infinite elements, "long" elements and separable "long" elements. As a "long" element a 3D wedge element shown in Appendix I was used.

In Table 5.4, errors in voltages on the electrodes with "long" elements are shown. A mesh with "long" elements means that there is one element layer in the mesh whose elements reach from 14 cm to 32 cm (or to 50 cm or 100 cm) as shown in Fig. 5.16. In the separable "long" element -case the solution was assumed to be separable in x, y- and z-directions. In the z-direction these elements reached

Table 5.5: Errors in voltages on the electrodes, when separable infinite elements have been used.

decay	error
$\frac{1}{r^2}$	0.0017
exponential	0.0009

from 14 cm to 32 cm (50 cm, 100 cm).

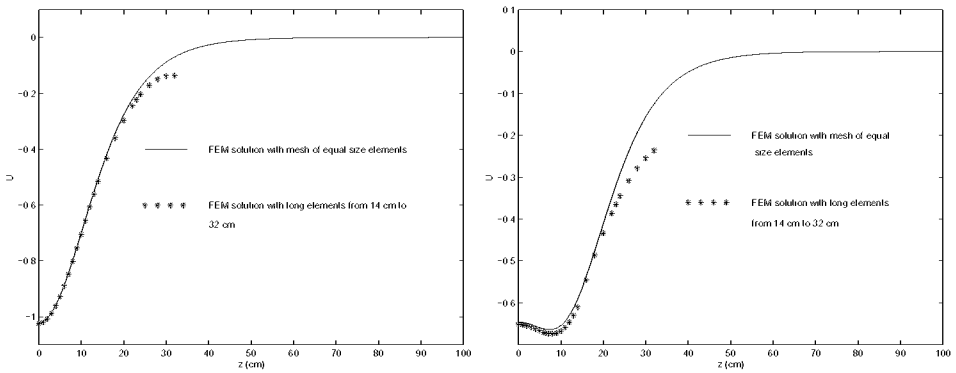

Figure 5.17: Voltages U as a function of height z when "long" elements with second order basis functions have been used with a) 1st current injection and b) 33rd current injection.

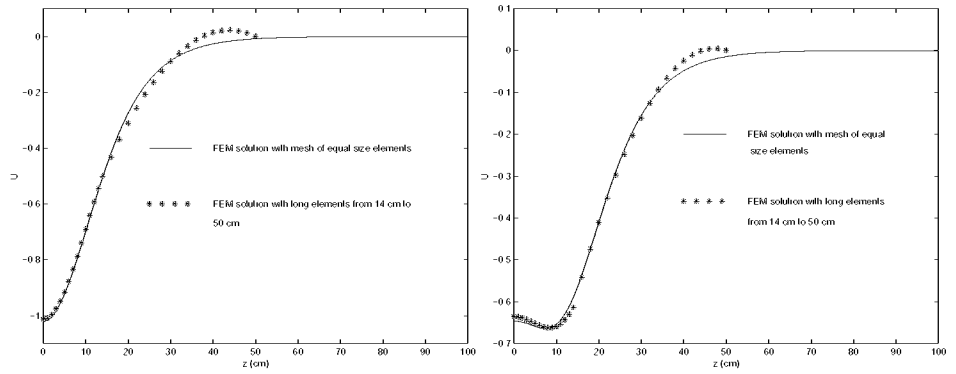

Figure 5.18: Voltages U as a function of height z when "long" elements with second order basis functions have been used with a) 1st current injection and b) 33rd current injection.

In static reconstruction it is important to have as accurate a forward model and also as accurate a numerical method as possible. The accuracy of the forward solver (FEM in this study) depends on the mesh density and "quality". The quality of the mesh Q has been defined as the mean of $Q_i = 3R_{\text{in}}(T_i)/R_{\text{out}}(T_i)$, where $R_{\text{in}}(T_i)$ is the radius of the inscribed sphere and $R_{\text{out}}(T_i)$ is the radius of the

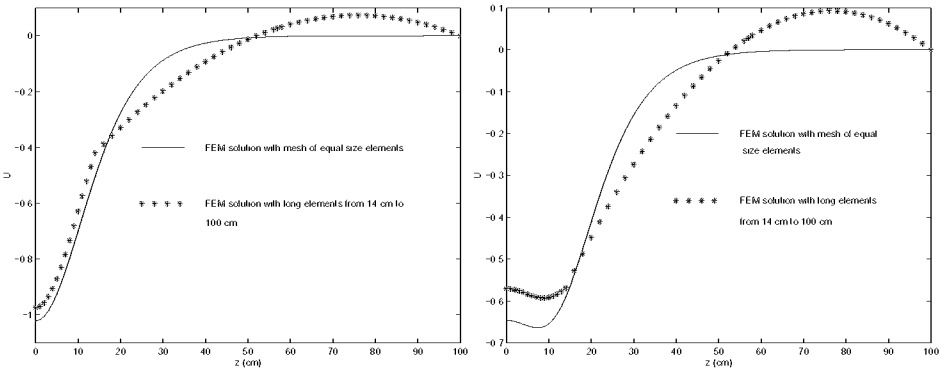

Figure 5.19: Voltages U as a function of height z when "long" elements with second order basis functions have been used with a) 1st current injection and b) 33rd current injection.

circumscribed sphere in the tetrahedron T_i [60]. For an ideal tetrahedron $Q_i = 1$. More study about the quality of the meshes used in EIT can be found in [103]. As can be seen from the Table 5.4, if separable "long" elements are used the errors are smaller because the elements are not as ill-conditioned as regular "long" elements (tetrahedral). In Fig. 5.17– 5.19, the differences between the true voltages and the voltages computed by using "long" elements with the second order basis functions are shown. The same effect can also be seen in the voltage curves. If the stretched element is too long the results become worse due to the ill-conditioning problem. On the other hand, if the "long" element is truncated near the electrodes, the voltages are incorrect due to the truncation.

The disadvantages of using "long" elements can be somewhat overcome by using infinite elements in the truncation boundary. The results of using infinite elements with $1/r^2$ decay (mapped infinite elements) and exponential decay are shown in Table 5.5 and the errors in the nodal voltages in the exponential decay -case in Figs. 5.21 and 5.20. The exponential decay represents the decay of the voltages better and therefore the errors are smaller than with $1/r^2$ decay. The smallest error in the voltages on the electrodes was obtained when z_1=14cm, z_2=15 cm and $L = 5$ (see Fig. 5.21). When z_1=14cm, z_2=16 cm and $L = 7$, as in Fig. 5.20, the error on the electrodes was 0.0023. If the voltages on the electrodes are wanted to be as accurate as possible the error will increase in the upper part of the domain, away from the electrodes.

5.2.2 Errors in the reconstructions

Before the actual image reconstructions, effects of the model truncation on the solutions were studied in homogeneous situations with different mesh sizes. In the

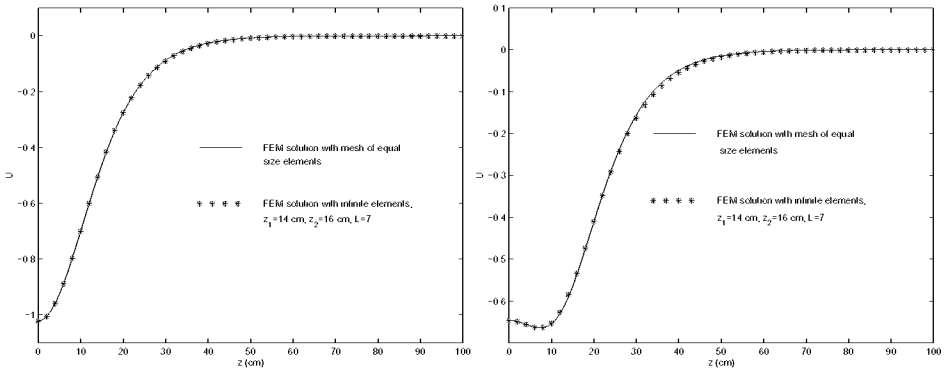

Figure 5.20: Voltages U as a function of height z when separable infinite elements with exponential decay have been used with a) 1st current injection and b) 33rd current injection.

first tests the voltage measurements were simulated in the homogeneous cylinder of height 32 cm. From the Fig. 5.22 it can be seen that when the reference voltages are computed in too "small" a mesh (height 18 cm) the reconstructed resistivity values are smaller than the true values near the truncation boundary. If the reference voltages are computed in too "long" a mesh (height 50 cm), Fig. 5.23, the resistivity values are bigger than the true values near the truncation boundary.

The error caused by assuming that the domain extends to infinity was studied by simulating the measured voltages in the cylinders of heights 50 cm and 100 cm. The error in the voltages that are computed with infinite elements decreases when the actual height of the domain increases, which can be seen in the Figs. 5.24–5.25. This is because the potentials have decayed almost to zero which is the assumption when infinite elements are used. However, even if the domain is 100 cm long, the maximum error in the reconstructed resistivities was about 13 %.

To study the effects of the model truncation on image reconstruction, a simulated resistivity distribution shown in Fig. 5.26 was used. The height of the cylindrical object was 32 cm and diameter 30 cm. Inside the cylinder there were two different targets whose position with respect to the cylinder can be seen in Fig. 5.26. The resistivity of the upper target was 500 Ωcm and the resistivity of the lower 100 Ωcm. The background value was 300 Ωcm.

The results when the reference voltages were computed with different mesh sizes are shown in Fig. 5.27–5.29. In the Fig. 5.27, the Jacobian was computed in the same size of the mesh as the measured voltages (z=32 cm). Also the reference voltages were computed in real dimensions. For the reconstruction only seven element layers from the bottom were used (from the bottom to 14 cm). In the Fig.

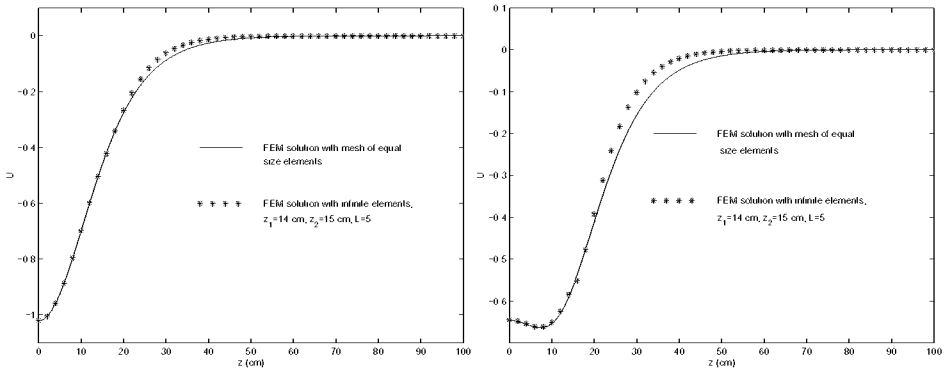

Figure 5.21: Voltages U as a function of height z when separable infinite elements with exponential decay have been used with a) 1st current injection and b) 33rd current injection.

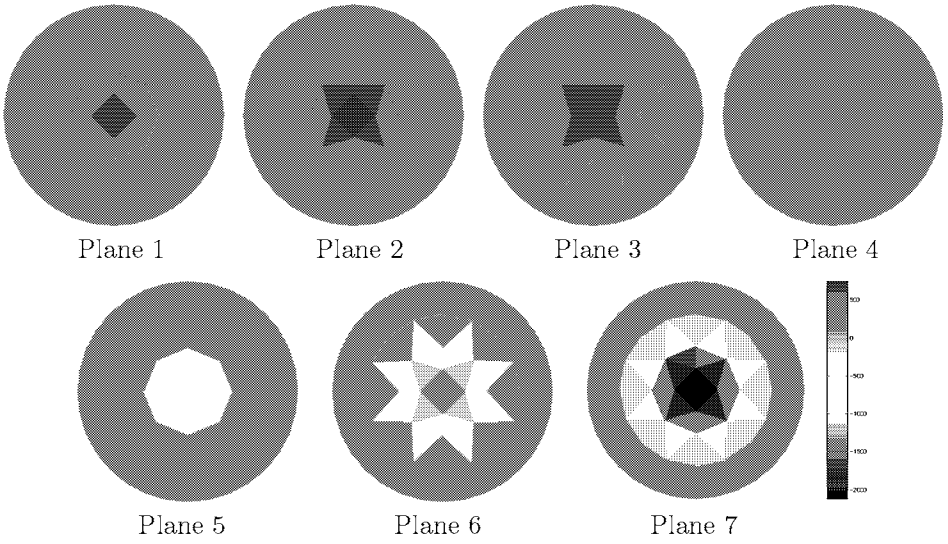

Figure 5.22: The static reconstruction from simulated homogeneous resistivity distribution (300 Ωcm). Plane 1 is on the bottom of the cylinder and plane 7 is the first layer above the uppermost electrode plane. The Jacobian has been calculated in same size of the mesh as the measured voltages (z=32 cm) and the reference voltages in the mesh of 18 cm with equal size finite elements and second order basis functions.

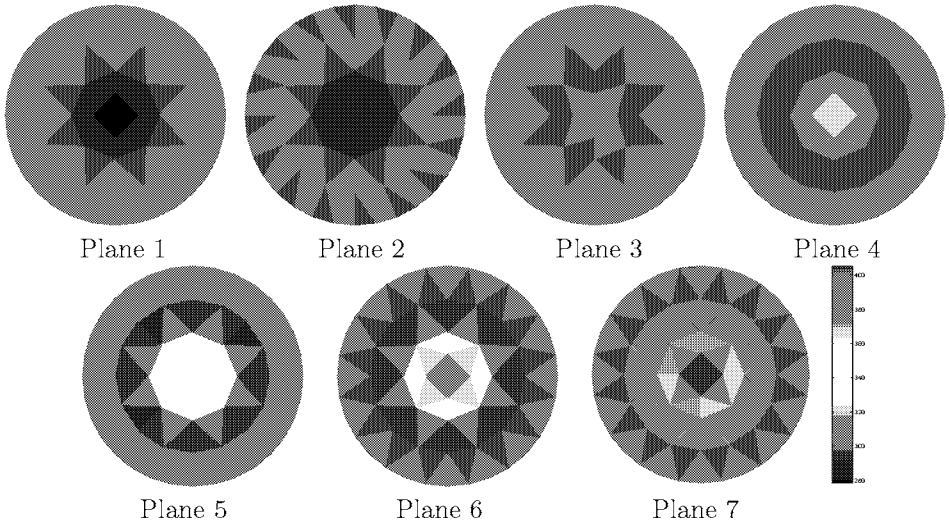

Figure 5.23: The static reconstruction from simulated homogeneous resistivity distribution (300 Ωcm). The Jacobian has been calculated in the same size of the mesh as the measured voltages (z=32 cm) and the reference voltages in the mesh of 50 cm with equal size finite elements and second order basis functions.

5.28 the reference voltages were computed in the mesh of 18 cm and in Fig. 5.29 in the mesh of 14 cm. As it can be seen, when the reference voltages were computed in the mesh whose height was 18 cm the lower target can be seen. Upper in the cylinder the error caused by the truncation is so big that the upper target can not be discerned. When the reference voltages were computed in the 14 cm mesh, the target on the bottom was hardly discernible. When the Jacobian was calculated in a truncated mesh (the reference was computed in the 32 cm mesh) the error is more pronounced near the truncation plane as can be seen in Fig. 5.30. The upper target can not be seen at all.

In Fig 5.31, the reference voltages were computed with separable infinite elements when $z_1 = 14$ cm, $z_2 = 15$ cm and L=5. One problem with infinite elements is the inaccuracy of the solution at the beginning of the infinite elements. Similar results have also been found in [90]. Effect of this inaccuracy can be seen in Fig. 5.31. It is hard to see the upper target because of the error in the middle of the image. At 32 cm the voltages do not decayed to zero and that causes error as well. The error caused when using "long" elements can be seen in Fig. 5.32.

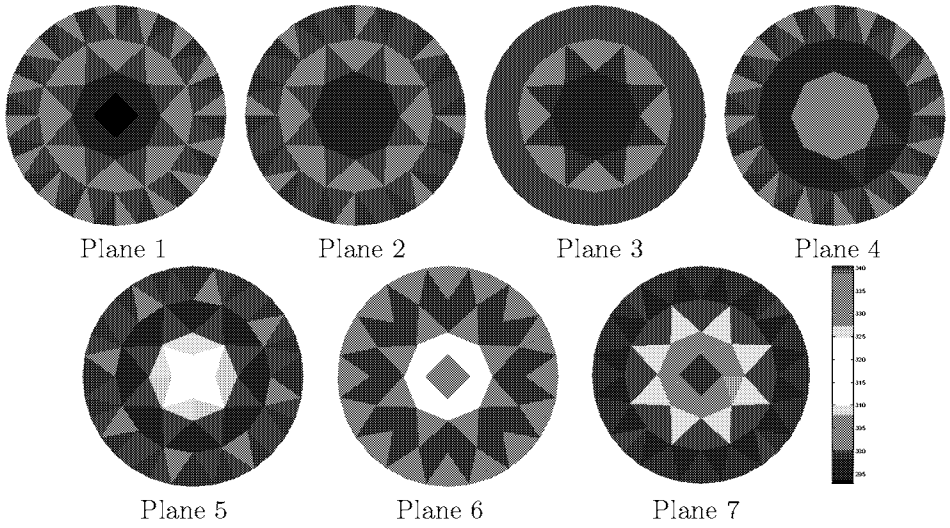

Figure 5.24: The static reconstruction from simulated homogeneous resistivity distribution (300 Ωcm). The Jacobian has been calculated in the same size of the mesh as the measured voltages (z=50 cm) and the reference voltages with separable infinite elements.

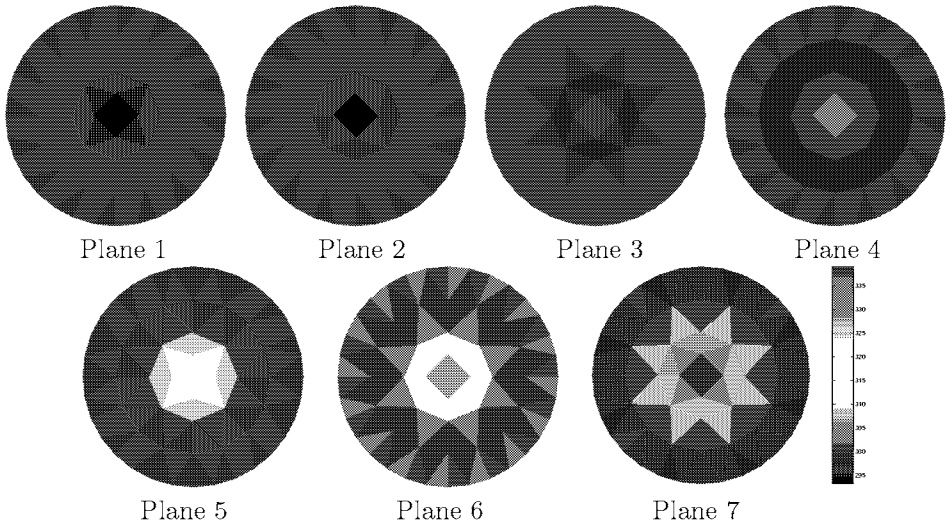

Figure 5.25: The static reconstruction from simulated homogeneous resistivity distribution (300 Ωcm, z=100 cm). The Jacobian has been calculated in the mesh of 50 cm and the reference voltages with separable infinite elements.

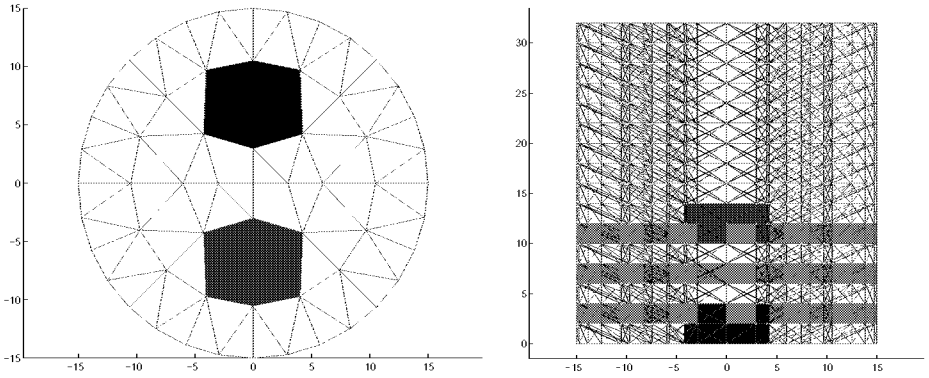

Figure 5.26: Simulated resistivity distribution a) from above, b) from the side.

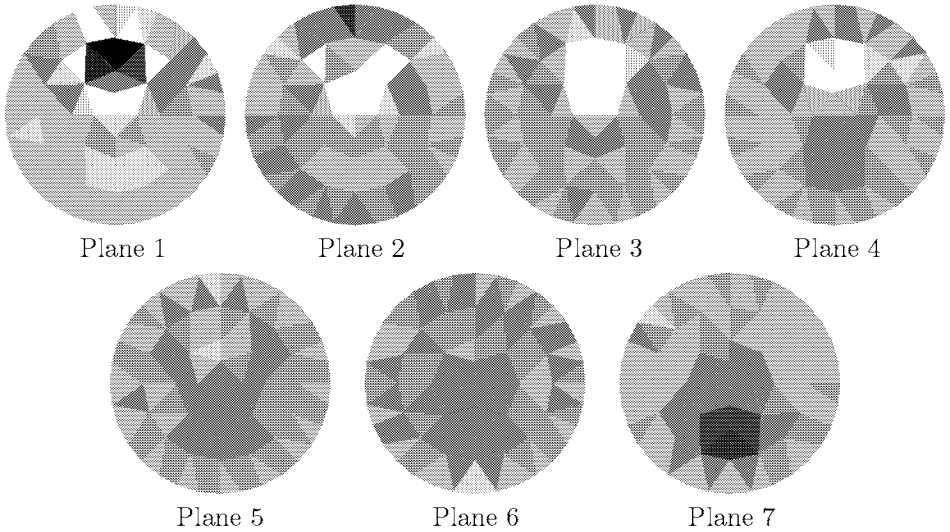

Figure 5.27: The static reconstruction from simulated resistivity distribution. The Jacobian and the reference voltages have been computed in same size of the mesh as the measured voltages (z=32 cm).

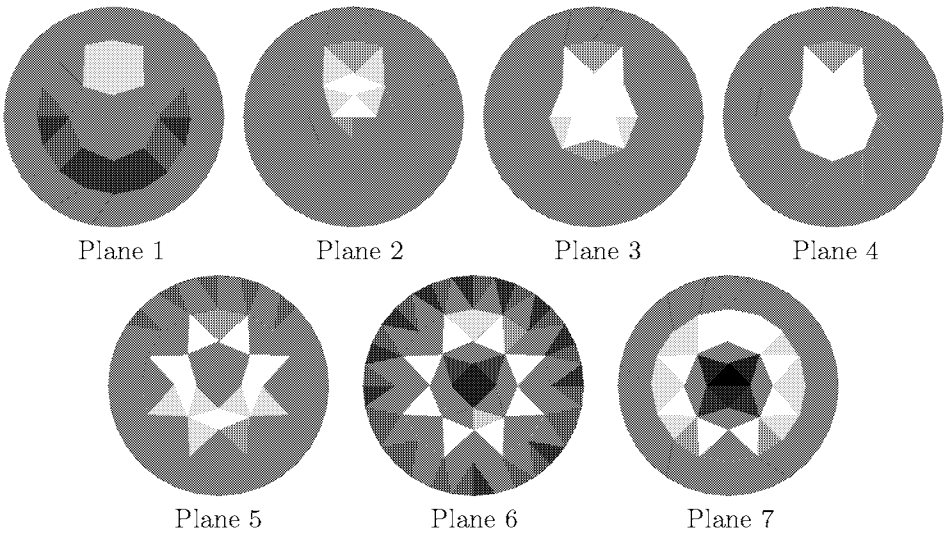

Figure 5.28: The static reconstruction from simulated resistivity distribution. The Jacobian has been computed in same size of the mesh as the measured voltages (z=32 cm) and the reference voltages in mesh of 18 cm.

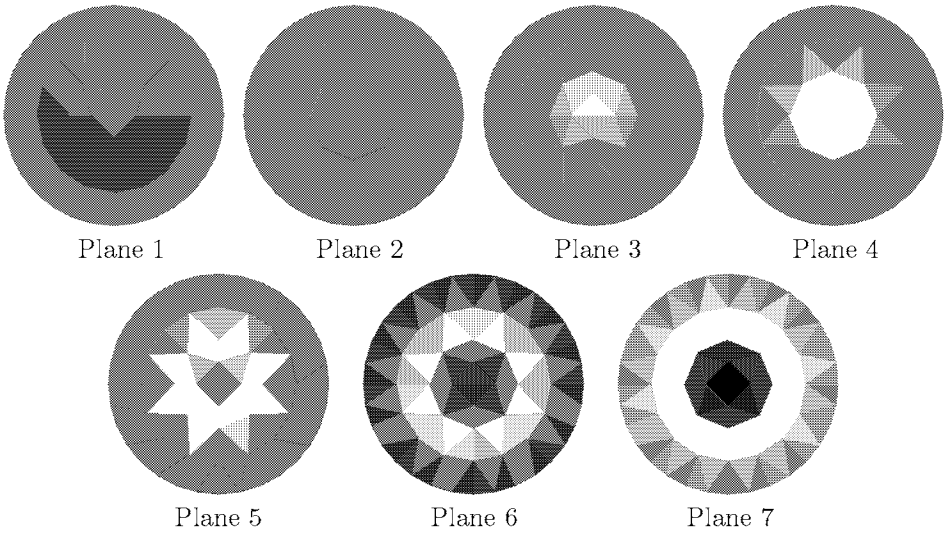

Figure 5.29: The static reconstruction from simulated resistivity distribution. The Jacobian has been computed in same size of the mesh as the measured voltages (z=32 cm) and the reference voltages in mesh of 14 cm.

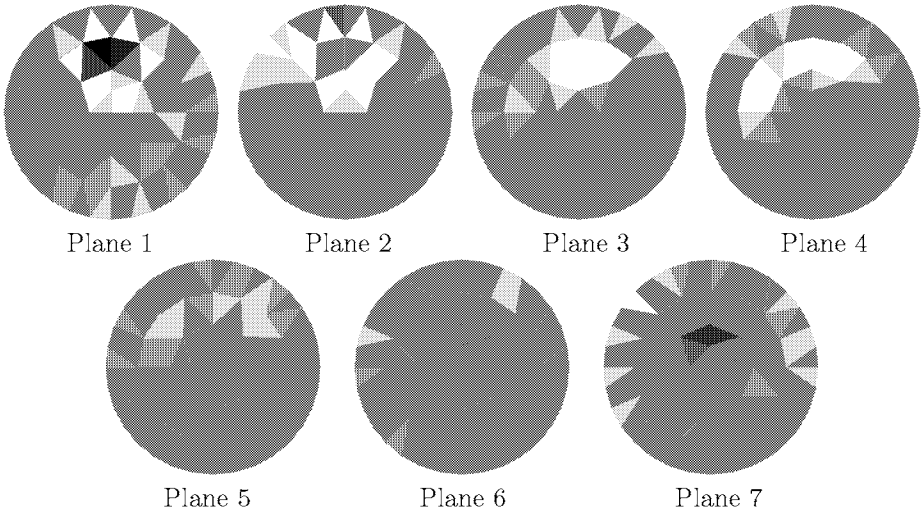

Figure 5.30: The static reconstruction from simulated resistivity distribution. The Jacobian has been calculated in mesh of 14 cm and the reference voltages in same size of the mesh as the measured voltages (z=32 cm).

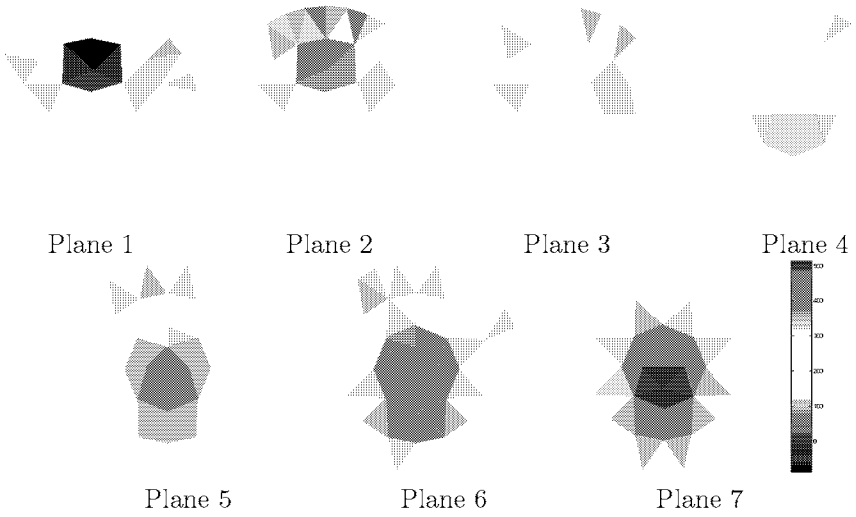

Figure 5.31: The static reconstruction from simulated resistivity distribution. The Jacobian has been calculated in same size of the mesh as the measured voltages (z=32 cm) and the reference voltages with separable infinite elements, z_1 = 14 cm, z_2 = 15 cm and L=5. The resistivities of the lower and the upper target were 100 Ωcm and 500 Ωcm, respectively. Background value was 300 Ωcm.

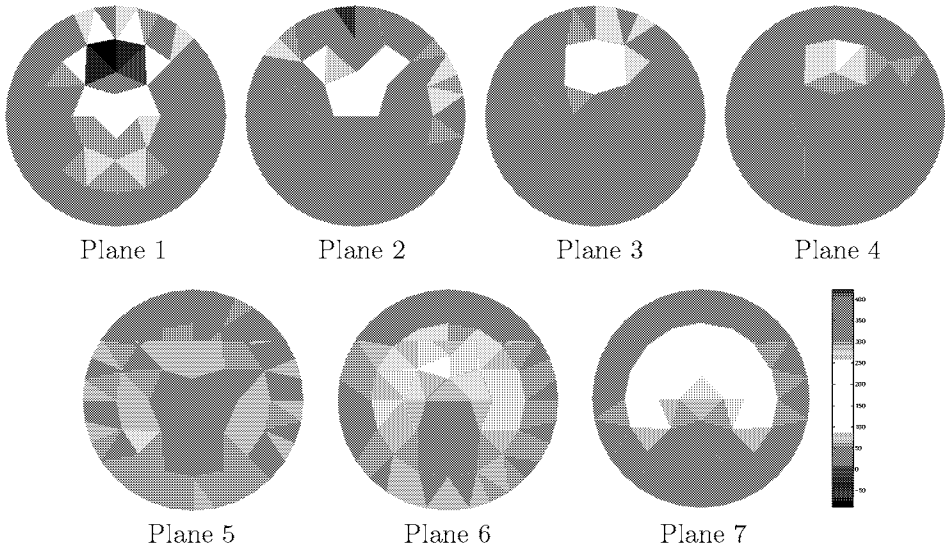

Figure 5.32: The static reconstruction from simulated resistivity distribution. The Jacobian has been calculated in same size of the mesh as the measured voltages (z=32 cm) and the reference voltages with separable "long" elements from 14 cm to 32 cm. Resistivity of the lower target was 100 Ωcm and the resistivity of the upper target was 500 Ωcm. Background value was 300 Ωcm.

CHAPTER VI

Conclusions

In this work 3D reconstruction methods for EIT have been proposed. The method is based on the finite element approximation for the complete electrode model. The proposed approaches do not impose any restrictions on the geometry of the object (boundary) or the geometry of the targets. For the model truncation problem, "extended" finite element methods were also introduced.

Static images were reconstructed with the proposed approaches using a numerical simulation. The aim of the study was not to compare the quality of the reconstructions or find the optimal priors for the problem to be minimized. Instead, the main interest was to compare the efficiency and the computer storage in different methods cases in which the absolute values of the resistivity distribution are of interest.

It was found that Gauss-Newton, conjugate gradient and steepest descent methods converged to the same solution because the functional to be minimized is same in these methods. Convergence of Gauss-Newton method is the most efficient of the three because the curvature information provided by the Hessian is also taken into account. However, the memory demand in Gauss-Newton method is much bigger than in the cases of Conjugate gradient and Steepest descent methods which may limit the use of the Gauss-Newton method in cases of large dimensional problems. Memory need of Conjugate gradient and Steepest descent methods is small and these methods are suitable especially for large dimensional problems. Convergence rate of steepest descent method is poor but it can be enhanced remarkably by using inexact line search. Conjugate gradient method is preferable to steepest descent method because of significantly shorter computational time which can be further reduced by using inexact line search. In nonlinear conjugate gradient method the search directions are not as optimal as search directions in the case of Gauss-Newton method and therefore more iteration steps are needed for the convergence. However, it has to be noticed that if absolute resistivity values are not needed and only qualitative images are wanted, the number of the iteration steps which are needed for the reconstruction is remarkably smaller. Also in the proposed block-nonlinear conjugate-gradient method the gradients needed

for the search direction can be computed in separate blocks. This reduces further the need of storage in the computation and allows parallelization and the computational time can be further reduced.

When Kaczmarz and Extended Kalman filter iterations are compared with Gauss-Newton, Conjugate gradient and Steepest descent methods, it is important to notice that they do not converge to the same solution due to different priors associated. Extended Kalman filter is a proper reconstruction method also in stationary situation. One weakness in this method is that the memory need with spatial regularization is huge. Finding less memory demanding ways of incorporating spatial regularization into the state estimation scheme in EIT is a topic of on-going research. Changing the order of current injections improved the quality of the extended Kalman filter estimates considerably. The memory need of the Kaczmarz iteration is smallest comparing to the other proposed reconstruction methods. However, the problem in Kaczmarz method arises from the instability of the solution. In order to get feasible solutions one should know when to cut the iteration.

It was found that obtaining the absolute resistivity values requires more than one iteration steps. Also the priors have significant effect on final resistivity values of the reconstruction. If the iterative reconstruction methods and more accurate priors are used the absolute resistivity values obtained with EIT from human subjects could be used for example in inverse EEG and ECG problems, in which the internal current sources are estimated. The use of resistivity estimates is believed to improve the accuracy of the source localization [77]. In human experiments the problem is that the boundary shape is rarely known. However, this problem can be solved in many ways. MRI or CT images from which the boundary shape could be extracted could be utilized. Many commercial systems have been developed for external boundary shape reconstruction. These are usually based on laser and digital camera techniques, see for example PROFA [21].

If static images of humans are required the boundary conditions on the "cutting planes", that is, the termination boundary of the FEM mesh, should be carefully considered. The obvious approach would be to extend the computations well beyond the furthest electrode planes. Then the current flow across the termination boundary would be insignificant, which in turn would justify the use of Neumann boundary conditions ($\sigma \partial u/\partial n = 0$) on these boundaries. However, this approach means that the number of parameters increases significantly and that the geometry of the object should be possible to model also well outside the principal regions of interest. It was found that in order to make the error of the voltages on the electrodes fairly small, the mesh should be extended as far as twice the radius of the cylinder.

In this work, the model truncation problem was studied with separable infinite elements, "long" finite elements and separable "long" elements. It was found that approximately the same accuracy can be obtained by using infinite elements as by using a mesh whose height is twice the radius of the cylinder. The advantage of infinite elements is that the number of nodes needed is only half of that needed in the big mesh (see Table 5.3). Hence it does not take so much time to calculate

the voltages for the static reconstructions. For example, with Matlab the time needed for computations with the mesh of 6897 nodes (height of 32 cm) was four times that needed when the infinite elements were used (3344 nodes). However, there are certain difficulties in using infinite elements, for example, choosing the decay function. There are also adjustable parameters, the values of which can be difficult to find in practice. It was also found that there are inaccuracies in the solution (potentials) at the beginning of the infinite elements. When the infinite elements were utilized in the image reconstruction, there was an artifact in the center of the image due to the mismatch in the forward solution. The error was almost as big as that when "long" separable elements were used. This is because a mesh of 32 cm was used as a test case. If the object to be imaged was longer, the error with infinite elements would be smaller than that when "long" elements are used.

In testing the infinite elements, a cylindrical volume which was assumed to be (almost) unbounded in one direction was considered. The idea that the three-dimensional basis functions are separable was used and therefore the one-dimensional infinite elements can be used also in 3D. This approach is suitable only in situations in which the object to be imaged is cylindrical and the voltages decay only in one direction. When more complicated geometries are used, the separable basis functions cannot be utilized.

In static imaging when real measurements are used, the accuracy requirement of the computed potentials on the electrodes that correspond to the (initial) distribution ρ_0 is very high. It was found that in certain cases the required accuracy can be obtained with relatively sparse finite element mesh when the second order basis functions are used [103, 109, 108]. The modelling of the curved shapes, such as organs, is also easier with these functions because the shapes of the elements can be curved as well. In principle, the required accuracy could also be obtained with the first order basis but this would necessitate the construction of another much denser mesh. This other mesh should match the same anatomical structures as the mesh used in the inverse computations. Since mesh generation is one of the most cumbersome tasks in the method, the use of the second order basis yields an important benefit.

REFERENCES

[1] B.D.O. Anderson and J.B. Moore. *Optimal Filtering.* Prentice Hall, 1979.

[2] S. R. Arridge. Optical tomography in medical imaging. *Inv Probl*, 15:R41–R93, 1999.

[3] S. R. Arridge and M. Schweiger. A general framework for iterative reconstruction algorithms in optical tomography, using a finite element method. In C. Borgers and F. Natterer, editors, *Computational Radiology and Imaging: Therapy and Diagnosis*, volume 110 of *IMA Volumes in Mathematics and its Applications*, pages 45–70. IMA, Springer-Verlag, 1998.

[4] D.C. Barber and B.H. Brown. Recent developments in applied potential tomography. In Bacharac, editor, *Information processing in medical imaging*, pages 106–121. Martinus Nichoff, 1986.

[5] R.H. Bayford, A. Gibson, A. Tizzard, T. Tidswell, and D.S. Holder. Solving the forward problem in electrical impedance tomography for the human head using ideas (integrated design engineering analysis software), a finite element modelling tool. *Physiol. Meas*, 22:55–64, 2001.

[6] G. Beer and J.L.Meek. Infinite domain elements. *International Journal for Numerical Methods in Engineering*, 17:43–52, 1981.

[7] G. Beer and J.O. Watson. Infinite boundary elements. *Int J Numer Methods Eng*, 28:1233–1247, 1989.

[8] P. Bettess. Infinite elements. *Int J Numer Methods Eng*, 11:53–64, 1977.

[9] P. Bettess. *Infinite Elements.* Penshaw Press, Cleadon, 1992.

[10] Å. Björck. *Numerical methods for least squares problems.* SIAM, 1996.

[11] R. S. Blue, D. Isaacson, and J. C. Newell. Real-time three-dimensional electrical impedance imaging. *Physiol. Meas*, 21:15–26, 2000.

[12] S.C. Brenner and L.R. Scott. *The Mathematical Theory of Finite Element Methods.* Springer, 1994.

[13] B.H. Brown, D.C. Barber, and A.D. Seagar. Applied potential tomography: possible clinical applications. *Clin Phys Physiol Meas*, 6:109–121, 1985.

[14] A.P. Calderón. On an inverse boundary value problem. In W.H. Meyer and M.A. Raupp, editors, *Seminar on Numerical Analysis and its Applications to Continuum Physics*, pages 65–73, Rio de Janeiro, 1980. Brazilian Math. Society.

[15] M. Cheney and D. Isaacson. Distinguishability in impedance imaging. *IEEE Trans Biomed Eng*, 39:852–860, 1992.

[16] M. Cheney, D. Isaacson, and J. C. Newell. Electrical impedance tomography. *SIAM Rev*, 41:85–101, 1999.

[17] K.-S. Cheng, D. Isaacson, J.C. Newell, and D.G. Gisser. Electrode models for electric current computed tomography. *IEEE Trans Biomed Eng*, 36:918–924, 1989.

[18] V.G. Cherednichenko and G.V. Veryovkina. Inverse conductivity problem in the two-dimensional case. *Ill-Posed Problems in Natural Science*, pages 270–276, 1992.

[19] C. Cuvelier and A. Segal. *Finite element methods and Navier-Stokes equations*. D. Reidel Publishing Company, 1986.

[20] F. Dickin and M. Wang. Electrical resistance tomography for process tomography. *Meas Sci Tech*, 7:247–260, 1996.

[21] Duncan Hynd Associates Ltd, First Floor Offices, 53 High Street, Chinnor Oxon OX9 4DJ, UK. *PROFA SYSTEMS*.

[22] R. Fletcher. *Practical methods of optimization*. John Wiley & Sons Ltd., 1987.

[23] A. Friedman and V. Isakov. On the uniqueness in the inverse conductivity problem with one measurement. *Indiana University Mathematics Journal*, 38:563–579, 1989.

[24] R. Gadd, F. Vinther, P.M. Record, and P. Rolfe. Reconstruction of three-dimensional data for electrical impedance tomography. *Electron Lett*, 28:974–976, 1992.

[25] K. Gerdes and L. Demkowicz. Solution of 3D-laplace and helmholtz equations in exterior domains using hp-infinite elements. *Comput. Methods Appl. Mech. Engrg.*, 137:239–273, 1996.

[26] P.E. Gill, W. Murray, and M.H. Wright. *Practical optimization*. Agademic Press, Inc., 1981.

[27] J. Goble, M. Cheney, and D. Isaacson. Electrical impedance tomography in three dimensions. *Appl Comput Electromagn Soc J*, 7:128–147, 1992.

[28] C. W. Groetsch. *Inverse Problems in the Mathematical Sciences*. Vieweg, 1993.

[29] J. Hämäläinen and J. Järvinen. *Elementtimenetelmä virtauslaskennassa*. CSC-Tieteellinen laskenta, 1994.

[30] P. C. Hansen. The truncated SVD as a method of regularization. *BIT*, 27:534–553, 1987.

[31] P.C. Hansen. *Regularization Tools: A Matlab package for analysis and solution of discrete ill-posed problems*. UNI-C, Technical university of Denmark, 1992.

[32] L. M. Heikkinen, M. Vauhkonen, T. Savolainen, and J.P. Kaipio. Modelling of internal structures and electrodes in electrical process tomography. *Measur Sci Technol*, 12:1012–1019, 2001.

[33] L.M. Heikkinen, T. Vilhunen, R.M. West, and M. Vauhkonen. Simultaneous reconstruction of electrode contact impedances and internal electrical properties: II. Laboratory experiments. *Measur Sci Technol*, 13:1855–1861, 2002.

[34] D. Henwood and J. Bonet. *Finite Elements, A Gentle Introduction*. Macmillan, 1996.

[35] E. Hinton and D.R.J. Owen. *An Introduction to Finite Element Computations*. Pineridge Press Limited, Swansea, U.K., 1979.

[36] http://www.mathworks.com/.

[37] P. Hua, E.J. Woo, J.G. Webster, and W.J. Tompkins. Iterative reconstruction methods using regularization and optimal current patterns in electrical impedance tomography. *IEEE Trans Med Imaging*, 10:621–628, 1991.

[38] P. Hua, E.J Woo, J.G. Webster, and W.J. Tompkins. Using compound electrodes in electrical impedance tomography. *IEEE Trans Biomed Eng*, 40:29–34, 1993.

[39] A. Le Hyaric and M.K. Pidcock. An image reconstruction algorithm for three-dimensional electrical impedance tomography. *IEEE Trans Biomed Eng*, 48(2):230–235, 2001.

[40] Y.Z. Ider, N.G. Gencer, E. Atalar, and H. Tosun. Electrical impedance tomography of translationally uniform cylindrical objects with general cross-ectional boundaries. *IEEE Trans Med Imaging*, 9:49–59, 1990.

[41] V. Isakov. On uniqueness of recovery of a discontinuous conductivity coefficient. *Commun Pure Appl Math*, 41:865–877, 1988.

[42] G. James. *Modern Engineering Mathematics*. Prentice Hall, 2001.

[43] S. Järvenpää. A finite element model for the inverse conductivity problem. Phil. Lic. thesis, University of Helsinki, Finland, 1996.

[44] C.R. Johnson. Numerical methods for bioelectric field problems. In J.D. Bronzino, editor, *The biomedical Engineering Handbook*, chapter 12, pages 162–180. CRC, Trinity College, Hartford, Connecticut, USA, 1995.

[45] J.E. Dennis Jr and R.B. Schnabel. *Numerical methods for unconstrained optimization and nonlinear equations*. Society for industrial and applied Mathematics, 1996.

[46] J.P. Kaipio, P.A. Karjalainen, E. Somersalo, and M. Vauhkonen. State estimation in time-varying electrical impedance tomography. *Ann New York Acad Sci*, 873:430–439, 1999.

[47] J.P. Kaipio, V. Kolehmainen, M. Vauhkonen, and E. Somersalo. Inverse problems with structural prior information. *Inv Probl*, 15:713–729, 1999.

[48] J.P. Kaipio, A. Seppänen, E. Somersalo, and H. Haario. Posterior covariance related optimal current patterns in electrical impedance tomography. *Inv Probl*, 2003. (submitted).

[49] J.P. Kaipio, A. Seppänen, E. Somersalo, and H. Haario. Statistical inversion approach for optimizing current patterns in EIT. In *3rd World Congress on Industrial Process Tomography, Banff, Canada*, pages 683–688, 2003.

[50] J.P. Kaipio and E. Somersalo. Nonstationary inverse problems and state estimation. *J. Inv. Ill-Posed Problems*, 7:273–282, 1999.

[51] W. Kaplan. *Maxima and Minima with applications*. Wiley, 1999.

[52] P.A. Karjalainen. *Regularization and Bayesian methods for evoked potential esimation*. PhD thesis, University of Kuopio, Department of Applied Physics, 1997.

[53] H. Kim and J.K. Seo. Unique determination of a collection of a finite number of cracks from two boundary measurements. *SIAM J Math Anal*, 27:1336–1340, 1996.

[54] R. Kohn and M. Vogelius. Determining conductivity by boundary measurements. *Commun Pure Appl Math*, 37:289–298, 1984.

[55] R.V. Kohn and M. Vogelius. Determining conductivity by boundary measurements II. Interior results. *Commun Pure Appl Math*, 38:643–667, 1985.

[56] V. Kolehmainen. *Novel Approaches to Image Reconstruction in Diffusion Tomography*. PhD thesis, University of Kuopio, Kuopio, Finland, 2001.

[57] A.V. Korjenevsky. Reconstruction of absolute conductivity distribution in electrical impedance tomography. In *Proc IX Int Conf Electrical Bio-Impedance*, pages 532–535, Heidelberg, Germany, 1995.

[58] M. Kuzuoglu, M. Moh'dSaid, and Y. Ider. Analysis of three-dimensional software EIT phantoms by the finite element method. *Clin Phys Physiol Meas, Suppl A*, 13:135–138, 1992.

[59] G.A. Kyriacou, M.A. Alexiou, C.S. Kokourlis, and J.N. Sahalos. A three dimensional FEM model of the human torso for electrical impedance applications. In *Proc IX Int Conf Electrical Bio-Impedance*, pages 484–485, Heidelberg, Germany, 1995.

[60] J.-F. Lee and R. Dyczij-Edlinger. Automatic mesh generation using a modified Delaunay tessalation. *IEEE Ant Propag Mag*, 39:34–45, 1997.

[61] J.M.M.C. Marques and D.R.J. Owen. Infinite elements in quasi-static materially nonlinear problems. *Computers and Structures*, 18:739–751, 1984.

[62] F.J. McArdle, B.H. Brown, R.G. Pearse, and D.C. Barber. The effect of the skull of low-birthweight neonates on applied potential tomography imaging of centralised resistivity changes. *Clin Phys Physiol Meas, Suppl A*, 9:55–60, 1988.

[63] P. Metherall, D.C. Barber, and R.H. Smallwood. Three dimensional electrical impedance tomography. In *Proc IX Int Conf Electrical Bio-Impedance*, pages 510–511, Heidelberg, Germany, 1995.

[64] P. Metherall, D.C. Barber, R.H. Smallwood, and B.H. Brown. Three-dimensional electrical impedance tomography. *Nature*, 380:509–512, 1996.

[65] P. Metherall, R.H. Smallwood, and D.C. Barber. Three dimensional electrical impedance tomography of the human thorax. In *Proc 18th Int Conf IEEE Eng Med Biol Society*, 1996.

[66] C.E. Miller and C.S. Henriquez. Finite element analysis of bioelectric phenomena. *Crit. Rev. in Biomed. Eng.*, 18:207–233, 1990.

[67] J.P. Morucci, M. Granie, M. Lei, M. Chabert, and P.M. Marsili. 3D reconstruction in electrical impedance imaging using a direct sensitivity matrix approach. *Physiol Meas*, 16:A123–A128, 1995.

[68] J.L. Mueller, D. Isaacson, and J.C. Newell. A reconstruction algorithm for electrical impedance tomography data collected on rectangular electrode arrays. *IEEE Trans Biomed Eng*, 46(11):1379–1386, 1999.

[69] J.L. Mueller, D. Isaacson, and J.C. Newell. Reconstruction of conductivity changes due to ventilation and perfusion from EIT data collected on a rectangular electrode array. *Physiol. Meas*, 22:97–106, 2001.

[70] T. Murai and Y. Kagawa. Electrical impedance computed tomography based on a finite element model. *IEEE Trans Biomed Eng*, 32:177–184, 1985.

[71] D. Murphy, P. Burton, R. Coombs, L. Tarassenko, and P. Rolfe. Impedance imaging in the newborn. *Clin Phys Physiol Meas, Suppl A*, 8:131–140, 1987.

[72] A.I. Nachman. Global uniqueness for a two-dimensional inverse boundary value problem. *Annals of Math*, 143:71–96, 1996.

[73] F. Natterer. *The Mathematics of Computerised Tomography.* Wiley, New York, 1986.

[74] F. Natterer and F. Wubbeling. *Mathematical Methods in Image Reconstruction.* SIAM Philadelphia, 2001.

[75] J. Nocedal and S.J. Wright. *Numerical optimization.* Springer series in operations reseach. Springer-Verlag, New York, 1999.

[76] J. Ollikainen, M. Vauhkonen, P.A. Karjalainen, and J.P. Kaipio. Effects of local skull inhomogeneities on EEG source estimation. *Med Eng Phys*, 21:143–154, 1999.

[77] J. Ollikainen, M. Vauhkonen, P.A. Karjalainen, P.J. Ronkanen, and J.P. Kaipio. Effect of skull inhomogeneities on EEG localization accuracy. In *Proc 19th Int Conf IEEE Eng Med Biol Society*, pages 2120–2123, Chicago, October 30-November 2 1997.

[78] C. Emson P. Bettess and K. Bando. Some useful techniques for testing infinite

elements. *Appl Math Modelling*, 6:436–440, 1982.

[79] K. Paulson, W. Breckon, and M. Pidcock. Electrode modelling in electrical impedance tomography. *SIAM J Appl Math*, 52:1012–1022, 1992.

[80] N. Polydorides. *Image reconstruction algorithms for soft-field tomography.* PhD thesis, UMIST, 2002.

[81] N. Polydorides, W. Lionheart, and H. McCann. Krylov subspace iterative techniques: On the detection of brain activity with electrical impedance tomography. *IEEE Trans Med Imaging*, 21{6):596–603, 2002.

[82] K.S. Rabbani, M. Hassan, and A. Kiber. 3D object localization using EIT measurements at two levels. *Physiol Meas*, 17:189–199, 1996.

[83] K.S. Rabbani and A.M.B.H. Kabir. Studies on the effect of the third dimension on a two- dimensional electrical impedance tomography system. *Clin Phys Physiol Meas*, 12:393–402, 1991.

[84] A.G. Ramm. A simple proof of the uniqueness theorem in impedance tomography. *Appl Math Lett*, 1:287–290, 1988.

[85] P. Ronkanen. Three-dimensional electrical impedance tomography (In Finnish). Master's thesis, University of Kuopio, Department of Applied Physics, 1997.

[86] R.J. Sadleir, R.A. Fox, F.J. van Kann, and Y. Attikiouzel. Estimating volumes of intra-abdominal blood using electrical impedance imaging. In *Proc 14th Int Conf IEEE Eng Med Biol Society*, pages 1750–1751, 1992.

[87] J.N. Sahalos, G.A. Kyriacou, P. Bonovas, A. Rigas, and C.S. Kokourlis. The electrical impedance of the human head by using a 3-D FEM model. In *Proc IX Int Conf Electrical Bio-Impedance*, pages 489–490, Heidelberg, Germany, 1995.

[88] J.N. Sahalos, G.A. Kyriacou, and E. Vafiadis. An efficient finite-element algorithm for 3D layered complex structure modelling. *Physiol Meas*, 15:A65–A68, 1994.

[89] A. Seppänen, M. Vauhkonen, P.J. Vauhkonen, E. Somersalo, and J.P. Kaipio. State estimation with fluid dynamical evolution models in process tomography – an application to impedance tomography. *Inv Probl*, 17:467–484, 2001.

[90] L. Simoni and B.A. Schrefler. Mapped infinite elements in soil consolidation. *Int J Numer Methods Eng*, 24:513–527, 1987.

[91] E. Somersalo, M. Cheney, and D. Isaacson. Existence and uniqueness for electrode models for electric current computed tomography. *SIAM J Appl Math*, 52:1023–1040, 1992.

[92] H.W. Sorenson. *Parameter Estimation: Principles and Problems.* Marcel Dekker, 1980.

[93] Z. Sun. The inverse conductivity problem in two dimensions. *Journal of Differential Equations*, 87:227–255, 1990.

[94] J. Sylvester. An anisotropic inverse boundary value broblem. *Commun Pure Appl Math*, 43:201–232, 1990.

[95] J. Sylvester and G. Uhlmann. A uniqueness theorm for inverse boundary value problem in electrical prospection. *Comm Pure Appl Math*, 39:91–112, 1986.

[96] J. Sylvester and G. Uhlmann. A global uniqueness theorem for an inverse boundary value problem. *Ann Math*, 125:153–169, 1987.

[97] A.T. Tidswell, A. Gibson, R.H. Bayford, and D.S. Holder. Three-dimensional electrical impedance tomography of human brain activity. *NeuroImage*, 13:283–294, 2001.

[98] A.T. Tidswell, A. Gibson, R.H. Bayford, and D.S. Holder. Validation of a 3d reconstruction algorithm for eit of human brain function a realistic head-shaped tank. *Physiol. Meas*, 22:177–185, 2001.

[99] M. Vauhkonen. Electrical impedance tomography (In Finnish). Master's thesis, Department of Applied Physics, University of Kuopio, 1994.

[100] M. Vauhkonen. *Electrical Impedance Tomography and Prior Information.* PhD thesis, University of Kuopio, Kuopio, Finland, 1997.

[101] M. Vauhkonen, J.P. Kaipio, E. Somersalo, and P.A. Karjalainen. Electrical impedance tomography with basis constraints. *Inv Probl*, 13:523–530, 1997.

[102] M. Vauhkonen, P.A. Karjalainen, and J.P. Kaipio. A Kalman filter approach to track fast impedance changes in electrical impedance tomography. *IEEE Trans Biomed Eng*, 45:486–493, 1998.

[103] P. Vauhkonen. Second order and infinite elements in three dimensional electrical impedance tomography. Phil. Lic. thesis, University of Kuopio, Finland, 1999.

[104] P.J. Vauhkonen and M. Vauhkonen. Errors due to the model truncation in three-dimensional EIT. In *1st EPSRC Engineering Network meeting Biomedical applications of EIT*, London, April 14-16 1999.

[105] P.J. Vauhkonen, M. Vauhkonen, and J.P. Kaipio. Errors due to the truncation of the computational domain in static three-dimensional electrical impedance tompography. *Physiol Meas*, 21:125–135, 2000.

[106] P.J. Vauhkonen, M. Vauhkonen, and J.P. Kaipio. Fixed-lag smoothing and state estimation in dynamic electrical impedance tomography. *Int J Numer Methods Eng*, 50:2195–2209, 2001.

[107] P.J. Vauhkonen, M. Vauhkonen, T. Mäkinen, P.A. Karjalainen, and J.P. Kaipio. Dynamic electrical impedance tomography – phantom studies. *Inv Prob Eng*, 8:495–510, 2000.

[108] P.J. Vauhkonen, M. Vauhkonen, T. Savolainen, and J.P. Kaipio. Static three-dimensional electrical impedance tomography. *Ann New York Acad Sci*, 873:472–481, 1999.

[109] P.J. Vauhkonen, M. Vauhkonen, T. Savolainen, and J.P. Kaipio. Three-dimensional electrical impedance tomography based on the complete electrode model. *IEEE Trans Biomed Eng*, 46:1150–1160, 1999.

[110] M.N. Viladkar, P.N. Godbole, and J. Noorzaei. Some new three-dimensional infinite elements. *Computers and Structures*, 34:455–467, 1990.

[111] T. Vilhunen, J.P. Kaipio, P.J. Vauhkonen, T. Savolainen, and M. Vauhkonen. Simultaneous reconstruction of electrode contact impedances and internal electrical properties: I. theory. *Measur Sci Technol*, 13:1848–1854, 2002.

[112] J.G. Webster. *Electrical Impedance Tomography.* Adam Hilger, Bristol, UK, 1990.

[113] A. Wexler. Electrical impedance imaging in two and three dimensions. *Clin Phys Physiol Meas, Suppl A*, 9:29–33, 1988.

[114] A. Wexler, B. Fry, and M.R. Neuman. Impedance computed tomography algorithm and system. *Appl Opt*, 24:3985–3992, 1985.

[115] R.A. Williams and M.S. Beck, editors. *Process Tomography, Principles, Techniques and Applications.* Butterworth-Heinemann Ltd, Oxford, 1995.

[116] E.J. Woo, P.Hua, J.G. Webster, and W.J. Tompkins. Finite-element method in electrical impedance tomography. *Med Biol Eng Comput*, 32:530–536, 1994.

[117] T.J. Yorkey, J.G. Webster, and W.J. Tompkins. Comparing reconstruction algorithms for electrical impedance tomography. *IEEE Trans Biomed Eng*, 34:843–852, 1987.

[118] O.C. Zienkiewicz, K. Bando, P. Bettess, C. Emson, and T.C. Chiam. Mapped infinite elements for exterior wave problems. *Int J Numer Methods Eng*, 21:1229–1251, 1985.

Appendix I

Basis functions for 3D wedge element

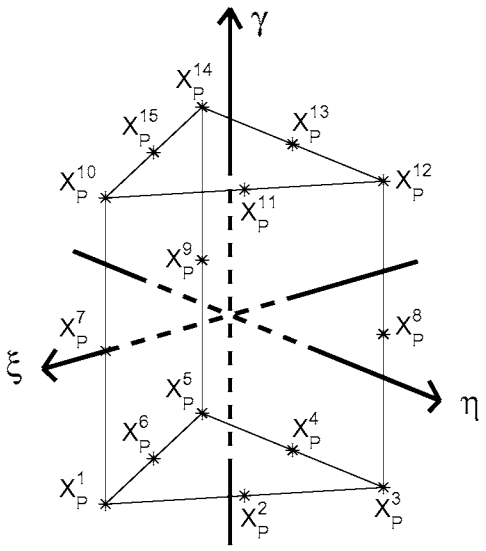

Figure A.1: Three-dimensional infinite element where nodes X_P^{10}, X_P^{11}, X_P^{12}, X_P^{13}, $X_P^{10} \to \infty$ when γ_{10}, γ_{11}, γ_{12}, γ_{13}, γ_{14}, $\gamma_{15} \to \infty$.

The nodes X_P of a three-dimension wedge-shaped element as in Fig. A.1 are

$$X_P = \begin{bmatrix} \xi_1 & \eta_1 & \gamma_1 \\ \xi_2 & \eta_2 & \gamma_2 \\ \xi_3 & \eta_3 & \gamma_3 \\ \xi_4 & \eta_4 & \gamma_4 \\ \xi_5 & \eta_5 & \gamma_5 \\ \xi_6 & \eta_6 & \gamma_6 \\ \xi_7 & \eta_7 & \gamma_7 \\ \xi_8 & \eta_8 & \gamma_8 \\ \xi_9 & \eta_9 & \gamma_9 \\ \xi_{10} & \eta_{10} & \gamma_{10} \\ \xi_{11} & \eta_{11} & \gamma_{11} \\ \xi_{12} & \eta_{12} & \gamma_{12} \\ \xi_{13} & \eta_{13} & \gamma_{13} \\ \xi_{14} & \eta_{14} & \gamma_{14} \\ \xi_{15} & \eta_{15} & \gamma_{15} \end{bmatrix} = \begin{bmatrix} 1 & 0 & -1 \\ \frac{1}{4} & \frac{\sqrt{3}}{4} & -1 \\ -\frac{1}{2} & \frac{\sqrt{3}}{2} & -1 \\ -\frac{1}{2} & 0 & -1 \\ -\frac{1}{2} & -\frac{\sqrt{3}}{2} & -1 \\ \frac{1}{4} & -\frac{\sqrt{3}}{4} & -1 \\ 1 & 0 & 0 \\ -\frac{1}{2} & \frac{\sqrt{3}}{2} & 0 \\ -\frac{1}{2} & -\frac{\sqrt{3}}{2} & 0 \\ 1 & 0 & 1 \\ \frac{1}{4} & \frac{\sqrt{3}}{4} & 1 \\ -\frac{1}{2} & \frac{\sqrt{3}}{2} & 1 \\ -\frac{1}{2} & 0 & 1 \\ -\frac{1}{2} & -\frac{\sqrt{3}}{2} & 1 \\ \frac{1}{4} & -\frac{\sqrt{3}}{4} & 1 \end{bmatrix} . \tag{A.1}$$

The basis functions are

$$\varphi_1(\xi,\eta,\gamma) = \frac{1}{2}L_1(2L_1-1)(1-\gamma) - \frac{1}{2}L_1(1-\gamma^2) \quad \text{(A.2)}$$
$$\varphi_2(\xi,\eta,\gamma) = 2L_1L_3(1-\gamma) \quad \text{(A.3)}$$
$$\varphi_3(\xi,\eta,\gamma) = \frac{1}{2}L_3(2L_3-1)(1-\gamma) - \frac{1}{2}L_3(1-\gamma^2) \quad \text{(A.4)}$$
$$\varphi_4(\xi,\eta,\gamma) = 2L_2L_3(1-\gamma) \quad \text{(A.5)}$$
$$\varphi_5(\xi,\eta,\gamma) = \frac{1}{2}L_2(2L_2-1)(1-\gamma) - \frac{1}{2}L_2(1-\gamma^2) \quad \text{(A.6)}$$
$$\varphi_6(\xi,\eta,\gamma) = 2L_1L_2(1-\gamma) \quad \text{(A.7)}$$
$$\varphi_7(\xi,\eta,\gamma) = L_1(1-\gamma^2) \quad \text{(A.8)}$$
$$\varphi_8(\xi,\eta,\gamma) = L_3(1-\gamma^2) \quad \text{(A.9)}$$
$$\varphi_9(\xi,\eta,\gamma) = L_2(1-\gamma^2) \quad \text{(A.10)}$$
$$\varphi_{10}(\xi,\eta,\gamma) = \frac{1}{2}L_1(2L_1-1)(1+\gamma) - \frac{1}{2}L_1(1-\gamma^2) \quad \text{(A.11)}$$
$$\varphi_{11}(\xi,\eta,\gamma) = 2L_1L_3(1+\gamma) \quad \text{(A.12)}$$
$$\varphi_{12}(\xi,\eta,\gamma) = \frac{1}{2}L_3(2L_3-1)(1+\gamma) - \frac{1}{2}L_3(1-\gamma^2) \quad \text{(A.13)}$$
$$\varphi_{13}(\xi,\eta,\gamma) = 2L_2L_3(1+\gamma) \quad \text{(A.14)}$$
$$\varphi_{14}(\xi,\eta,\gamma) = \frac{1}{2}L_2(2L_2-1)(1+\gamma) - \frac{1}{2}L_2(1-\gamma^2) \quad \text{(A.15)}$$
$$\varphi_{15}(\xi,\eta,\gamma) = 2L_1L_2(1+\gamma) \quad \text{(A.16)}$$

where

$$L_1 = \frac{1}{3}(1+2\xi) \quad \text{(A.17)}$$
$$L_2 = \frac{1}{3}(1-\xi-\sqrt{3}\eta) \quad \text{(A.18)}$$
$$L_3 = \frac{1}{3}(1-\xi+\sqrt{3}\eta)\ . \quad \text{(A.19)}$$